

THE POLARIZATION AND MAGNETIC MOMENT  
OF THE SIGMA PLUS HYPERON

by

CAROL ANN WILKINSON

A thesis submitted in partial fulfillment of the  
requirements for the degree of

Doctor of Philosophy  
(Physics)

at the

UNIVERSITY OF WISCONSIN - MADISON

1985



## THE POLARIZATION AND MAGNETIC MOMENT

## OF THE SIGMA PLUS HYPERON

Carol Ann Wilkinson

Under the supervision of Professor Lee G. Pondrom

## ABSTRACT

The polarization and magnetic moment of the  $\Sigma^+$  hyperon have been determined by analyzing 137,300  $\Sigma^+ \rightarrow p\pi^0$ ,  $\pi^0 \rightarrow 2\gamma$  decays. A beam of inclusively-produced, polarized  $\Sigma^+$  hyperons was generated in a Fermilab Meson Lab beamline by 400 GeV protons incident on a beryllium target. The  $\Sigma^+$ 's were produced at an angle of 5 mrad and ranged in momentum from 140 GeV/c to 350 GeV/c. The  $\Sigma^+ \rightarrow p\pi^0$ ,  $\pi \rightarrow 2\gamma$  decays were detected by a multiwire proportional and drift chamber spectrometer with a lead glass array.

The measured average polarization was

$$P_{\text{ave}} = +0.234 \pm 0.005 .$$

The range in transverse momentum was  $0.7 < P_T < 1.75$  GeV/c and in Feynman  $x$  was  $0.35 < x_F < 0.88$ . The polarization was precessed through a measured angle of  $201.54^\circ \pm 1.34^\circ$  while passing through a magnetized channel with a field integral of  $6.55 \pm 0.01$  T-m. The precession angle measurement was used to determine the magnetic moment,

$$\mu_{\Sigma^+} = 2.469 \pm 0.019 \mu_n ,$$

where the quoted error combines a statistical error of  $\pm 0.011$  and an estimated systematic error of  $\pm 0.016$ .

## ACKNOWLEDGEMENTS

"Fellowship is heaven; lack of fellowship is hell"

William Morris

I would like to thank Lee Pondrom for the many interesting talks we had at the beginning of our collaboration and for his continuing support as my thesis advisor.

I also acknowledge with pleasure the many contributions of the various members of the Michigan-Minnesota-Rutgers-Wisconsin Hyperon Group. Kam-biu Luk, Byron Lundberg, and Craig Dukes manned the portakamp with zeal and an appreciated attention to detail. Ken Heller, Oliver Overseth, and Marleigh Sheaff contributed their expertise in data taking and analysis. The special wizardry of Bob Handler is evident in every aspect of the experiment, from chamber building to his elegant reconstruction programs. George Ott and Jesse Jaske built and maintained apparatus, retaining their good humor against all pressures. Andy Beretvas provided continuous support and many useful suggestions for handling difficult subjects such as data analysis and group politics. The whimsey Ron Grobel brought to life and high energy physics enlivened many otherwise dull moments and is remembered with fondness.

Special thanks go to Tom Devlin, one of the major moving forces in our collaboration. Tom's pushing my apparatus out of the beamline before I could accumulate too much data and his unflagging interest and help on the analysis have helped propel me, at last, out of graduate school.

Many thanks are also due to Tom Mattison, who chivvied me into learning the modern plotting methods essential to the understanding of this experiment and who shared his expertise in this vital area.

The cooperation and efforts of the Fermilab staff, especially that of the Meson Lab, towards making this experiment a success are acknowledged with appreciation.

Finally, I would like to thank my close friends and relatives, who have supported me in graduate school.

## TABLE OF CONTENTS

	Page
ABSTRACT .....	iii
ACKNOWLEDGEMENTS .....	iv
TABLE OF CONTENTS .....	vi
LIST OF TABLES .....	viii
LIST OF FIGURES .....	ix
1. INTRODUCTION	
1.1 JUSTIFICATION .....	1
1.2 EXPERIMENTAL BACKGROUND .....	2
1.3 SPIN AND POLARIZATION .....	4
1.4 SPIN PRECESSION IN A MAGNETIC FIELD .....	6
1.5 MAGNETIC MOMENTS .....	9
2. APPARATUS .....	16
2.1 INTRODUCTION .....	16
2.2 PROTON BEAM TRANSPORT .....	17
2.3 HYPERON BEAM CHANNEL .....	19
2.4 PRECESSION FIELD .....	22
2.5 CHARGED PARTICLE SPECTROMETER .....	24
2.5.1 INTRODUCTION .....	24
2.5.2 MULTIWIRE PROPORTIONAL CHAMBERS .....	25
2.5.3 CHAMBER COORDINATE SYSTEM .....	27
2.5.4 DRIFT CHAMBERS .....	28
2.5.5 DRIFT CHAMBER CALIBRATION .....	30
2.5.6 ANALYZING MAGNETS .....	32
2.5.7 SCINTILLATION COUNTERS .....	32
2.5.8 REDUCTION OF MULTIPLE SCATTERING .....	33
2.6 GAMMA DETECTORS .....	34
2.6.1 LEAD GLASS ARRAY .....	34
2.6.2 LEAD GLASS CALIBRATION .....	36
2.6.3 MWPC GAMMA DETECTOR - C9 .....	38
2.6.4 MWPC GAMMA DETECTOR - C5 .....	39
2.7 TRIGGER LOGIC .....	41
2.8 DATA ACQUISITION .....	42

2.8.1	ELECTRONICS .....	42
2.8.2	DATA TAPE CONTENTS .....	43
3.	EVENT RECONSTRUCTION AND SELECTION .....	44
3.1	INTRODUCTION .....	44
3.2	CHARGED TRACK RECONSTRUCTION .....	45
3.3	GAMMA RECONSTRUCTION .....	52
3.4	KINEMATIC FITS .....	55
3.5	MONTE CARLO PROGRAM .....	58
3.6	CUTS AND BACKGROUND STUDIES .....	63
3.7	FINAL EVENT SAMPLE .....	68
4.	POLARIZATION AND MAGNETIC MOMENT ANALYSIS .....	76
4.1	INTRODUCTION .....	76
4.2	POLARIZATION ANALYSIS .....	76
4.3	ACCEPTANCE STUDIES .....	81
4.3.1	DEPENDENCE ON PHYSICAL PARAMETERS .....	81
4.3.2	EFFECT OF TARGETING ANGLES .....	83
4.3.3	EFFECT OF GAMMA DETECTION .....	85
4.4	POLARIZATION RESULTS .....	88
4.5	PRECESSION ANGLE MEASUREMENT .....	90
4.6	MAGNETIC MOMENT CALCULATION .....	91
4.7	SYSTEMATIC ERRORS .....	94
5.	RESULTS AND IMPLICATIONS .....	100
5.1	RESULTS SUMMARY .....	100
5.2	POLARIZATION THEORIES .....	101
5.3	MAGNETIC MOMENT MODELS .....	109
	REFERENCES .....	115

## LIST OF TABLES

	Page
1.1 Ground state spin wave functions for the 1/2 <sup>+</sup> baryon octet. ....	13
1.2 Quark masses and magnetic moments generated by the naive quark model. ....	14
1.3 Naive quark model predictions and measurements of the baryon magnetic moments. ....	14
2.1 Multiwire proportional chamber statistics. ....	27
2.2 Drift chamber calibration results. ....	28
3.1 Charged track pattern recognition codes. ....	50
3.2 Gamma reconstruction codes. ....	54
3.3 Pattern recognition event types for events with reconstructable charged tracks. ....	54
3.4 The number of events in each reconstruction category for the final sample ....	69
4.1 Results for the polarization, precession angle, and magnetic moment for nine momentum bins. ....	92
4.2 Polarization analysis for samples with known zero polarization. ....	95
5.1 $\Sigma^+$ magnetic moment measurements to date. ....	104
5.2 Theoretical predictions for the hyperon magnetic moments .....	111



## LIST OF FIGURES

	Page
1.1 Spin and momentum precession for a charged particle moving in a magnetic field. ....	5
1.2 Baryon magnetic moment measurements compared to quark model predictions. ....	15
1.3 Differences between the measured magnetic moments and the predictions. ....	15
2.1 The M2 proton beam transport system. ....	18
2.2 The hyperon production target and proton beam monitors. ....	18
2.3 Plan and elevation views of the charged hyperon collimator. ....	20
2.4 The relative momentum acceptance of the charged hyperon collimator for non-decaying particles. ....	21
2.5 The total precession field integral vs. the standard field. ....	23
2.6 Plan view of the charged hyperon $\Sigma^+ \rightarrow p\pi^0$ detector. ....	25
2.7 Lead glass array and associated gamma detectors. ....	35
2.8 Lead, scintillator, MWPC sandwich used to detect gammas upstream of the momentum analyzing magnet. ....	40
3.1 Equivalent source point in the bend plane of the precession magnet. ....	47
3.2 Event reconstruction and event selection flow chart. ....	51
3.3 Diagram of an event fitting the decay hypothesis $\Sigma^+ \rightarrow p\pi^0$ , $\pi^0 \rightarrow 2\gamma$ . ....	57
3.4 Acceptance of $\Sigma^+ \rightarrow p\pi^0$ decays in the collimator channel, in the trigger, and in the reconstruction programs. ....	60
3.5 $\Sigma^+$ momentum spectrum for the Monte Carlo and data $\Sigma^+$ candidate samples. ....	64

3.6	Comparison of geometric $\chi^2$ fit to the charged track information for data and Monte Carlo samples. ....	64
3.7	Kinematic $\chi^2$ distributions for data and Monte Carlo $\Sigma^+$ candidate samples. ....	66
3.8	The $\Sigma^+$ decay vertex distribution after all cuts. ....	70
3.9	Laboratory opening angle between $\Sigma^+$ and the daughter proton for the final sample of events. ....	70
3.10	The momentum spectra for $\Sigma^+$ , p, $\pi^0$ after all cuts. ....	71
3.11	Chi-square distributions of the various reconstruction fits for the final data sample. ....	72
3.12	The $\gamma\gamma$ invariant mass plot for events in the final sample with two gammas in the lead glass array. ....	74
3.13	The $p\pi^0$ invariant mass plot obtained from the measured values. ....	75
4.1	Initial direction of the polarization vector at production. ....	78
4.2	$R_i(\cos\theta)$ plotted versus $\cos\theta$ for the total sample summed over momentum. ....	80
4.3	Acceptance plots for $\cos\theta_i$ , $i = x, y, z$ , for 3 representative momentum bins. ....	82
4.4	Measured production angle $\theta_y$ showing the difference in $\pm 5$ mrad targeting. ....	84
4.5	Acceptance plots for $\cos\theta_i$ , $i = x, y, z$ , for the total samples, and for the 1-gamma and 2-detected-gammas subsamples ....	87
4.6	Precession of the polarization vector in magnet M2. ....	89
4.7	Polarization plotted as a function of momentum for the total data sample. ....	93
4.8	Plot of $P_z$ versus $P_x$ for nine momentum bins. ....	93
4.9	The magnetic moment plotted as a function of momentum. ....	93
4.10	The $\Sigma^+$ magnetic moment plotted against the various cut parameters. ....	97
4.11	The $\Sigma^+$ magnetic moment for various detection type classifications. ....	98

4.12	The polarization and magnetic moments for the kink track data for two different analysis methods. ....	99
5.1	Plot of precession angle versus magnetic field integral. ....	102
5.2	$\Sigma^+$ magnetic moment measurements as a function of time. ....	103
5.3	Collected inclusive polarization data for hyperons. ....	105
5.4	An $s\bar{s}$ pair is created along a color force field string. ....	108

*Scarecrow, let me tell you something. Back where I come from, we have things called universities. People study there for years, and when they're finished they have no more brains than you. The one thing they have that you lack is a diploma!*

The Wizard of Oz,  
adapted by Horace J. Elias  
from the original story by  
L. Frank Baum

## CHAPTER 1: INTRODUCTION

## 1.1 JUSTIFICATION

This work describes a measurement of the polarization and magnetic moment of a large sample of inclusively produced  $\Sigma^+$  hyperons. Both polarization and magnetic moments have been useful in testing theories which describe the structure and interactions of elementary particles. The magnetic moment of a particle with charge  $q$ , mass  $m$ , and spin angular momentum  $\vec{S}$  is given by

$$\vec{\mu} = \frac{g}{2} \left( \frac{q}{mc} \right) \vec{S} , \quad (1.1)$$

where the gyromagnetic ratio,  $g$ , is defined by this equation. The magnetic moment is a static property which can be measured without disturbing internal structure, making it a good probe of the complex hadronic structure. The large anomalous moments ( $g \neq 2$ ) of the baryons provide a testing ground for current theories describing the hadrons, since their magnetic moment predictions are sensitive to the assumed internal arrangements. The simple  $SU(6)$  quark model, for example, assumes that the particle moments are sums of the constituent quark moments and is able to predict the known baryon magnetic moments to within  $\sim 0.20$  n.m. Accurate magnetic moment measurements are needed to help select refinements to this and other models which will improve the match between theory and data.

Inclusively produced polarization, a net alignment of spins in a statistical sample of particles, occurs during interactions and provides a test not only of theories of hadron structure but also of theories detailing interactions between structural elements. Again, taking the naive quark model as an example, the predicted polarizations depend upon the assumed interaction processes. In this model, a proton composed of three quarks (uud) exchanges a d-quark for a sea s-quark in an interaction with another nucleon, becoming a  $\Sigma^+$  (uus). The two u-quarks are spectators in the interaction. If the s-quark carries the polarization in some unspecified manner, the relative magnitudes and signs of the hyperon polarizations can be predicted. An extension of this idea which includes polarization of the spectator quarks allows a similar set of predictions to be made. Hyperon polarization measurements may help distinguish between these and other predictions and shed light on the confused picture of hadronic interactions.

## 1.2 EXPERIMENTAL BACKGROUND

By 1975, the proton and neutron magnetic moments had been measured and shown to agree with the then current quark model theories.<sup>1</sup> Several hyperon moments had also been measured with enough accuracy to show serious discrepancies between theory and measurement.<sup>2</sup> In 1976, an experimental group at Fermilab discovered polarization in  $\Lambda$ 's inclusively produced in the interaction  $p + \text{Be} \rightarrow \Lambda + \text{anything}$ .<sup>3</sup> An inclusive sample contains particles that are produced directly in the interaction or that are decay products of other directly produced

particles. Polarization was surprising since a net spin alignment in a sample produced by diverse mechanisms was expected to be zero. This discovery allowed the same experimental group to use a beam of polarized  $\Lambda$ 's to obtain a precision measurement of the  $\Lambda$  magnetic moment.<sup>4</sup>

Although none of the accepted theories<sup>5</sup> of two body interactions could adequately explain inclusive polarization, it was soon demonstrated that the alignment was not a nuclear effect. Experiments measuring polarization as a function of target material, incident proton energy, or kinematic variables such as  $p_{\perp}$  or Feynman  $x$  have established polarization as a general feature of inclusively produced  $\Lambda$ 's.<sup>6-10</sup> Subsequent experiments have shown that the  $\Xi^0$  is also produced polarized,<sup>11</sup> but that  $\bar{\Lambda}$ 's<sup>12</sup> and protons<sup>13,14</sup> are not. Some phenomenological models attempting to describe this polarization have advanced the theory that all hyperons are polarized in inclusive production.<sup>12,15,16</sup> If so, their magnetic moments can be measured via the same techniques as those used to measure the  $\Lambda$  moment.<sup>17</sup>

It was in the hopes of discovering polarization in the charged hyperons  $\Sigma^+$ ,  $\Sigma^-$ ,  $\Xi^-$ , and  $\Omega^-$  that experiment E620 was performed at Fermilab. Measurable polarization would allow the determination of additional magnetic moments needed to test theory. Polarization had been seen in exclusive processes such as  $K^- p \rightarrow \Sigma^+ \pi^-$ ,<sup>18</sup> but it was not known if inclusively produced  $\Sigma^+$  would also exhibit polarization. This thesis presents the experimental results for  $\Sigma^+$ .

Experiment E620 determined that the inclusively produced  $\Sigma^+$  were indeed polarized, with a sign opposite to that of the  $\Lambda$  and a magnitude which averaged  $0.234 \pm 0.005$  over the momentum range 140-350 GeV/c. The magnetic moment was found to be

$$\mu_{\Sigma^+} = 2.469 \pm 0.011 \pm 0.016 \mu_n ,$$

where the first error is statistical and the second is the estimated systematic error. This measurement is in good agreement with the world average  $\mu_{\Sigma^+} = 2.30 \pm 0.13$  current at the time of data taking,<sup>18</sup> and shows a considerable improvement in precision.

### 1.3 SPIN AND POLARIZATION

The spin of a particle is defined to be its intrinsic angular momentum and is a purely quantum mechanical property. According to Ehrenfest's theorem, however, the expectation value of a quantum mechanical observable follows classical equations of motion. In the classical format,<sup>19</sup> a measurement of a particle's component of spin along any specified direction  $\hat{e}$  will obtain one of the  $2S + 1$  eigenvalues for spin  $\vec{S}$ . The ratio of the expectation value of the spin component along  $\hat{e}$  to the maximum possible value is called the polarization  $P$ , ( $-1 \leq P \leq 1$ ). It should be noted that classical statements about the spin direction refer to the instantaneous particle rest frame and are therefore applicable to massive particles only.



The polarized  $\Sigma^+$  hyperons in this experiment were produced by bombarding a beryllium target with 400 GeV/c protons. Any parity allowed polarization must be perpendicular to the production plane defined by  $\hat{k}_p \times \hat{k}_\Sigma$ , where  $\hat{k}_p$  and  $\hat{k}_\Sigma$  are the directions of the incoming proton and the outgoing  $\Sigma^+$  momenta. The  $\Sigma^+$  beam traverses a region of homogeneous magnetic field which is parallel to the production plane and perpendicular to the spin direction. The spin precesses about the magnetic field direction, as shown in Figure 1.1. The final spin direction was determined by measuring the asymmetry of the  $\Sigma^+ \rightarrow p\pi^0$  decay. Due to parity violation in weak decays, the angular distribution of the daughter protons is a function of the  $\Sigma^+$  polarization.

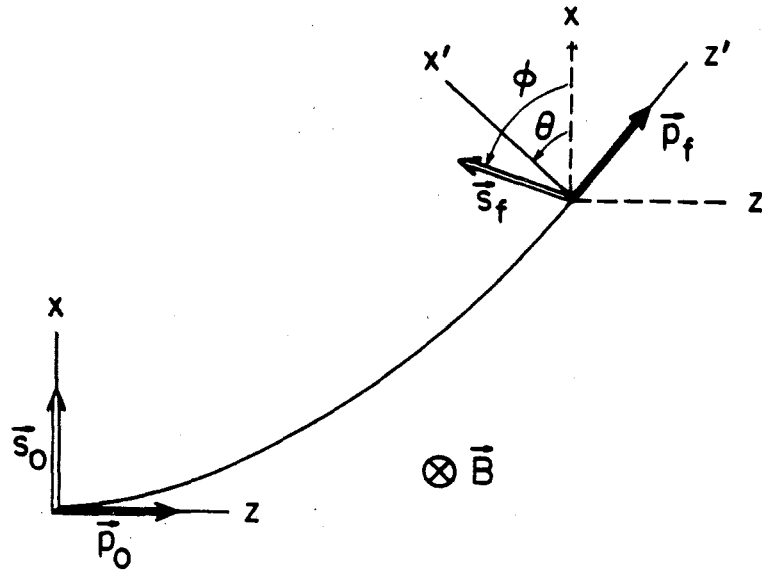


Figure 1.1 Spin and momentum precession for a charged particle moving in a magnetic field perpendicular to the plane defined by the initial vectors.

#### 1.4 SPIN PRECESSION IN A MAGNETIC FIELD

The time rate of change of the spin  $\hat{S}$ , in the center of mass frame of a particle with magnetic moment  $\vec{\mu}$ , is classically<sup>20</sup> given by

$$\frac{d\vec{S}}{dt} = \vec{\mu} \times \vec{B} \quad (1.2)$$

or

$$\frac{d\vec{S}}{dt} = \frac{g}{2} \left( \frac{q}{mc} \right) \vec{S} \times \vec{B} . \quad (1.3)$$

Since the magnetic field  $\vec{B}$  is perpendicular to the spin  $\vec{S}$  in the experiment, the magnitude of the spin remains unchanged. The spin direction merely precesses in the plane perpendicular to the magnetic field, at the rate

$$\frac{d\phi}{dt} = \frac{g}{2} \left( \frac{q}{mc} \right) (-B) . \quad (1.4)$$

Equations (1.3) and (1.4) describe the spin motion in the rest frame (CM) of the  $\Sigma^+$  and must be transformed to the laboratory frame (LAB), where  $\vec{B}$  and the change in angle  $\phi$  are measured. When the  $\Sigma^+$  passes through the magnet, however, both its spin and momentum vectors precess. This means that the rest frame in which spin is defined is rotating with respect to the LAB frame and a simple Lorentz boost is not sufficient for the transformation. The LAB rate of change of a vector quantity  $\vec{G}$  is given by the Thomas equation<sup>21</sup>

$$\left(\frac{d\vec{G}}{dt}\right)_{\text{LAB}} = \left(\frac{d\vec{G}}{dt}\right)_{\text{CM}} + \vec{\omega}_T \times \vec{G}, \quad (1.5)$$

which states that the rate of change in a fixed reference frame (LAB) is equal to the rate of change in the CM frame plus a purely kinematical term due to the rotation of the CM frame in the fixed frame. The Thomas frequency is defined as

$$\vec{\omega}_T = \frac{\gamma^2}{\gamma + 1} \frac{\vec{a} \times \vec{v}}{c^2}, \quad (1.6)$$

where  $\gamma^2 = (1 - \beta^2)^{-1}$  and  $\beta = v/c$ . The acceleration experienced by a moving charged particle in a magnetic field is

$$\vec{a} = \frac{q}{\gamma mc} \vec{v} \times \vec{B}, \quad (1.7)$$

so, for  $\vec{v} \perp \vec{B}$ ,

$$\vec{\omega}_T = \left[1 - \frac{1}{\gamma}\right] \frac{q}{mc} \vec{B}. \quad (1.8)$$

Thus Equation (1.2), when transformed to the LAB, becomes

$$\frac{d\vec{S}}{dt}(\text{LAB}) = \frac{q}{mc} \left[ \frac{g}{2} - 1 + \frac{1}{\gamma} \right] \vec{S} \times \vec{B}. \quad (1.9)$$

With  $\vec{S} \perp \vec{B}$ , Equation (1.9) reduces to an equation for the precession frequency

$$\frac{d\vec{\phi}}{dt}(\text{LAB}) = \frac{q}{mc} \left[ \frac{g}{2} - 1 + \frac{1}{\gamma} \right] (-\vec{B}) . \quad (1.10)$$

Integrating over the magnetic field length  $d\lambda = \beta c dt$  gives the change in angle with respect to a fixed axis

$$\phi(\text{LAB}) = - \frac{q}{\beta mc} \left[ \frac{g}{2} - 1 + \frac{1}{\gamma} \right] \int B d\lambda . \quad (1.11)$$

See Figure 1.1. The angle the spin direction makes with the rotated axis, after passing through the magnet, is then

$$(\phi - \theta)_{\text{LAB}} = - \frac{q}{\beta mc} \left[ \frac{g}{2} - 1 \right] \int B d\lambda , \quad (1.12)$$

where  $\theta = (q/\beta \gamma mc^2) \int B d\lambda$  represents the rotation of the axis. The same result can be obtained by a more elegant method than the classical Thomas derivation outlined above. If the spin vector  $\vec{S}$  is generalized to an axial 4-vector in the CM frame, the equation of motion can be treated relativistically with Lorentz covariance to obtain the BMT equation,<sup>22</sup> which reduces to the Thomas Equation (1.9) for this case.

It is necessary to relate the quantities in Equation (1.12) to the measured quantities in the laboratory. The vertical magnetic field is defined to lie in the  $-y$  direction, and the  $\vec{\Sigma}^+$  velocity vector at production defines the  $+z$  direction. The initial spin direction  $\vec{S}$  must lie in either the  $+x$  or  $-x$  direction;  $\hat{x} = \hat{y} \times \hat{z}$ . In this LAB frame the leading minus sign in Equation (1.12) disappears since it simply indicates that positive rotations lie along  $-\vec{B}$ , which is now  $+\hat{y}$ . Using

$q_{\Sigma^+} = e$  and  $(e\hbar/2m_p c) = 3.15252 \times 10^{-14}$  MeV/T, the measured angle between the final spin vector and the x-axis of the rotated reference frame is, at last,

$$(\phi - \theta)_{\text{LAB}} = \frac{1}{\beta} (18.307^\circ/\text{T-m}) \left[ \frac{g}{2} - 1 \right] \frac{m_p}{m_{\Sigma}} \int B d\lambda. \quad (1.13)$$

This equation is essentially momentum independent since  $\beta = 1$  to better than 0.01% over the momentum range of the experiment.

### 1.5 MAGNETIC MOMENTS

Magnetic moments for the spin  $1/2^+$  baryons are usually given in terms of nuclear magnetons  $\mu_n = (e\hbar/2m_p c)$ , where  $m_p$  is the mass of the proton. Rewriting Equation (1.1) in units of  $\mu_n$  gives

$$\vec{\mu} = \frac{g}{2} \left[ \frac{m_p}{m} \right] q \hat{S}, \quad (1.14)$$

where  $q$  is in units of  $e$ . Equation (1.12) demonstrates that a measurement of the spin precession angle results in a determination of  $g/2$  and the anomalous magnetic moment defined above. The interest in making this measurement lies in the comparison between experiment and the theoretical models which attempt to construct the total baryon moments from individual contributions by particle components.

Successful constituent models describe the baryons as systems made up of three spin  $1/2$  flavored quarks with fractional charge. Considering its simplicity, the naive quark model predictions for the baryon moments are remarkably close to the measured values. In the

simplest non-relativistic SU(6) case, the baryons are formed by a combination of three quarks assumed to be in a ground state with zero orbital angular momentum. An additional restriction that the color portion of the wave function be a singlet state is apparently required of observable particles. The space-spin-flavor portion must therefore be symmetric for the overall fermion wave function to be antisymmetric. This implies that any two quarks of the same flavor must be in a triplet spin state. Table 1.1 lists the ground state spin wave functions for the light  $1/2^+$  baryons.

The magnetic moment of a baryon composed of three quarks in such an S-wave state is given by the sum over the flavors  $i$ ,

$$\mu_B = \sum_i \langle B | \mu_i | B \rangle \quad (1.15)$$

where  $\mu_i$  is the magnetic moment operator of a quark with flavor  $i$  and  $|B\rangle$  is the baryon wave function. Using the wave functions in Table 1.1, the calculated baryon magnetic moments are represented by the following linear combinations of the individual quark moments:

$$\mu_p = \frac{4}{3} \mu_u - \frac{1}{3} \mu_d$$

$$\mu_n = \frac{4}{3} \mu_d - \frac{1}{3} \mu_u$$

$$\mu_\Lambda = \mu_s$$

$$\mu_{\Sigma^+} = \frac{4}{3} \mu_u - \frac{1}{3} \mu_s$$

$$\mu_{\Sigma^0 \rightarrow \Lambda} = \frac{1}{\sqrt{3}} (\mu_d - \mu_u) \quad (1.16)$$

$$\mu_{\Sigma^-} = \frac{4}{3} \mu_d - \frac{1}{3} \mu_s$$

$$\mu_{\Sigma^+} = \frac{4}{3} \mu_s - \frac{1}{3} \mu_u$$

$$\mu_{\Xi^-} = \frac{4}{3} \mu_s - \frac{1}{3} \mu_d$$

The above equations involve only three unknown quark moments and can be solved by using three measured baryon moments as input. The first precision measurements were those of the proton, neutron, and  $\Lambda$  moments, which produce the quark moments listed in Table 1.2. These individual moments, when substituted into the remaining equations (1.16), result in the naive quark model magnetic moment predictions listed in Table 1.3 and plotted in Figure 1.2.

The individual quark masses can also be extracted from the three input moments. If the quarks are assumed to be pointlike particles, the intrinsic magnetic moments can be described by

$$\vec{\mu}_i = g \frac{q_i}{2m_i c} \vec{S}_i, \quad (1.17)$$

where  $q_i$  is the quark charge in terms of the unit charge  $e$  and  $m_i$  is the quark mass. With  $g = 2$  and  $S = \hbar/2$ , Equation (1.17) can be solved for the quark mass

$$m_i = \frac{q_i}{\mu_i} m_p . \quad (1.18)$$

The individual quark moment is in nuclear magnetons. The results, given in Table 1.2, agree with broken symmetry SU(6) and bag model predictions.

The measured baryon moments, including those from the E620 charged hyperon experiment, are compared to the quark model predictions in Figure 1.2 and Table 1.3. The manner in which the predictions in Figure 1.2 track the changes in magnitude and sign of the experimental results indicates that the naive quark model is a good description of the gross features of baryon construction. The differences between predicted and measured values, some of which are significant, are plotted in Figure 1.3. Because of the simplicity of this naive model and its assumptions, these differences are not unexpected. The wave functions, for instance, may involve mixing of higher angular momentum states with the S-wave state assumed here. There may also be additional dynamical terms in the magnetic moment besides the term involving the sum of the static quark moments. Corrections due to these and other effects are discussed in Chapter 5. The measured baryon magnetic moments should aid in the creation of refinements to those theories which have proven most successful in describing the complexities of the "elementary" particles.



TABLE 1.1 Ground<sub>23</sub>state spin wave functions for the  $1/2^+$  baryon octet.

---


$$|p\rangle = \frac{1}{\sqrt{18}} [2\uparrow\uparrow\downarrow_{uud} - (\uparrow\downarrow_{uu} + \downarrow\uparrow_{uu}) \uparrow_d + 2 \text{ permutations}]$$

$$|n\rangle = \frac{1}{\sqrt{18}} [2\uparrow\uparrow\downarrow_{ddu} - (\uparrow\downarrow_{dd} + \downarrow\uparrow_{dd}) \uparrow_u + 2 \text{ permutations}]$$

$$|\Lambda\rangle = \frac{1}{\sqrt{12}} [(\uparrow\downarrow_{ud} - \downarrow\uparrow_{ud}) \uparrow_s + 5 \text{ permutations}]$$

$$|\Sigma^+\rangle = \frac{1}{\sqrt{18}} [2\uparrow\uparrow\downarrow_{uus} - (\uparrow\downarrow_{uu} + \downarrow\uparrow_{uu}) \uparrow_s + 2 \text{ permutations}]$$

$$|\Sigma^0\rangle = \frac{1}{\sqrt{36}} [2\uparrow\uparrow\downarrow_{uds} - (\uparrow\downarrow_{ud} + \downarrow\uparrow_{ud}) \uparrow_s + 5 \text{ permutations}]$$

$$|\Sigma^-\rangle = \frac{1}{\sqrt{18}} [(\uparrow\downarrow_{dd} + \downarrow\uparrow_{dd}) \uparrow_s - 2\uparrow\uparrow\downarrow_{dds} + 2 \text{ permutations}]$$

$$|\Xi^0\rangle = \frac{1}{\sqrt{18}} [(\uparrow\downarrow_{ss} + \downarrow\uparrow_{ss}) \uparrow_u - 2\uparrow\uparrow\downarrow_{ssu} + 2 \text{ permutations}]$$

$$|\Xi^-\rangle = \frac{1}{\sqrt{18}} [2\uparrow\uparrow\downarrow_{ssd} - (\uparrow\downarrow_{ss} + \downarrow\uparrow_{ss}) \uparrow_d + 2 \text{ permutations}]$$


---

TABLE 1.2 Quark masses and magnetic moments generated by the naive quark model, with p, n, and  $\Lambda$  magnetic moment measurements as input data..

QUARK	CHARGE (e)	MAGNETIC MOMENT ( $\mu_n$ )	MASS <sub>2</sub> (MeV/c <sup>2</sup> )
u	+2/3	1.85	338
d	-1/3	-0.97	322
s	-1/3	-0.61	509

TABLE 1.3 Naive quark model predictions and measurements of the baryon magnetic moments, in nuclear magnetons. Data are from Ref. 24 except where noted.

BARYON	SU(6)	EXPERIMENT	EXP.-SU(6)
p	input	2.793	--
n	input	-1.913	--
$\Lambda$	input	-0.613 $\pm$ 0.004	--
$\Sigma^+$	2.67	2.469 $\pm$ 0.019 <sup>(a)</sup>	-0.201
$\Sigma^0 \rightarrow \Lambda$	-1.63	1.61 $\pm$ 0.07 <sup>(b)</sup>	+0.02
$\Sigma^-$	-1.09	-1.10 $\pm$ 0.05	-0.01
$\Xi^-$	-0.49	-0.69 $\pm$ 0.04 <sup>(26)</sup>	-0.20
$\Xi^0$	-1.44	-1.253 $\pm$ 0.014	+0.18

(a) this experiment

(b) new world average including data from Ref. 25. Sign of experimental value is assumed negative.

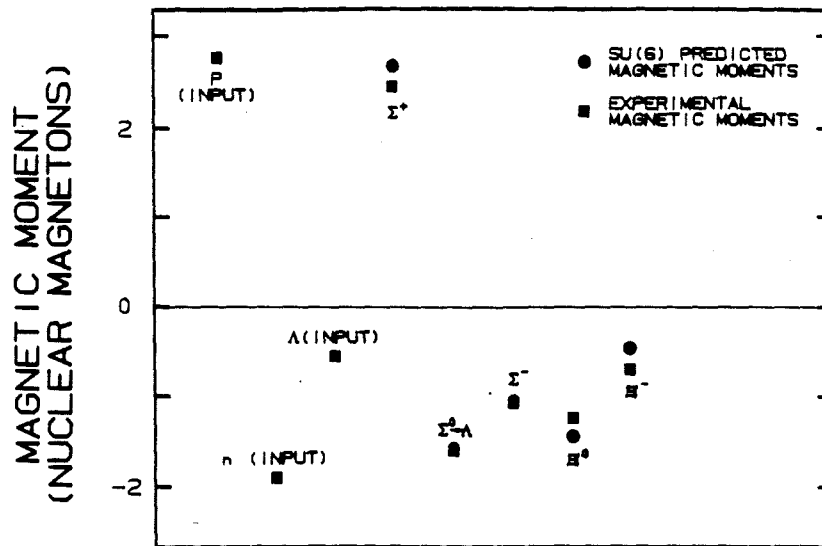


Figure 1.2 Baryon magnetic moment measurements compared to simple quark model predictions, with  $\mu_p$ ,  $\mu_n$ ,  $\mu_\Lambda$  as input data.

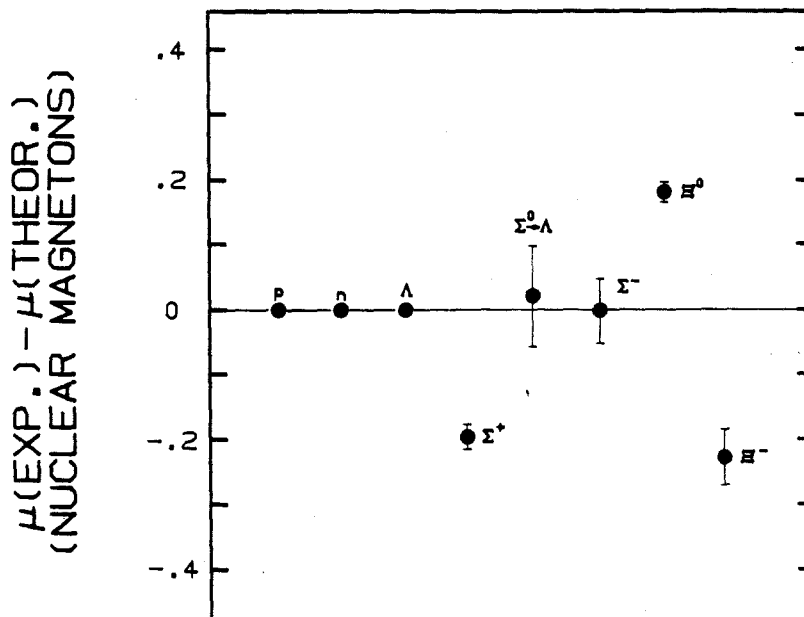


Figure 1.3 Differences between the measured magnetic moments and the predictions. The measurement errors are plotted for comparison.

## CHAPTER 2: APPARATUS

## 2.1 INTRODUCTION

This experiment was one of several hyperon magnetic moment measurements performed in the M2 beam line at Fermi National Accelerator Laboratory. Data for this particular measurement were taken during January, 1980. The decay mode studied was

$$\begin{aligned}\Sigma^+ &\rightarrow p\pi^0 \\ &\quad | \rightarrow \gamma\gamma.\end{aligned}$$

A 400 GeV secondary proton beam produced at the Meson target was transported down the M2 line to the experimental target, where the charged hyperon beam was created. The hyperon beam was collimated and momentum analyzed by a 5.3 m long magnetic channel. A standard spectrometer consisting of multiwire proportional chambers (MWPC), drift chambers, and analyzing magnets was used to detect the tracks of the  $\Sigma^+$  and its charged decay product p. Drift chambers were used in the decay region to make the determination of the vertex more precise. The gammas from the  $\pi^0$  decay were detected by an array of lead glass blocks and by detector "sandwiches" made of scintillator, lead, and MWPC's. A trigger requiring an incoming charged track in the decay volume, a charged track in the downstream spectrometer, and a shower from a neutral particle in the lead glass selected possible  $\Sigma^+ \rightarrow p\pi$  decays. Information from the charged and neutral particle detectors was written to disc file by an online computer and then transferred to

magnetic tape.

## 2.2 PROTON BEAM TRANSPORT

The primary 400 GeV proton beam for this experiment was produced by the Fermilab proton synchrotron. Beam spills of 1 sec duration and average intensity of  $2 \times 10^{13}$  protons per spill were extracted at intervals of 12 seconds and sent to the experimental areas. Roughly 20% of each spill was directed onto the Meson Central target. The M2 beam line was tuned to accept 400 ( $\pm 0.4$ ) GeV protons diffracted at an angle of approximately 0.8 mrad from the primary beam direction and to focus them on the hyperon production target 450 m downstream of Meson Central target.

The transport system for the M2 line consisted of standard focussing quadrupole and steering dipole magnets, as shown in Figure 2.1. The beam was first brought to an intermediate focus 201 m downstream of the Meson target. Intensity was controlled by two sets of movable slits upstream of this focus, and beam size, typically less than 5 mm in diameter, was monitored by a segmented wire ion chamber (SWIC) at the focus. The remaining elements in the transport string brought the beam to a final spatial and momentum focus at the hyperon target. The angle between the incoming proton beam and the outgoing hyperons could be controlled by varying the incident targeting angle. A vernier magnet at 335 m pitched the beam up or down and a dipole string centered at 440 m restored it to the production target median plane. Targeting angles of  $\pm 5$  mrad in the vertical direction were

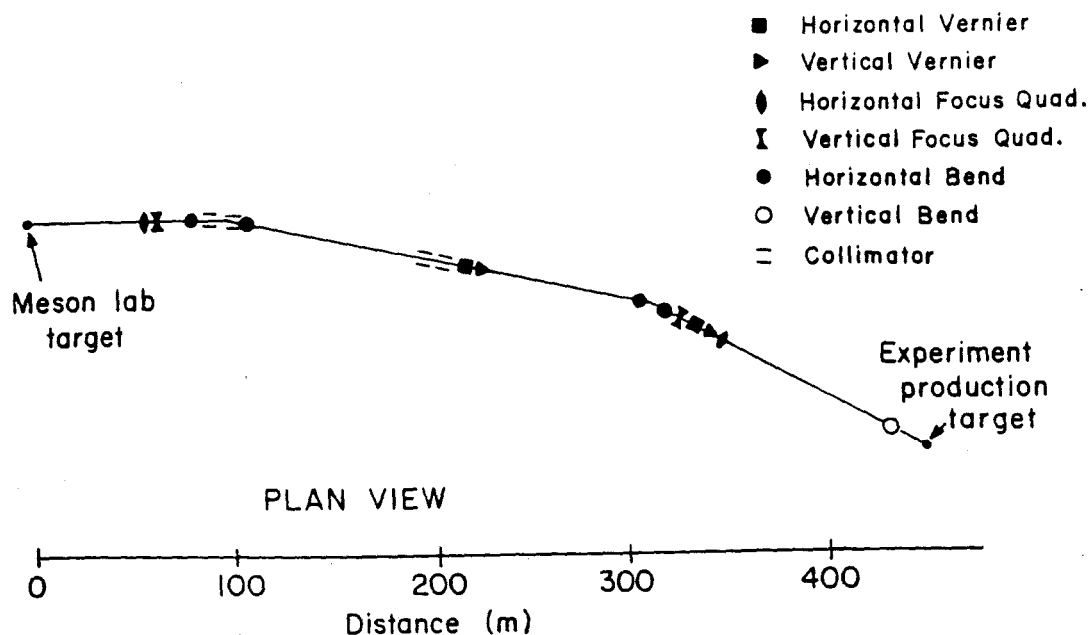


Figure 2.1 The M2 proton beam transport system (not to scale).

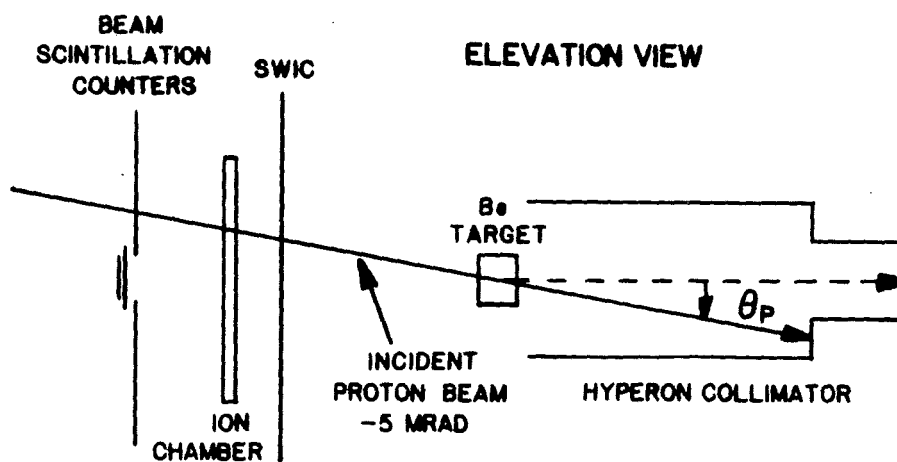


Figure 2.2 The hyperon production target and associated proton beam monitors. The scintillator counters were used to calibrate the ion chamber and were removed during data taking. The ion chamber monitored beam intensity and the SWIC monitored spot size and position. The collimator was designed to absorb the incident proton beam and to transmit particles produced at the hyperon target. (Not to scale)

produced for this experiment.

Figure 2.2 shows the beam monitoring systems placed just upstream of the hyperon target. Average intensities of  $3.0 \times 10^8$  protons/pulse were measured by an argon-filled ion chamber placed one meter upstream of the target. A set of beam and halo scintillator counters were used to calibrate the ion chamber for intensities up to  $10^6$  protons/sec, giving a calibration constant of approximately 100 ion pairs per cm of gas per proton. These calibration counters were not in the beam during data taking. A SWIC with 1 mm spatial resolution monitored beam position and spot size 90 cm upstream of the target. Average beam size was 3 mm FWHM at the SWIC, indicating that about 90% of the proton beam could be contained within a 6 mm cross section.

### 2.3 HYPERON BEAM CHANNEL

The experimental target, a 6 mm diameter by 15 cm long beryllium cylinder, was placed immediately in front of a collimating channel embedded in the gap of a vertical field dipole magnet. The 5.3 m long collimator consisted of nine drilled brass blocks which formed a channel with a circular cross section and an arc of 10 mrad in the horizontal plane. The entrance collimator blocks were designed with decreasing steps in hole sizes to allow the 5 mrad proton beam to be buried in the channel and magnet. The layout is shown in Figure 2.3. The defining aperture for the channel was a 4 mm hole in a tungsten insert in the central collimator block. Another tungsten insert with a 10 mm hole placed in the last collimator block served as the exit

aperture. Tungsten was used in these crucial areas to increase absorption of particles outside the collimated beam. The solid angle acceptance of the channel was  $1.4 \times 10^{-6}$  steradians for the central orbit.

The momentum acceptance of the channel was defined by the dipole magnet, which, at maximum current, had a central field in the vertical direction of 2.6 T, or a total field integral of 13.6 T-m over the particle path. The channel was tuned to transmit 200 GeV/c positively

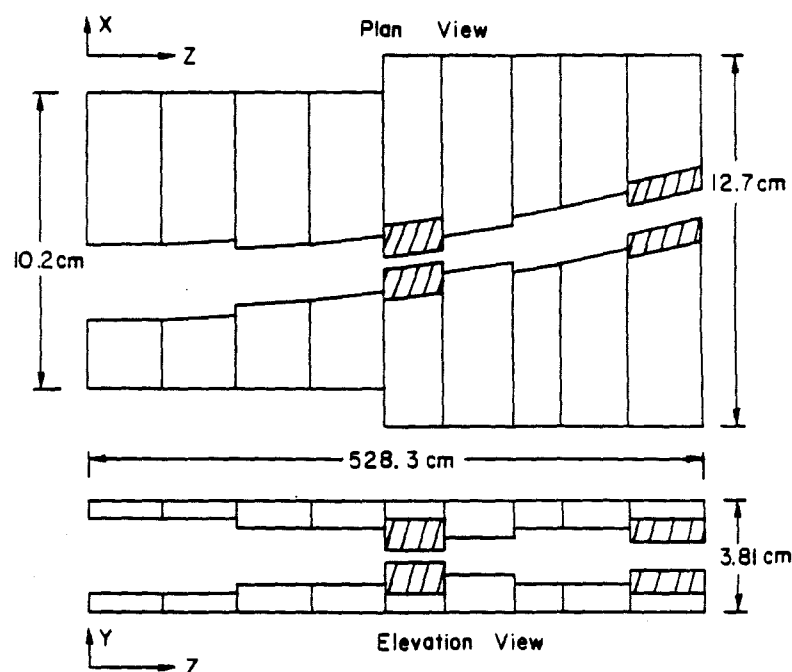


Figure 2.3 Plan and elevation views of the charged hyperon collimator. The collimator was placed in the gap of a dipole magnet with a vertical field. The channel followed an arc of 10 mrad in the horizontal plane and was designed to transmit 200 GeV particles. Shaded areas were tungsten inserts designed to absorb incident beam protons and particles outside the collimated channel.



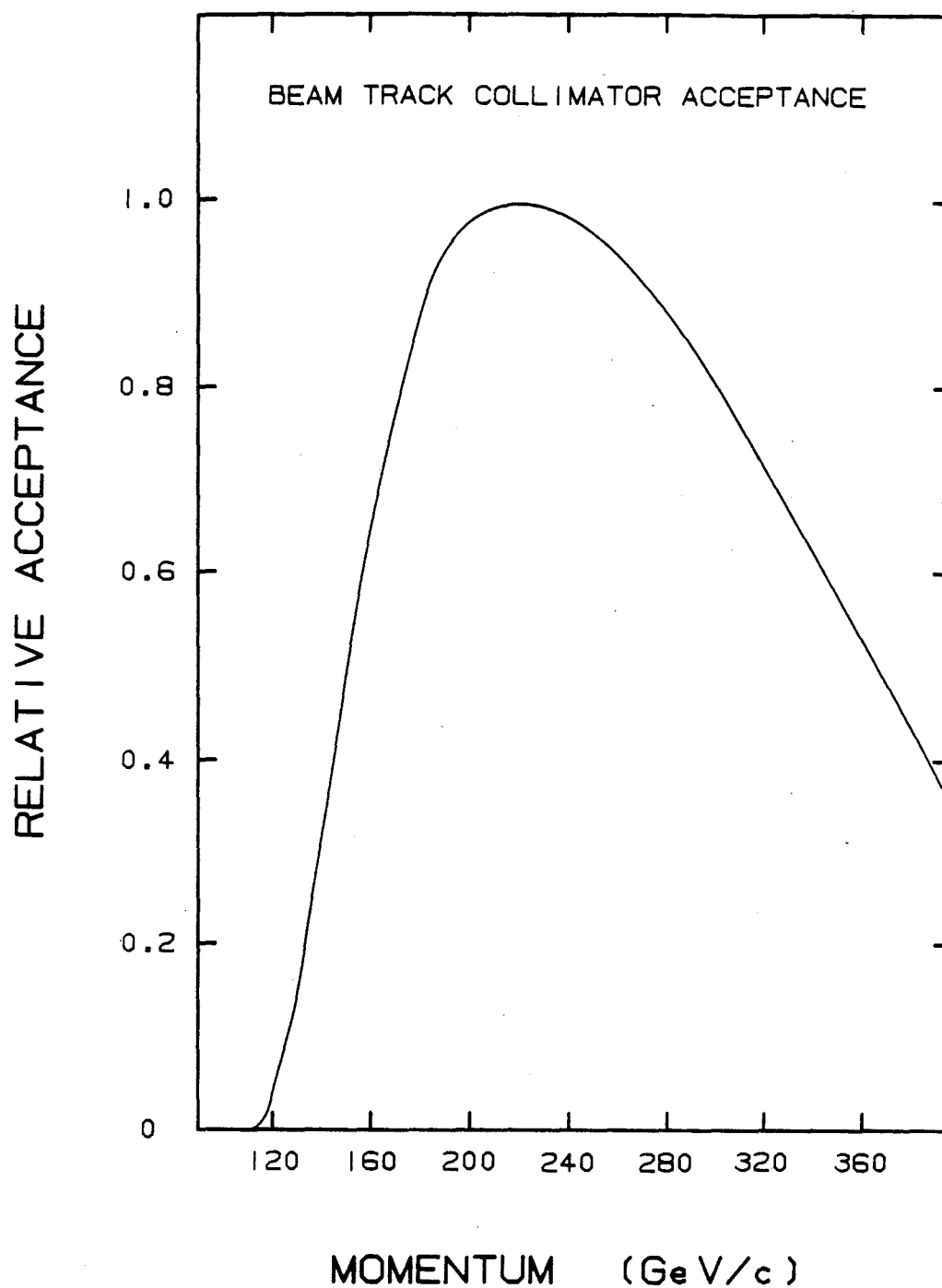


Figure 2.4 The relative momentum acceptance of the charged hyperon collimator for charged, non-decaying particles. The collimator channel was designed to pass 200 GeV particles. An abscissa value of 1 corresponds to the full geometrical solid angle of the collimator central aperture,  $1.4 \times 10^{-6}$  sterad.

charged particles by operating the magnet at a nominal field setting of 6.6 T-m. The momentum acceptance for non-decaying particles produced at the target and exiting from the collimator ranged from 120 GeV/c to over 400 GeV/c, as shown in Figure 2.4. The peak in the spectrum occurred at the nominal tune value of 200 GeV/c. The rates in MWPC C1, placed 70 cm from the collimator exit, indicate that the channel transmitted  $\sim 2 \times 10^5$  total particles per spill. Comparison of the number of reconstructed  $\Sigma^+ \rightarrow p\pi^0$  decays to the number of particles in the beam indicates that this beam consists of  $\sim 0.5\% \Sigma^+$ , after corrections for branching ratios.

#### 2.4 PRECESSION FIELD

The magnet which selected the  $\Sigma^+$  momentum also provided the precession field necessary for determining the  $\Sigma^+$  magnetic moment. A precise measurement of the magnetic moment, however, was possible only if the field integral was well known. A nuclear magnetic resonance (NMR) probe placed in the collimator just before the exit block provided run-to-run monitoring of the field at that point. The relationship between this "standard field" and the total field integral was established during a careful field mapping performed for a previous experiment.<sup>27</sup> The total field integral per standard field plotted in Figure 2.5 was 1.5% less than that quoted in the original source since the target for this experiment was mounted 40 cm closer to the collimator entrance, thereby shortening the  $\Sigma^+$  path length in the entrance fringe field. The NMR probe indicated that the field integral

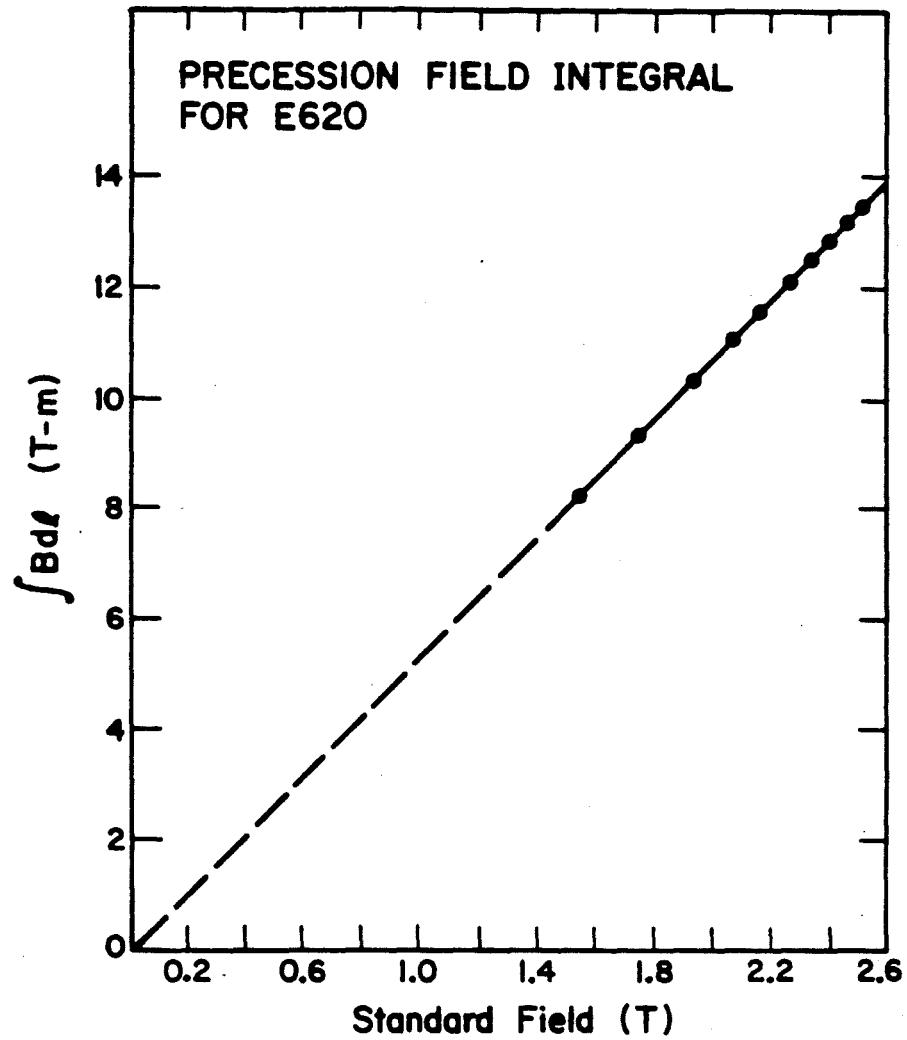


Figure 2.5 The total precession field versus the measured standard field. The field integral for this experiment was  $6.55 \pm 0.01$  T-m, with run-to-run variations of less than 0.1%.

was  $6.55 \pm 0.01$  T-m, with run-to-run variations of less than 0.1%.

## 2.5 CHARGED PARTICLE SPECTROMETER

### 2.5.1 INTRODUCTION

Eight multiwire proportional chambers (MWPC), three drift chambers (DC), two analyzing magnets, and various scintillators comprised the charged particle spectrometer. Two distinct regions of the spectrometer should be noted: an upstream portion which tagged the incoming  $\Sigma^+$  and determined the decay point, and a downstream portion which momentum analyzed the decay protons. The first element of the upstream section, MWPC C1, was positioned 0.7 m from the exit collimator and served to tag the  $\Sigma^+$ . See Figure 2.6. Beam and halo scintillators (S1, S2) defined the accepted positive beam. The remainder of this section consisted of a 12 m decay region stretching from DC1 to C3 and including three drift chambers (DC1-DC3) and two MWPC's (C2, C3). These chambers were used to further track the  $\Sigma^+$  and to determine the beginning of the daughter proton track, thus establishing the decay point as the intersection of the two tracks. The downstream portion of the charged detector consisted of five additional MWPC's (C4-C8) and an analyzing magnet M3. These tracked and momentum analyzed the daughter protons, which were required to register in scintillator PC at the far downstream end of the spectrometer.

### 2.5.2 MULTIWIRE PROPORTIONAL CHAMBERS

The MWPC's used in this experiment were of standard design and had been used in several previous experiments. They are described in detail elsewhere.<sup>28</sup> Each chamber had two perpendicular sense planes with 2 mm wire spacing. These were made of 25  $\mu\text{m}$  diameter gold plated tungsten wires and were sandwiched between high voltage planes made of 75  $\mu\text{m}$  diameter Be-Cu alloy wires with 1 mm spacing. Chamber C4 was placed with its sense planes at a  $45^\circ$  angle to the x and y planes of the other chambers. Chamber C5 had an additional plane with  $2\sqrt{2}$  mm spacing placed at  $45^\circ$  to the other planes. The number of wires per

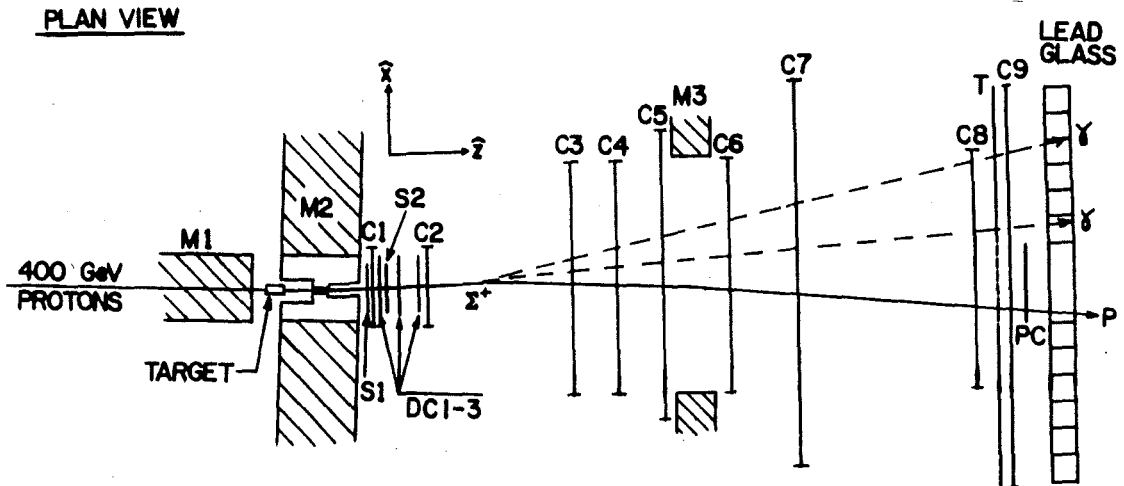


Figure 2.6 Plan view of the charged hyperon  $\Sigma^+ \rightarrow p\pi^0$  detector (not to scale). The  $\Sigma^+$  decay region stretched from the precession magnet M2 exit to MWPC C3. Chambers downstream of C3 tracked the decay proton, which also registered in scintillator PC, 40 m downstream of M2. The event shown represents a  $\Sigma^+$  decay where both  $\gamma$ 's from the  $\pi^0$  decay strike the lead glass calorimeter.

chamber started at  $24 \times 32$  wires for C1, and increased to  $640 \times 192$  wires for the last chamber, C9. A complete list is given in Table 2.1. The gas used was a combination of argon and freon bubbled through methyral at  $0^\circ \text{C}$ , resulting in a mixture with 90% argon, 10% methyral, and 0.1% Freon by weight. Typical operating voltages were -3.0 kV. Chamber gains and efficiencies were monitored by checking the pulse height of signals from sense wires illuminated by weak  $\text{Fe}^{55}$  x-ray sources.

The signal pulses from each wire were individually amplified to ECL levels ( $-0.75$  to  $-1.5\text{V}$ ) and then split into two signals: one which was fed into a fast "OR" for all the wires in a plane and one which was sent to an 850 ns delay. The fast OR signals from each chamber plane were sent to the electronics control room where they could be used in the trigger logic. In the event of a suitable trigger, an enable pulse sent back to the chambers allowed the delayed data to be latched and held until it was read out by the data acquisition system described in Section 2.8.1.

Chamber efficiencies, defined to be the percentage of times that a hit registered for each event trigger, were typically 99%. See Table 2.1. C1 and C2 exhibited lower efficiencies due to beam loading at intensities of  $2 \times 10^5$  particles/pulse measured at C1. Spatial resolution of the chambers was  $580 \mu\text{m}$ .

### 2.5.3 CHAMBER COORDINATE SYSTEM

The chamber coordinate system was established by removing the hyperon target and directing the 400 GeV proton beam onto the collimator aperture at 0 mrad incident angle. With the magnetic channel tuned to 400 GeV and the analyzing magnet M3 turned off, the resulting narrow beam defined the chamber centers. The +z direction was taken to be along the beam and +y was chosen to be vertically upward. The +x direction was then defined by the cross product  $\hat{y} \times \hat{z}$ . The chambers were perpendicular to the z axis, with wires parallel to the x and y axes. An exception was C4, which had wires aligned at 45° to these axes to allow resolution of hit ambiguities for multitrack events.

TABLE 2.1 MWPC characteristics.

		C1	C2	C3	C4*	C5**	C6	C7	C8	C9
No.of	x	24	128	256	128	320	316	640	256	640
Wires	y	32	128	128	128	320	128	192	128	192
Cham.	x	0.92	0.97	0.99	0.99	0.99	0.99	0.99	0.99	0.98
Eff.	y	0.92	0.96	0.99	0.99	0.99	0.99	0.99	0.99	0.99

\*C4 had u, v planes rotated 45° from x and y.

\*\*C5 u plane had 256 wires.

#### 2.5.4 DRIFT CHAMBERS

Drift chambers were chosen for the upstream spectrometer to allow accurate determination of the  $\Sigma^+$  track for events with a vertex in the decay region. The average DC spatial resolution of 300  $\mu\text{m}$ , as given in Table 2.2, was nearly twice as good as that of the MWPC's. Resolutions of  $\pm 0.12$  mrad for the decay angles could be obtained if the vertex occurred between DC1 and C2. Such accuracy was crucial since the typical decay angle was 1.0 mrad. The  $\Sigma^+$  momentum could be obtained with a resolution of  $\pm 7\%$  by tracing the upstream track back through the defining collimator to the target.

A chamber consisted of a set of x planes followed by a set of y planes, each set containing a plane and an ambiguity resolving plane offset by half a cell width. Cell sizes were 2.032 cm for the x planes, 3.048 cm for DC1 and DC2 y planes, and 6.096 cm for DC3 y. The

TABLE 2.2 Drift chamber calibration results.

CH	CELL SIZE cm	PED. ct	ROT. mrad	DRIFT VEL. cm/ct (cm/ $\mu\text{s}$ )	RESOL. $\mu\text{m}$	EFF.
1Y	3.048	66	4.5	0.001217 (4.87)	299	0.50
1X	2.032	87	21.2	0.001308 (5.23)	287	0.70
2Y	3.048	102	0.4	0.001229 (4.92)	328	0.22
2X	2.032	92	4.4	0.001282 (5.13)	281	0.70
3Y	6.096	67	0.2	0.001686 (4.82)	341	0.60
3X	2.032	110	5.9	0.001285 (5.14)	260	0.78



The chambers were borrowed from the University of Michigan and a detailed description of their construction exists in the literature.<sup>29</sup> For this experiment, a total of 40 wires was implemented. Signals were amplified at the chambers and then were carried via 400 ns long RG-58 cables to time-to-digital converters (TDC) in the electronics control room. The TDC's were 8 channel LeCroy model 2228A. Thirty-two channels were set for a counting rate of 250 ps/ct; the remaining eight channels, which serviced the large cells in DC3y, were set for a counting rate of 350 ps/ct. The long delay lines allowed the TDC clocks to be started by a signal from the fast trigger logic.

The chambers were filled with an 80/20 argon/CO<sub>2</sub> mixture and were operated at voltages of +2.7 kV. They were 60-70% efficient except for DC1y and DC2y, which had high voltage difficulties. See Table 2.2. All the chambers showed lowered efficiencies due to high charged particle fluxes. The beam in the decay region was distributed over only two or three cells for each chamber, resulting in heavy beam loading for those cells. These low efficiencies reduced the acceptance of events with a detectable change in the charged track direction at the decay point. In a Monte Carlo simulation, the percentage of these "kinked-track" events accepted from the total generated sample was 25%. When the drift chamber efficiencies in the simulation were all raised to 0.90, the acceptance increased to 31%.

### 2.5.5 DRIFT CHAMBER CALIBRATION

The drift chambers were calibrated by using fitted straight tracks from MWPC information and the average sum of the TDC counts for each DC half-cell. For calibration purposes, a half-cell was defined to be the space enclosed by a sense wire and a field shaping wire in one plane, and the field and sense wires directly behind them in the ambiguity resolving plane. Thus, a half-cell had a sense wire at both ends, and the sum of the counts recorded for any particle trajectory through the cells should remain constant. Using the average sums for each half-cell reduced errors involved in determining the maximum number of counts for a single wire and errors due to non-linearities in the drift velocity curves. Corrected average sums,  $XAV$ , were found by subtracting pedestals defined to be the midpoint of the rise in a plot of the number of events versus TDC counts for each chamber. The assumption was made that the relationship between TDC counts and distance in a half-cell was linear and that the cell widths and drift velocities were the same for all cells in a chamber.

The drift velocities were determined by using the least squares method on the constraint equation for the individual half-cell width  $L$  in a particular chamber,

$$L = V \cdot XAV_i + (m_i + m_0)d, \quad (2.1)$$

where  $V$  is the drift velocity,  $XAV_i$  is the average summed TDC counts,  $m_i$  is the average particle slope through half-cell  $i$  as determined by the MWPC's,  $m_0$  is the chamber rotation with respect to the  $xy$  plane,

and  $d$  is the 5.5 cm spacing between a plane and its ambiguity plane. The constraint equations for all the half-cells in a chamber were squared, multiplied by the number of events per half-cell, and added to form a weighted sum which was then minimized by setting the partial derivatives with respect to  $V$  and  $m_0$  equal to zero. The two resulting equations could be solved for the unknown chamber drift velocity  $V$  and the chamber rotation  $m_0$ . Results are listed in Table 2.2. Wire positions were determined by using the residuals between the calculated hits on the drift chambers and the extrapolated hits from the MWPC's. Residuals were 0.01 cm or less for all wires. Sampling large numbers of events in runs throughout the running period indicated that the drift velocities varied by about  $\pm 6 \mu\text{m}/\text{ct}$ , which is far below the single event resolution.

An alternate method which did not require the assumption that all the cell velocities in a chamber were the same was used as a check on the calibrations. The positions of the hits in the drift chambers, as determined by the MWPC's, were separated into 600  $\mu\text{m}$  bins and the average number of TDC counts per bin was then plotted for each wire. The drift velocity for an individual wire was determined by the slope of the curve, and the pedestal and wire position were obtained from the intersection of the slopes from each half of the cell. Data within 1.3 mm of the sense wire did not follow the assumption of linearity and were excluded from the determination of the slopes. For accuracy, this method required large statistics and uniform illumination of the cells by the beam, conditions generally not seen in the  $\Sigma^+$  beam. Results for

the center cells, which did have large statistics, agreed with the first method, reinforcing the validity of its assumptions.

#### 2.5.6 ANALYZING MAGNETS

The momenta of the  $\Sigma^+$  and the decay proton were analyzed by magnets M2 and M3, respectively. As mentioned earlier, the  $\Sigma^+$  momentum for events with a visible decay was obtained by extending the  $\Sigma^+$  track back through the magnetic channel in M2 and constraining it to fit the 4 mm defining collimator and the 6 mm target. The momentum of the daughter proton was determined by M3, a ferric superconducting dipole (iron yoke, superconducting coil) with a maximum field integral of 3.17 T-m. The 2.5 m long channel through magnet M3 was 20.3 cm high and 61 cm wide. For  $\Sigma^+$  data taking, the field was set near maximum to give transverse momentum  $p_t = 0.95$  GeV/c. Lead glass calibration runs with  $e^+e^-$  pairs used field settings with  $p_t = 0.58$  GeV/c. Positively charged particles were bent in the negative x direction.

#### 2.5.7 SCINTILLATION COUNTERS

Various scintillation counters with photomultiplier tubes served to define the accepted particle beams. A hit registering in S1 indicated that a charged particle had entered the decay region. See Figure 2.6. The signal from this counter was used as a timing marker for other data signal inputs to the fast trigger logic. Mounted just downstream of chamber DC1, halo counter S2 vetoed events with charged

particles outside the collimated hyperon beam. The counter was 10 cm wide by 30 cm high with a hole 5.0 cm by 3.8 cm centered on the beamline.

A third counter, PC, was located just in front of the lead glass array at the end of the spectrometer. It was 10 cm high by 30 cm wide, large enough to contain 94% of the decay proton beam. Seventy centimeters in front of the lead glass was an additional counter, T, which matched the lead glass acceptance. It had a hole corresponding to the size and position of the counter PC, and its function was to veto charged tracks outside the accepted area covered by PC. The relative positions of these counters are shown in Figure 2.7.

#### 2.5.8 REDUCTION OF MULTIPLE SCATTERING

Helium-filled bags of polyethylene were used in the spectrometer to reduce multiple scattering of the decay protons by air molecules. The bags filled the spaces between chambers from C3 to C8, including the analyzing magnet channel. An evacuated aluminum pipe, 8.5 m long with a diameter of 40 cm, was placed between chambers C2 and C3 to reduce scattering in the decay vertex region. The total amount of material in the beam was  $\sim 3.6\%$  of a radiation length, or  $\sim 1\%$  of a nuclear interaction length.

## 2.6 GAMMA DETECTORS

### 2.6.1 LEAD GLASS ARRAY

The primary detector of gammas from  $\pi^0$  decays was a 70 block lead glass array at the far downstream end of the spectrometer. The F2 grade blocks were 10.06 cm square by 38.4 cm ( $12 X_{\text{rad}}$ ) long and were individually wrapped in aluminum foil and light proof tape. Long axes parallel to the beam, the blocks were stacked in five horizontal rows, each row offset half a block from the rows above and below. See Figure 2.7. The front face of the array was  $\sim 145$  cm by 50 cm, which covered the region populated by gammas which passed through the aperture of the analyzing magnet M3. Since the  $\Sigma^+$  event trigger required a charged track in the spectrometer and a shower in the glass, it was necessary to eliminate showers from charged hadrons. Removing the three blocks shadowed by the proton counter PC prevented proton showers from triggering the array. Events with charged tracks outside the area of the counter were vetoed by the scintillation counter T.

The Cherenkov light from the showers in the glass was collected by RCA 6342A/V1 ten-stage photomultiplier tubes mounted in a rack behind the array. The tube faces fitted into 5.08 cm diameter O-rings epoxied to the backs of the blocks and were pressed against the glass by springs in the rack. The coupling between the blocks and the phototubes was glass-to-glass. Typical operating voltages for the tubes were -1500 V.

The array and phototubes were enclosed in a light-tight steel box which was mounted on wheels. For  $\Sigma^+$  data taking, one edge of the hole was lined up on the chamber center line, with the hole lying entirely in the  $-x$  region. For  $e^+e^-$  calibration runs, the array was moved perpendicularly to the beam so that different sections of the glass could be illuminated by the charged pairs.

The anode signals were discriminated at the 30 mV level, corresponding to 1 GeV in the glass, and combined in a logical OR. Thus, 1 GeV registering in any glass block generated a logic pulse which served as the lead glass trigger GOR. The dynode pulses were

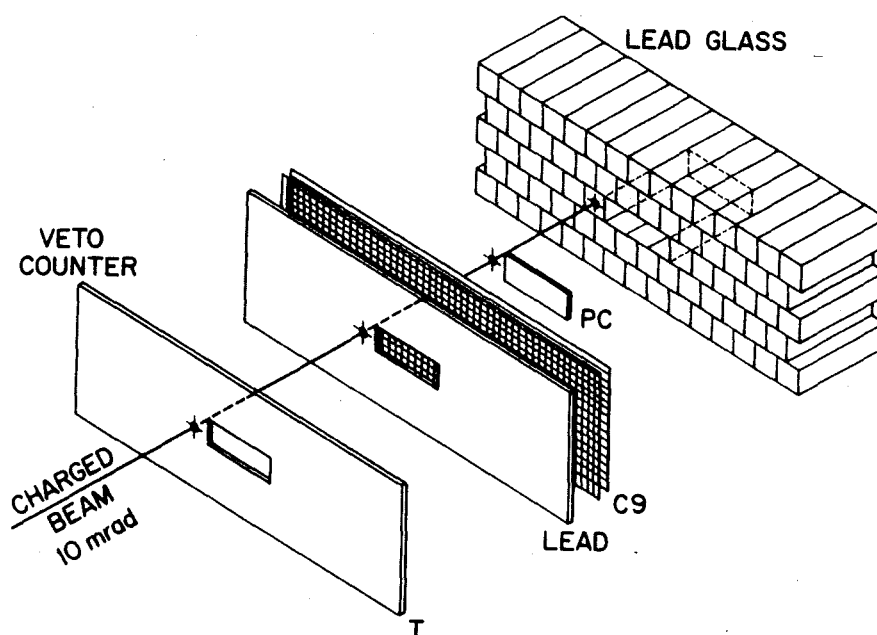


Figure 2.7 Lead glass array and associated gamma detectors. The lead glass measured gamma energy and gave an estimate of the shower position. The scintillator - lead - MWPC sandwich enhanced the gamma position determination. Counter PC was used in the trigger to detect decay protons and counter T acted as a veto for charged tracks hitting the glass.

delayed and transported to the electronics control room, where they were attenuated by 16 db. The signals were then fed into LeCroy 2249A 12-channel analog-to-digital converters (ADC). The channels were set for a sensitivity of 0.25 pC/count, with 1024 maximum counts. Pulses were integrated over a 100 ns gate generated by the event trigger. With a typical conversion factor of 0.08 GeV/count, the maximum energy which could be recorded by any channel was  $\sim 82$  GeV. This compares favorably with the maximum gamma energy of 80 GeV, which was typically spread over two or three blocks.

#### 2.6.2 LEAD GLASS CALIBRATION

The preliminary calibration constants relating energy to ADC counts for the lead glass were obtained by illuminating the glass with electron-positron pairs and comparing their momenta, as measured in the spectrometer, with the number of counts deposited in the ADC's. Electron pairs were created by allowing a neutral beam to convert in a thin sheet of lead placed at the collimator exit. A low intensity 200 GeV proton beam incident on the hyperon target at an angle of 0 mrad was used to produce the neutral beam. Collimator blocks 6 through 8 were removed and the exit block was replaced by a block with an 11 mm diameter hole drilled straight through its center. With the hyperon magnet turned on full field, charged particles were swept out of the collimator channel. The lead sheet, a third of a radiation length thick, was mounted on the downstream side of scintillator S1. An additional counter S3 was placed just downstream of the lead. The



hole in the counter T at the back of the spectrometer was also covered by scintillator. The  $e^+e^-$  event trigger,  $\overline{S1} \cdot S3 \cdot C3 \cdot T$ , required a neutral particle in S1 and charged particles in S3, chamber C3, and T.

The electron pairs could be made to illuminate the entire area of the array by controlling their trajectories with the spectrometer analyzing magnet and with an additional vernier magnet replacing C1. The vernier magnet was 60 cm long and had a horizontal field which split the pairs in the vertical direction. The analyzing magnet was set for  $p_t = 0.56$  GeV/c, to split the pairs horizontally. By rolling the glass array to three positions on a line perpendicular to the beam and operating the vernier at 5 field settings, each block in the array could be calibrated by several electrons with energies in the range of 3 to 60 GeV. The  $e^+e^-$  calibration data were taken after the  $\Sigma^+$  data taking ended.

The information from the MWPC's and the analyzing magnet was used to reconstruct the vee-like topology of the  $e^+e^-$  pairs and to determine the electron energies and positions in the glass. The calibration constants  $c_i$  for each block were adjusted to minimize the function

$$F = \sum_j (E_j - \sum_i c_i S_{ij})^2, \quad (2.2)$$

where  $j$  ranged over all the showers in the glass,  $i$  was the block number for blocks involved in shower  $j$ ,  $E_j$  was the measured spectrometer energy for shower  $j$ , and  $S_{ij}$  was the number of counts in block  $i$  for shower  $j$ . The average calibration constant found by this procedure was 0.086 GeV/ct. The spatial resolution was determined by

studying the difference between the position measured in the spectrometer and that given by the shower centroid. The FWHM of the difference was 6.0 cm and the sigma was 2.0 cm for both x and y. A standard deviation of 2.4 cm was chosen as the glass resolution for reconstruction purposes. Plots of  $(E_g - E_s)/\sqrt{E_s}$ , where  $E_g$  is the energy in the glass and  $E_s$  is the measured track energy, for all hits centered in each individual block yielded an energy resolution of  $0.32\sqrt{E}$ , where  $E$  was in  $\text{GeV}/e^2$ . The plots exhibited non-Gaussian, high energy tails, which indicated energy lost out the back and sides of the array.

The final calibration constants were obtained from the  $\Sigma^+$  data. The charged track information and the gamma cluster positions for  $\Sigma^+$  candidates with two cluster in the glass were fitted to the  $\Sigma^+ \rightarrow p\pi^0$  hypothesis. The calculated gamma energies were then used to solve for the calibration constants by the method described above. These "bootstrap" values were found to be consistent with the  $e^+e^-$  calibration constants.

### 2.6.3 MWPC GAMMA DETECTOR - C9

Improved spatial resolution for the gammas from the  $\pi^0$  decay could be obtained by using lead converters in front of MWPC's and searching offline for clusters in the chambers. MWPC C9, with a two radiation length thick lead sheet shadowing the glass acceptance, was placed 30 cm in front of the array. See Figure 2.7. A  $10 \times 30$  cm hole matching the proton counter PC was cut in the lead to allow the charged

beam to pass through without creating hadron showers. The scintillation counter T was just upstream of the lead and, as mentioned before, acted as a veto for events with charged tracks in the region expected to contain only gamma rays.

Clusters were located in the offline analysis by searching a window in the chamber of  $\pm 4.3$  cm in x and y around the position of the gamma cluster found in the glass array. The mean and variance of the chamber cluster position were calculated for x and y separately according to the equations:

$$\bar{x} = \frac{1}{N} \sum x_j \quad (2.3)$$

$$\sigma^2 = \frac{1}{N} \sum (x_j^2 - \bar{x}^2)$$

for all struck wires  $x_j$  in the window. If  $\sigma > 1.5$  cm, the chamber position information was ignored and the glass data and resolution were used instead. Only 65% of the gammas formed satisfactory chamber clusters, with a mean sigma of 0.5 cm.

#### 2.6.4 MWPC GAMMA DETECTOR - C5

A second scintillator-lead-MWPC "sandwich" was used upstream of the analyzing magnet M3 to expand the acceptance to include gammas which were outside the magnet aperture and undetected by the lead glass array. The arrangement is shown in Figure 2.8. Two pieces of lead, 20 cm high by 62 cm wide and 2 radiation lengths thick, were fitted to

the front of chamber C5, one above and one below the magnet aperture. Each lead-chamber combination was then sandwiched between two matching pieces of scintillator. Neutral particles travelled through the front scintillator, A1 or A2, without interacting, converted in the lead, showered in the chamber, and registered in the back scintillator, A3 or A4. The counters were latched and read during data taking and were interrogated in the offline analysis for  $\overline{A1} \cdot A3$  and  $\overline{A2} \cdot A4$  coincidences which implied gamma conversions. The chamber was then searched for clusters, the additional u plane helping to resolve hit ambiguities. One fourth of the  $\Sigma^+$  events had gammas which converted in C5, the average spatial resolution being 0.5 cm. Although no energies were

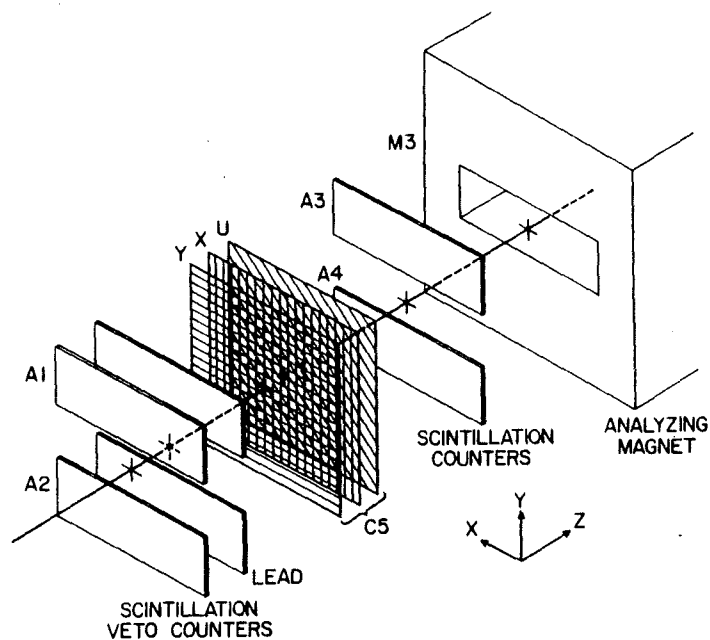


Figure 2.8 Scintillator - lead - MWPC - scintillator sandwich used to detect gamma position upstream of the momentum analyzing magnet. Counters A1 and A2 acted as charged particle vetoes, the  $2X^{\text{rad}}$  lead acted as a converter for gamma to electron showers, and MWPC C5 planes located the shower positions.

obtained for these gammas, the cluster position, together with the energy and position information in the glass for the second gamma, allowed a three constraint fit of the  $\Sigma^+$  decay to be made.

## 2.7 TRIGGER LOGIC

Coincidences of the fast electronic signals from the MWPC's, the lead glass, and the various scintillators in the detector were used to form a "good event" trigger, GE, about 600 ns after the event entered the detector. The  $\Sigma^+$  trigger was made as loose as possible by requiring only that a charged track entered the decay volume, a charged track traversed the downstream spectrometer, and at least one neutral particle of sufficient energy converted in the lead glass array. The charged tracks were defined by a coincidence of signals from the scintillator S1, the fast OR for C3, and the proton counter PC, and no signal from S2. This coincidence was logically represented as

$$S1 \cdot \overline{S2} \cdot C3 \cdot PC .$$

A shower from a neutral was determined by the glass OR, with no signal from the charged veto T, and was represented as

$$\overline{T} \cdot GOR .$$

The  $\Sigma^+ \rightarrow p\pi^0$  event trigger was then given as

$$\Sigma^+ = S1 \cdot \overline{S2} \cdot C3 \cdot PC \cdot \overline{T} \cdot GOR .$$

Mixed in with the  $\Sigma^+$  trigger was a prescaled portion of the positive

beam tracks in the detector, defined as

$$p = S1 \cdot \overline{S2} \cdot PC ,$$

making the good event trigger

$$GE = \Sigma^+ + \frac{P}{1024} .$$

The beam tracks were included for acceptance and background studies and represented about 6% of the total triggers. MWPC signals were excluded from the p coincidence in order that the chamber efficiencies might be determined.

## 2.8 DATA ACQUISITION

### 2.8.1 ELECTRONICS

The good event trigger GE formed by the fast logic coincidences was used to generate enable gates to the various detectors, an inhibit to prevent further data from accumulating in the apparatus, and a data read signal. Enable pulses were sent to the TDC's as clock starts, to the ADC's as a 100 ns wide gate, and to the MWPC's as a 100 ns wide gate on the wire latches. The enable to the MWPC latches, for example, was timed to arrive ~850 ns after the event entered the detector. The inhibit pulse prevented acceptance of data from later events until the existing data had been read into a PDP-11 computer.

The read signal went first to the MWPC's, where it cascaded through the chambers until it stopped at latched data, which was then

transferred to the PDP-11 direct memory access via Camac interface. The latches were reset and the read continued until all chambers had been interrogated. The TDC's, ADC's, and various latches were then read in and reset for data taking. An event record consisted of up to 240 words and took about 0.7 msec to be read in. Data were written to memory buffers at a high rate and then transferred to disc at a lower rate as the buffers became filled. The disc contents were written to 800 bpi tape at the end of the beam spill. Also written to tape at this time were scaler records of various rates and triggers. Approximately 200 events per spill were recorded, the data rate limited by the singles rate in the drift chambers. In between spills, the ADC's were again read to provide a continuous monitor on their pedestals.

### 2.8.2 DATA TAPE CONTENTS

Data were written to tape at the rate of one tape per hour: two tapes at +5 mrad production angle alternating with two tapes at -5 mrad. A total of 48 tapes were taken, 24 at each angle, each containing ~52,000 events. The total data sample included 2.5 million events, of which 6% were  $p^+$  beam triggers. Also taken were two tapes for chamber center calibration and three  $e^+e^-$  tapes for lead glass calibration.

## CHAPTER 3: EVENT RECONSTRUCTION AND SELECTION

## 3.1 INTRODUCTION

The reconstruction programs transformed the raw data information on the tapes to kinematic parameters necessary for the analysis of the  $\Sigma^+$  decay. Wire addresses, TDC counts, and ADC counts were decoded into corresponding spatial positions and energies, which were subsequently fed into the reconstruction program. Reconstruction occurred in three major steps:

1. Pattern recognition: The chamber hit positions were used to reconstruct charged tracks, while information from the lead glass and other detectors was used to reconstruct gammas. The event topology was then tested for the  $\Sigma^+ \rightarrow p\pi^0$ ,  $\pi^0 \rightarrow 2\gamma$  decay signature: a single charged track in the spectrometer (preferably with distinguishable parent and daughter tracks), a gamma shower in the lead glass, and, if detected, a second gamma in any of the detectors.
2. Kinematic fitting: Events with the proper decay patterns were kinematically fit to the simplified  $\Sigma^+ \rightarrow p\pi^0$  decay hypothesis on the basis of the charged track data alone, or to the global  $\Sigma^+ \rightarrow p\pi^0$ ,  $\pi^0 \rightarrow 2\gamma$  hypothesis, which incorporated both charged track and gamma information.



3. Event selection: The surviving event sample was cut to exclude background and  $\Sigma^+$  events unsuitable for polarization and magnetic moment analysis. Studies of possible contamination from unwanted decays and Monte Carlo simulation of the experiment were used to determine the cuts.

The flow of events through the reconstruction program and event selection process is shown schematically in Figure 3.2.

### 3.2 CHARGED TRACK RECONSTRUCTION

The charged track reconstruction program proceeded in three major steps. The daughter track was first reconstructed by locating a track downstream of the decay volume and then searching upstream in the decay region for chamber hits which fit the same track. These tracks were then checked for target pointing. Tracks which originated directly from the target indicated that the particle under study was a beam particle and not the product of a  $\Sigma^+$  decay. Once the daughter tracks were identified, the search for the parent  $\Sigma^+$  track was initiated at the target and continued back through the upstream chambers.

The preliminary daughter track reconstruction program looked for a single, positively charged track in the spectrometer downstream of the decay volume. The decoded MWPC wire hits were searched for a track that had at least 2 hits before and 2 hits after the momentum analyzing magnet M3 in the x or bend plane, and at least 3 hits in the y plane.

Reconstruction quality codes are listed in Table 3.1. Since the MWPC efficiencies were nearly all 98-99%, the 10% of the data removed by this single track search (Codes 1-4) was mostly multiple track events. Although the event trigger was designed to be as loose as possible, only requiring at least one charged track in the spectrometer and one neutral in the lead glass, the data sample was remarkably free of multi-track events. The downstream track reconstruction was next extended to the two MWPC's and three DC's in the decay region. A hit was added to the track if the minimizing  $\chi^2$  for a straight line fit through the selected points changed by less than 4.5 when that hit was added.

The central target and collimator positions in y and an equivalent source point in the bend plane x added to the track to test for target pointing. (See Figure 3.1 for a description of the equivalent source point). If the change in  $\chi^2$  per added point was less than 4.5, the track was assumed to be that of a non-decaying particle produced at the target (Code 5). These beam tracks, 45% of the events which passed the single track requirements, included events from prescaled beam triggers which did not require gamma information and from  $\Sigma^+$  triggers with accidentals in the lead glass array. For 90% of the accidental cases with two gammas in the glass, the energy deposited did not reconstruct a  $\pi^0$  mass. Many of the clusters appeared to be residual energy from events just prior to the desired event gate. Kinematic cuts (Codes 6-7) on the daughter momentum and preliminary calculation of the decay angle helped cut down background contamination, particularly from  $\Sigma^+ \rightarrow n\pi^+$  decays.

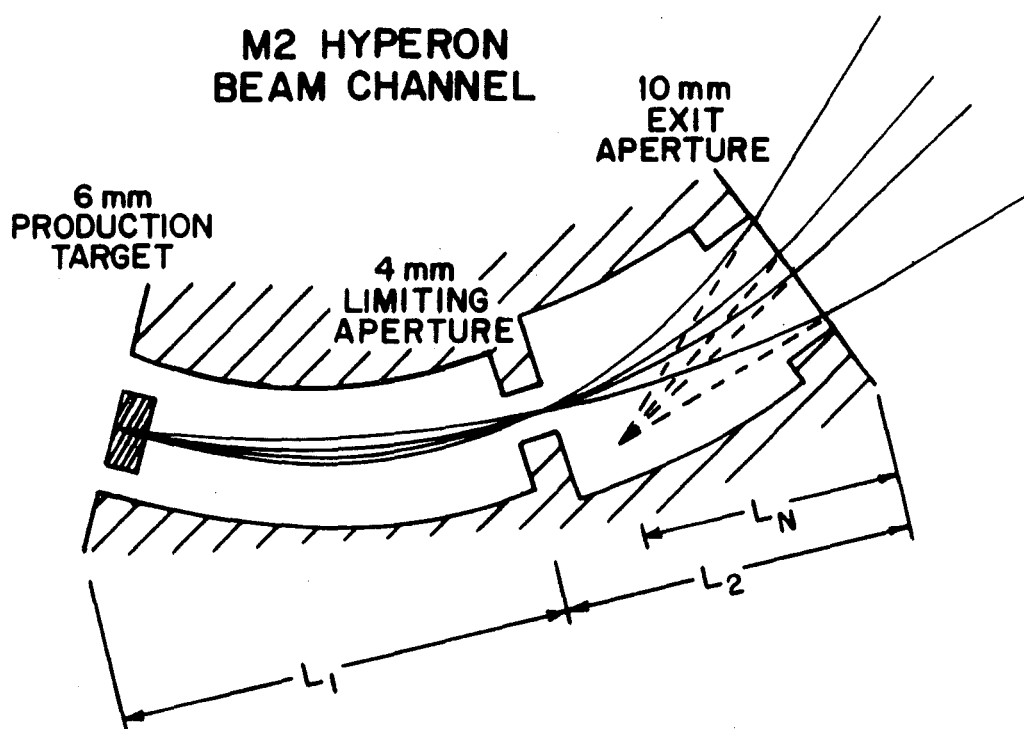


Figure 3.1 Equivalent source point in the bend plane of the precession magnet. If target and collimator aperture are small enough, all particles appear to emanate from a point a distance  $L_N = (L_2^2 + L_1 L_2) / (2L_2 + L_1)$  from the magnet exit. The actual virtual source is smeared due to the finite aperture sizes. The transverse dimensions and bend angles are exaggerated for clarity.

With the downstream track determined, the search for the upstream, or parent, track was started. Reconstruction of the  $\Sigma^+$  track required hits in the first two chambers and forced the fit through the source points in the collimator. Events with Codes 8-10, 88% of the candidate sample, could not reconstruct the parent track. Although some of these events had decay kink angles too small to be detected, the majority had vertices upstream of the decay region due to the short  $\Sigma^+$  lifetime. A  $\chi^2$  cut at 38 for the overall geometric track fit was applied when the upstream and downstream tracks were joined at the vertex (Codes 11-12). This  $\chi^2$  for a kinked track hypothesis was also required to be significantly better than a straight line fit to the same points (Code 13). Events with a mathematically unfeasible error matrix for the fit were eliminated from the sample (Code 14). Kinematic cuts on the parent momentum and momentum resolution, and a cut on the calculated kinetic energy of the proton in the  $\Sigma^+$  rest frame were also applied (Codes 15-17).

The events which survived all these cuts had well defined parent and daughter tracks and a decay vertex. They were subjected to a one constraint kinematic fit to the decay hypothesis  $\Sigma^+ \rightarrow p\pi^0$  (Codes 18-19). Only the upstream and downstream slopes determined by the chamber information, the source points in the collimator, and the  $\Sigma^+$  mass were used in the fit, which is described in detail in Section 3.4. Events which fit this decay hypothesis with  $\chi^2 \leq 7.5$  were labeled good kink sigmas and could be used to analyze the polarization and magnetic moment without the additional information from the gamma detectors.

Events in the total data sample of 2.5 million fell into four major categories according to the charged track reconstruction codes:

1. Kinematic and geometric reconstruction failures Codes 1-4,6,7,11,14,15	478,000 Events
2. Non-decaying beam tracks Code 5	1,005,000 Events
3. Non-kink tracks	
a. Early decays; Codes 8,9	615,400 Events
b. Kink track failures; Codes 12,13,16-18	273,800 Events
4. Good kink $\Sigma^+ \rightarrow p\pi^0$ decays Code 19	<u>105,800 Events</u>
$\Sigma^+$ candidates (categories 3 and 4)	995,000 Events

The failures in category (1) and the beam tracks in category (2) were later removed from the sample of  $\Sigma^+$  candidates. The beam tracks were used to monitor run-to-run variations of beam offsets at target and collimator and other useful parameters. Both the non-kink and good kink events were candidates for the global fit to the hypothesis  $\Sigma^+ \rightarrow p\pi^0$ ,  $\pi^0 \rightarrow 2\gamma$ , but many of the non-kink events were later removed from the sample because both gammas were not detected. Although the good kink events could be analyzed without the gamma information, the addition of this information helped eliminate background contamination and improved the acceptance for forward and backward decays.

TABLE 3.1 Charged track pattern recognition codes.

1. Cannot find two chambers outside decay region with single hits in y (non-bend) plane.
2. Cannot find at least one more y hit which fits line determined by single y hits in two chambers.
3. Cannot find tracks in x (bend) plane with 2 chamber hits both upstream and downstream of analyzing magnet.
4. Bend plane tracks do not meet in magnet.
5. Target and collimator points fit downstream track with change in  $\chi^2 < 4.5$  per added point (beam tracks).
6. Momentum below kinematic limit of 60 GeV/c for decay product.
7. Tentative decay angle greater than kinematic limit.
8. All MWPC hits on downstream track (no detectable kink).
9. All MWPC and DC hits, except first MWPC, on downstream track (evidence for early decay, but not enough for reconstruction).
10. x hit from first MWPC missing.
11. Closest approach of downstream track and tentative upstream track  $> 1$  cm.
12. Geometric  $\chi^2 > 38$  or  $\Delta\chi^2 > 6$  when vertex is added.
13. Difference in  $\chi^2 > 14$  for kinked and straight line fits to track.
14. Error matrix elements for fit not physical.
15. Momentum of upstream track  $< 60$  GeV/c.
16. Momentum resolution of upstream track  $\Delta p/p > 10\%$ .
17. Calculated kinetic energy of proton in  $\Sigma^+$  rest frame more than 12 MeV from expected 190 MeV.
18. Kinematic  $\chi^2 > 7.5$  for 1-C fit to  $\Sigma^+ \rightarrow p\pi^0$  hypothesis.
19. Kinematic  $\chi^2 \leq 7.5$  for  $\Sigma^+ \rightarrow p\pi^0$  fit (good kink event).



### 3.3 GAMMA RECONSTRUCTION

The primary gamma detector was the 70 block lead glass array, which was required to have a signal greater than 1.0 GeV for the event trigger. The array was searched for clusters, and the cluster positions and energies were calculated. Various tests, listed in Table 3.2, were then applied to the cluster information. Clusters were removed if the charged track in the spectrometer could be traced to the blocks containing the shower (Code 1). The largest category of cluster rejects (Codes 2,3), had energies below a selected threshold of 3 GeV and appeared to be residual energy from particles hitting the glass just before the event gate opened. The majority of  $\Sigma^+$  triggers which reconstructed as beam tracks had these low energy clusters and no other signal in the glass, indicating that the particle flux in the apparatus was high for the lead glass trigger gate width. See Table 3.3. Hadron showers were identified by a larger lateral spread of the shower than was expected for a gamma with the deposited energy (Codes 4,5). The energy resolution of the clusters was taken to be  $0.32 \sqrt{E} \text{ GeV/c}^2$  from electron shower studies.

The position resolution of the shower, taken to be 2.4 cm, could be improved by searching the lead-MWPC gamma detector, C9, placed immediately upstream of the glass array. If a cluster of hits with position resolution less than 1.5 cm was found, then the chamber position and resolutions were used instead of the PbG values (Codes 8-9). About 65% of the gammas hitting the lead glass produced acceptable showers in the C9 detector. If only one surviving gamma was



detected in the glass, the lead-MWPC detector C5, just upstream of the M3 analyzing magnet, was searched for gammas that missed the magnet aperture and would therefore not strike the PbG array. About 60% of the expected gammas had showers with an acceptable position resolution of 1.5 cm or less. Showers located in this detector had no energy information.

Once the clusters had been identified as gamma showers, the events in the candidate sample could be labeled according to the four detection types:

1. No gammas detected	350,500 Events
2. One gamma in PbG	453,600 Events
3. Two gammas in PbG	129,100 Events
4. Split gammas: 1 in PbG, 1 in C5	61,800 Events

Events with no gammas detected (Code 10) and a very small number of events with more than two surviving clusters in the glass (Code 7) were removed from the data set. Since the kinematic fitting programs required two detected gammas for the reconstruction of events in the non-kink track category, events of this type with only one surviving gamma were eliminated from further analysis (Code 11). The event sample divided into categories is shown in Table 3.3. Only those events in the outlined region were considered as candidates for the kinematic fitting programs.

TABLE 3.2 Gamma reconstruction codes.

1. Shower identified with proton track
2. Total energy in PbG  $< 3$  GeV
3. Cluster energy  $< 3$  GeV
4. Energy deposition pattern of hadron
5. Calculated error in energy  $> 4.2 \text{ GeV}/c^2$
6. Cluster centers less than one block width apart
7. More than 2 clusters in PbG
8. No hit in C9 detector within 4.3 cm of PbG hit
9. Position resolution in C5 or C9 detectors  $> 1.5$  cm
10. No gammas surviving PbG cluster tests
11. Non-kink track event with only one gamma detected

TABLE 3.3 Pattern recognition event types for events with reconstructable charged tracks. The outlined area indicates which events had sufficient information for kinematic fitting to the  $E^+$  decay hypotheses. Categories are described in Sections 3.2 and 3.3.

	No Gammas	One Gamma	Two Gammas	Split Gammas	Totals
Beam Track	88,000	225,000	645,000	47,000	1,005,000
Non-Kink Track	350,000	407,000	87,900	44,300	889,200
Kink Track	500	46,600	41,200	17,500	105,800
Totals	438,500	678,600	774,100	108,800	2,000,000

### 3.4 KINEMATIC FITS

Events shown by the pattern recognition program to have the proper decay signature were further tested to see if they satisfied the kinematic constraints of the decay mode. The requirements for conservation of energy and momentum were added to the event geometry and a  $\chi^2$  probability was calculated for the assumption that the event was a  $\Sigma^+$  decay. Two types of kinematic fits were applied to the data:

1. Kink track fit to  $\Sigma^+ \rightarrow p\pi^0$  hypothesis.
2. Global fit to  $\Sigma^+ \rightarrow p\pi^0$ ,  $\pi^0 \rightarrow 2\gamma$  hypothesis.

The fit in category (1) could only be applied to events with established parent and daughter tracks from the geometric fit in the pattern recognition program. The gamma information merely provided the event trigger and was not used in this fit, which was used primarily as a check on the global fit.

The event parameters from both the geometric fit for a kinked track hypothesis and the kinematic fits for the two  $\Sigma^+$  decay hypotheses were determined using the minimized chi-square method. The measured inputs, such as chamber hits, slopes, or vertices, and the constraint equations for energy and momentum conservation were used to calculate the parameters such as momenta and decay angles which describe the fit hypothesis. The minimum chi-square probability for a fit to a hypothesis with  $i$  parameters is

$$\chi_N^2 = \sum_i \frac{(x_i - x_i^0)^2}{\sigma_i^2} \quad (3.1)$$

where  $x_i$  is the decay parameter calculated by the measured inputs and constraints, and  $x_i^0$  is the adjusted value of the same parameter which, in concert with the adjusted values for all the other parameters, minimizes the sum in Equation 3.1. These adjusted parameters were the best fit to the data and were assumed to have the actual values which describe the event. The number of degrees of freedom,  $N$ , was the difference between the number of inputs and the number of parameters. Any parameter with a relatively large measurement error  $\sigma_i$  was given less weight in the calculation and was allowed to vary more than the more precisely measured parameters. If the working hypothesis was the correct one for the sample of events, the distribution of chi-square probabilities would match that expected for an  $N$ -degree-of-freedom fit with mean  $N$  and variance  $2N$ .

For the kinematic kink track fit, the 4 slopes describing the two tracks, the 3 measured vertex coordinates, the 2 collimator source coordinates, and the  $\Sigma^+$  conservation laws were used to calculate the  $\Sigma^+$  3-momentum, the 3 fitted vertex coordinates, and 2 decay angles. With 9 inputs and 8 parameters, this was a one degree of freedom, or one constraint (1C) fit. The term constraint was used for the degrees of freedom in the kinematic portion of the decay model, that is, the part which distinguishes this particular decay from other modes with the same geometry.

In the global fit, all the measured data from chambers and gamma detectors were included. The number of degrees of freedom was

$$N + M - 10 \quad (3.2)$$

where  $N$  was the number of chamber hits in both  $x$  and  $y$ ;  $M$  includes some or all of the possible additional inputs -- virtual source, gamma energies, gamma positions; and the 10 parameters describing the decay mode were the  $\Sigma^+$  3-momentum, the 3 vertex coordinates, and the 4 angles between the decay products. A diagram of the decay is shown in Figure 3.3a. Since this fit started with the chamber hit information instead of the calculated slopes from the geometric fit, the resulting

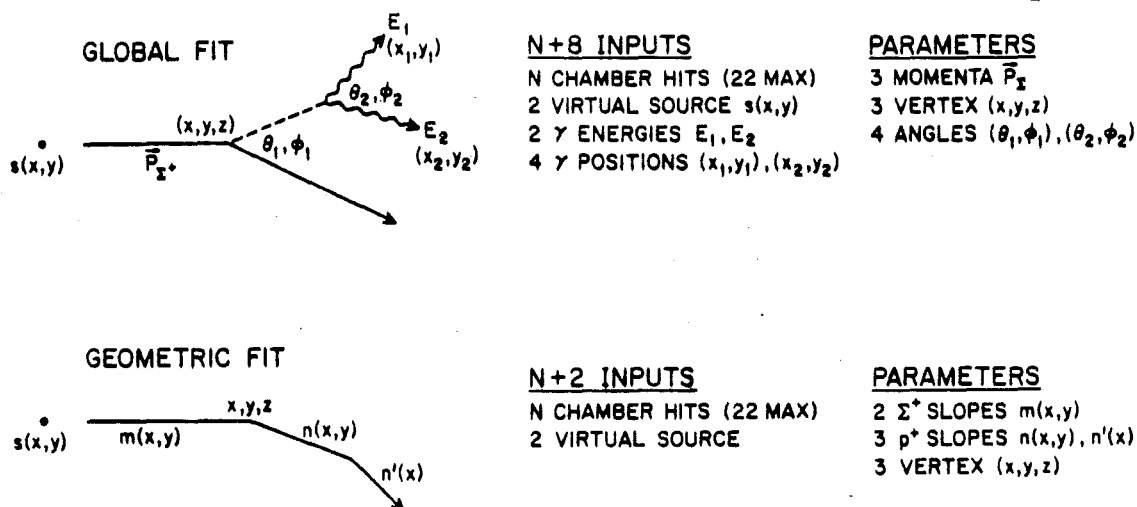


Figure 3.3 (a) Diagram of an event fitting the decay hypothesis  $\Sigma^+ \rightarrow p\pi^0$ ,  $\pi^0 \rightarrow 2\gamma$ . The parameters used to define the decay in the global minimizing  $\chi^2$  fit are listed, along with the number of measured inputs for an event with the maximum number of inputs (kink,  $2\gamma$ ). The number of degrees of freedom is the number of inputs minus the number of parameters. (b) Diagram of the charged track information used in the geometric  $\chi^2$  fit.

chi-square probability  $\chi^2$  includes both the geometric and kinematic contributions to the fit. The more interesting kinematic  $\chi^2$  was approximated by subtracting a geometric  $\chi^2$  for the charged track from the global  $\chi^2$ . This geometric fit involved the same number  $N$  of chamber hits, but the number of additional inputs was restricted to 2 for the virtual source point. The number of parameters, as shown in Figure 3.3b, was 8 and the number of degrees of freedom was, therefore,

$$N + 2 - 8 . \quad (3.3)$$

Subtracting this from the number of degrees of freedom for the global fit in Equation (3.2) left

$$C = M - 4 \quad (3.4)$$

for the kinematic degrees of freedom, or constraints. Events missing one gamma had 1-C fits, events with one gamma in detector C5 and one in the lead glass had 3-C fits, and events with both gammas in the lead glass array had 4-C fits. The goodness of fit and the position of  $\chi^2$  cuts were dependent upon the number of constraints, since the chi-square probability distributions had expected means and variances  $C$  and  $2C$ , respectively. Plots of the kinematic  $\chi^2$  distributions are shown in Section 3.7.

### 3.5 MONTE CARLO PROGRAM

A computer simulation of the experiment, or Monte Carlo, was a necessary tool for understanding the experiment and determining how

much confidence should be placed on the results. Measured physical dimensions, theory, known properties, and information from the real data sample were used to recreate the apparatus and the decay modes of interest. Whenever possible, use of measured data parameters dependent upon the properties under study was avoided to prevent compromising the technique. The Monte Carlo program was particularly helpful in identifying background contamination and biases. Comparisons between Monte Carlo and experimental data gave estimates of the sample purity, the reconstruction efficiencies, and systematic errors.

The first step in building the MC program was to mock the experimental set-up -- the positions and sizes of the apertures, the magnetic field values, and the positions, efficiencies, and resolutions of the various detectors. The acceptance of the apparatus was determined by generating a beam of non-decaying particles and testing it against the apertures. Tracks were generated by selecting a source point in the target -- randomly distributed in length  $z$  and normally distributed in radius  $r$ ; a point at the defining collimator aperture -- randomly distributed; and a momentum. The particle orbit for that momentum was then traced through the two generated points. The momenta were chosen from a flat distribution ranging from 90 GeV/c to 400 GeV/c. The collimator acceptance, with and without the  $\Sigma^+$  trigger acceptance, is plotted in Figure 3.4. Also shown is the total acceptance in the apparatus for events allowed to decay as polarized  $\Sigma^+ \rightarrow p\pi^0$ . In all cases the acceptance falls rapidly below 180 GeV/c and cuts off at 120 GeV/c.

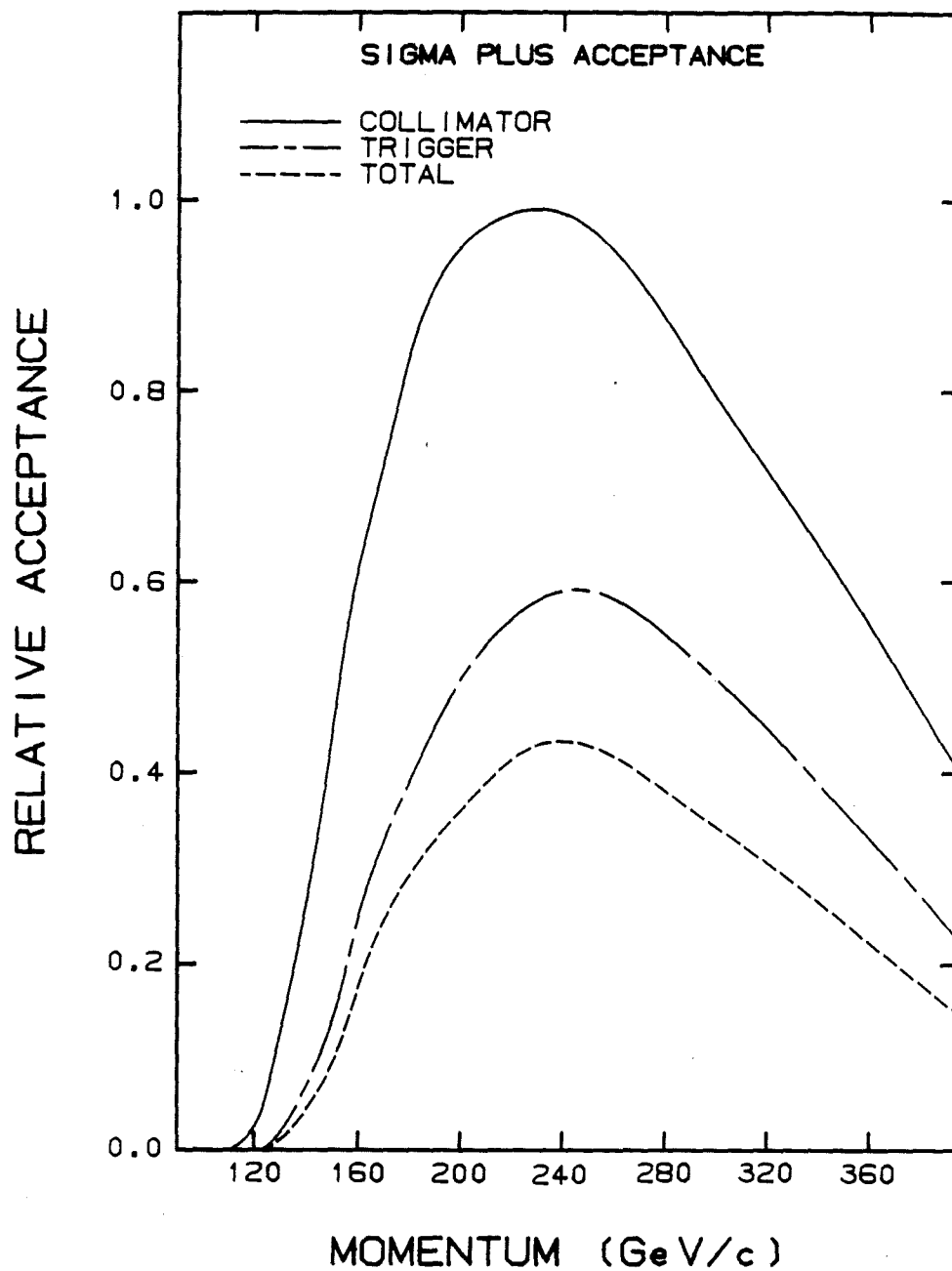


Figure 3.4 Acceptance of  $\Sigma^+ \rightarrow p\pi^0$  decays in the M2 collimator channel and the  $\Sigma^+$  trigger, and the total acceptance including collimator, trigger, and reconstruction acceptances. An abscissa value of 1 corresponds to the full geometrical solid angle of the collimator central aperture, or  $1.4 \times 10^{-6}$  sterads.



The next step involved generating a similar beam of  $\Sigma^+$  particles. The trajectory was chosen by the same method as above, but the momentum was taken from a production spectrum generated by dividing the data momentum spectrum by the total  $\Sigma^+$  acceptance. Variations in targeting were included by using measured run-to-run beam offsets at the target and collimator, and by forcing the distribution of generated  $\Sigma^+$  angles in the production plane to follow the function

$$e^{-1.55(\phi_y P_{\Sigma})^2}, \quad (3.5)$$

which is discussed in detail in Section 4.3. The angle  $\phi_y$  was measured with respect to the targeting angles of  $\pm 5$  mrad.

The decay vertex distribution followed the measured  $\Sigma^+$  lifetime  $c\tau = 2.4$  cm; particles with vertices upstream of the defining collimator, 274 cm from the source, were rejected. The remaining  $\Sigma^+$  were allowed to decay following the sequence

$$\begin{array}{l} \Sigma^+ \rightarrow p\pi^0 \\ \quad \quad \quad | \rightarrow 2\gamma, \end{array}$$

where the distribution of center of mass decay angles was chosen to be either unpolarized (isotropic in space), or polarized in a manner similar to the experimental data. The unpolarized sample was useful for checking acceptance biases in the apparatus. The trajectories of the decay products were calculated and checked against the apertures and trigger requirements. The event information was then put into the same form as the processed raw data from the tapes. The hit positions in the chambers were chosen to be the wire closest to the generated

charged track position, with ~8% registering as double wire hits. The clustering routines were by-passed and the gamma showers were directly transformed into energies and positions with detection efficiencies and resolutions matching the data as closely as possible. This short cut eliminated the check on hadron showers performed on the experimental data. At this point, the MC data was in the same form as the experimental data just before the reconstruction programs were called. Thus, except for the lack of a hadron check on the MC gamma showers, the experimental and the MC event samples could be subjected to the reconstruction and analysis programs without distinction.

The steps in the generation of the Monte Carlo  $\Sigma^+$  event sample could be summarized as:

1. Gaussianly distributed point at target and uniformly distributed point at collimator picked.
2. Momentum picked from data production spectrum and path fit through chosen points.
3. Production angle fitted to function  $e^{-1.55(\phi_y P_\Sigma)^2}$ .
4. Decay vertex chosen using  $\Sigma^+$  lifetime.
5. Polarized or isotropic  $\Sigma^+ \rightarrow p\pi^0$  decay generated.
6. All aperture and trigger requirements passed.
7. Trajectories transformed into chamber hits and PbG energies and positions.
8. Reconstruction program called and all cuts applied except hadron shower check.

### 3.6 CUTS AND BACKGROUND STUDIES

Studies of the event distributions for reconstructed  $\Sigma^+$  decays from the MC sample indicated that several cuts on the data were necessary to ensure sample purity. A comparison of the generated MC and reconstructed MC decay vertex positions indicated that ~50% of the events with reconstructed vertices located at the beginning of the decay region were from decays inside the precession magnet, M2. This occurred because the reconstruction program automatically assigned the hits in the first chamber, C1, to the  $\Sigma^+$  track, so that all reconstructed vertices were perforce downstream of C1. Since these early decaying sigmas did not pass through the entire magnetic field, their polarization vectors would not precess the full amount and their inclusion in the sample would compromise the polarization and magnetic moment analysis. A fiducial cut 4 cm downstream of chamber C1 excluded all but 4% of the MC early decays. Since the magnetic moment calculation would be changed by less than 0.2% by these remaining early decays, the effect was ignored in the data. Events with vertices after the last chamber in the decay region, C3, were also cut since the daughter track upstream of the analyzing magnet M3 could not be adequately determined.

The distributions of reconstructed  $\Sigma^+$  momenta, in Figure 3.5, showed a low momentum tail in the experimental data which was not evident in the MC sample. The MC acceptance study indicated that events below 120 GeV/c could not have been produced at the target. The most likely source of the low momentum tail was from scraping or

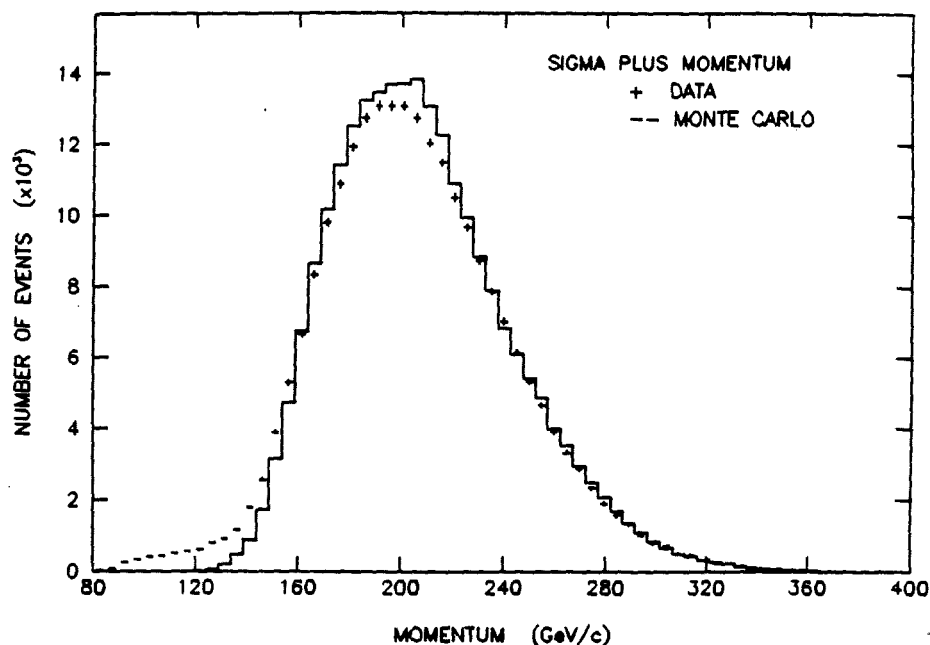


Figure 3.5  $\Sigma^+$  momentum spectrum for the Monte Carlo and data  $\Sigma^+$  candidate samples, cuts at 140 GeV/c and 350 GeV/c were applied to the data to remove events produced in the collimator channel.

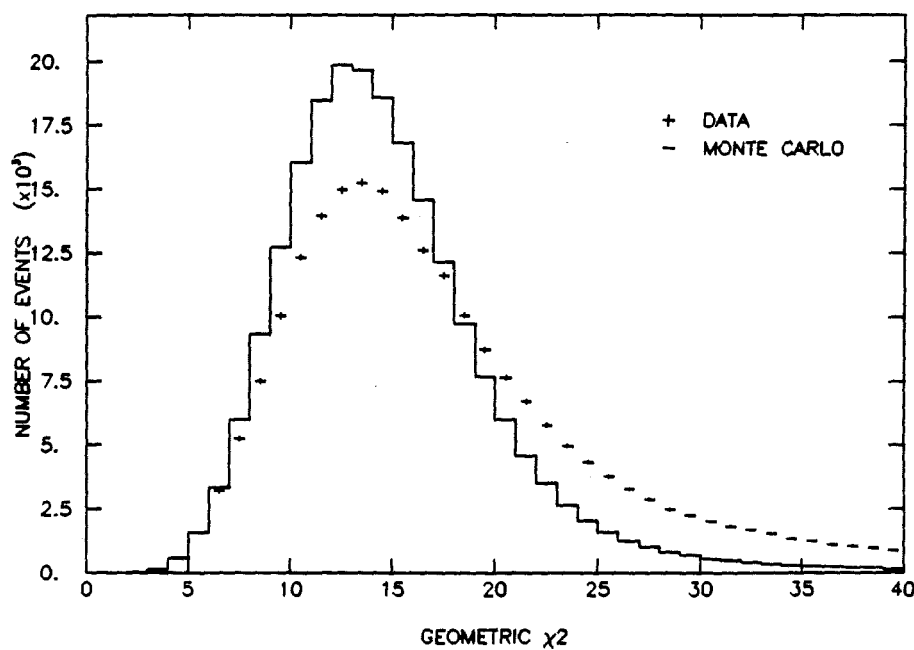


Figure 3.6 Comparison of geometric  $\chi^2$  fit to the charged track information for data and Monte Carlo  $\Sigma^+$  candidate samples. The average number of degrees of freedom in the fit was 12. A cut at  $\chi^2 = 27$  was chosen.

production of  $\Sigma^+$  at the defining collimator, halfway through the magnetic channel. A momentum cut at 140 GeV/c was introduced to eliminate these events. An upper cut at 350 GeV/c eliminated events where the statistics were too low to be useful.

Collimator produced events would also be expected to have bad geometric  $\chi^2$ , since the beam centroids at the target and collimator were included in the fit and the momentum would be calculated for traversal of the full channel length. A comparison of the MC and data geometric  $\chi^2$  distributions in Figure 3.6 does reveal a discrepancy between the two at large  $\chi^2$ . Additional contributions to the experimental tail in  $\chi^2$  may come from multiple-scattering in the material in the flight path, deviations in the magnetic fields, non-uniform inefficiencies in the detectors, or other imperfections in the apparatus, none of which were included in the Monte Carlo generation. A cut at  $\chi^2 = 27$  was chosen to eliminate poorly measured or unwanted  $\Sigma^+$  events and to reduce background contamination.

The kinematic  $\chi^2$  distributions in Figure 3.7 for the  $\Sigma^+ \rightarrow p\pi^0$ ,  $\pi^0 \rightarrow 2\gamma$  fit hypothesis to the data also show wider tails than the MC distributions. The worst mismatch occurred for the 4-C fit category, in which both gammas were detected in the PbG array. The simplified clustering routine used in the Monte Carlo to reproduce the gamma energies and positions also contributed to the mismatch. Cuts at kinematic  $\chi^2 = 9, 15$ , and 20 were applied to the 1, 3, and 4C fits, respectively, to eliminate events with poor fits to the  $\Sigma^+$  decay hypothesis.

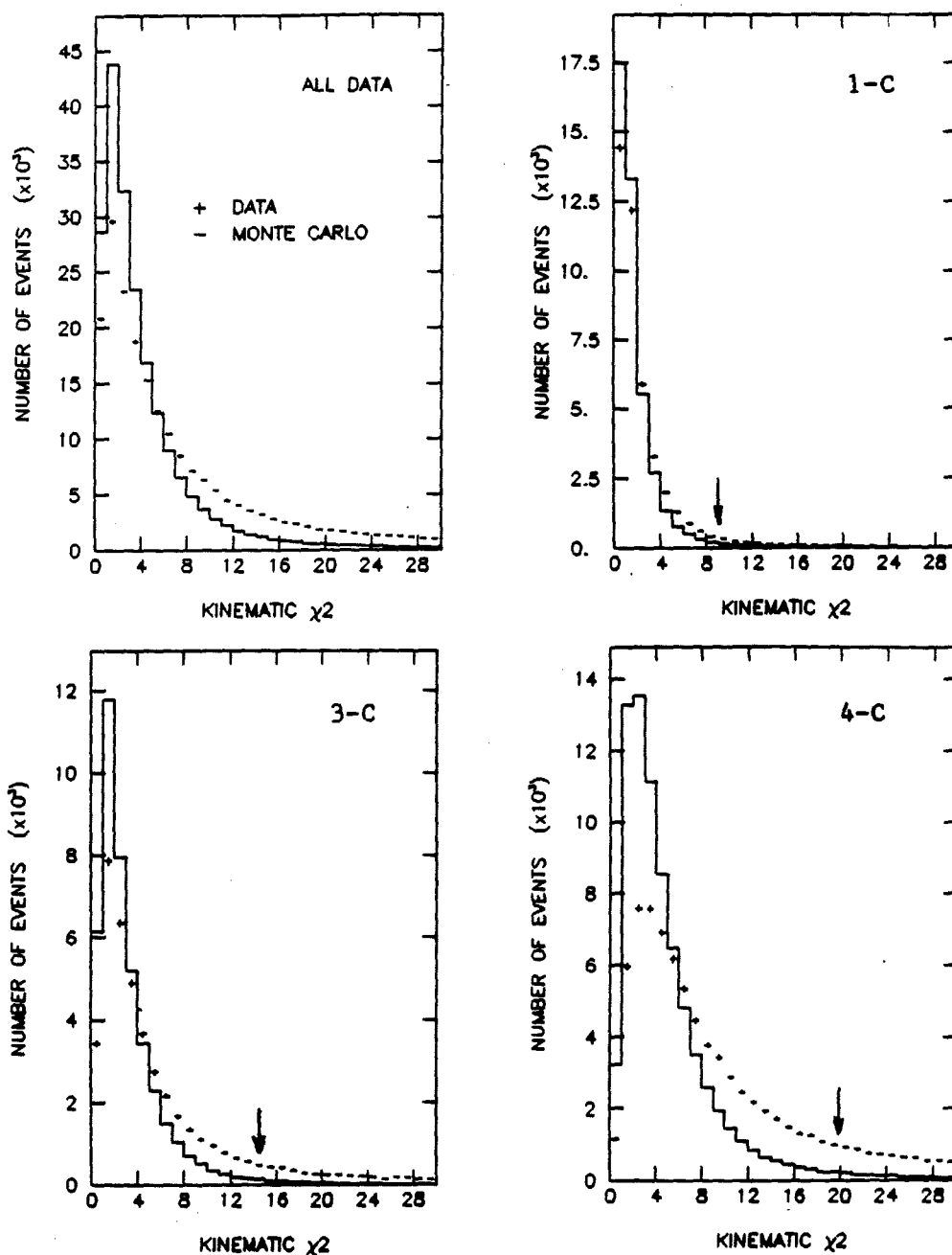


Figure 3.7 Kinematic  $\chi^2$  distributions for data and Monte Carlo  $\Sigma^+$  candidate samples, for the global fit hypothesis  $\Sigma^+ \rightarrow p\pi^0$ ,  $\pi^0 \rightarrow 2\gamma$ . Events in which the energy and position of only one gamma from the  $\pi^0$  decay was detected fell into the 1-C fit category; events with the energy of one gamma and the positions of both gammas fell into the 3-C category; and events with the energies and positions of both gammas fell into the 4-C category. C is the number of degrees of freedom for each fit. Cuts applied to the data are indicated for each fit category.

The Monte Carlo program was used to study the possibility of background events entering the sample and contributing to the measured polarization. Signals from collimator scattering and production,  $K^+ \rightarrow \pi^+ \pi^0$  decays,  $\Sigma^+ \rightarrow n \pi^+$  decays, and multiple-scattered beam tracks with PbG accidentals were considered. As already noted, the number of accepted collimator produced events was reduced by the momentum and geometric  $\chi^2$  cuts. Any such events remaining in the sample would have little contribution to the measured polarization, since they are produced at 0 mrad, with zero polarization. Beam particles whose tracks were seriously distorted by multiple-scattering in the spectrometer would be included in the sample if accidentals in the glass were reconstructed at the same time. Such occurrences should have been rare; firstly, because the amount of material in the beam path in the decay region was small, and secondly, because the reconstruction of accidental clusters in the glass was low, even though the trigger rate was high. Added to this was the expectation that the kinematic  $\chi^2$  for these events would be high.

A Monte Carlo generated sample of  $K^+ \rightarrow \pi^+ \pi^0$  decays was tested and 2% of the events passed the trigger requirements. About 0.05% reconstructed and passed all cuts, nearly all identified as good kink sigmas. The distributions for these events were flat in  $\cos\theta_x$  and  $\cos\theta_y$ , but were heavily peaked about  $\cos\theta_z = -0.5$ . With an estimated  $K^+/\Sigma^+$  ratio in the beam of 10, the  $K^+ \rightarrow \pi^+ \pi^0$  contamination in the data sample was  $\sim 0.2\%$  and had a negligible effect on the polarization measurement.

The competing  $\Sigma^+$  decay mode,  $\Sigma^+ \rightarrow n\pi^+$ , was also Monte Carlo simulated and tested. About 2% of the generated events satisfied the charged track requirements for non-kink events; none were identified as good kink sigmas. Very few of these events would have passed the hadron check on the neutron cluster; the gamma trigger requirements would be satisfied only if 2 accidentals reconstructed. The estimated background from  $\Sigma^+ \rightarrow n\pi^+$  decays was less than 0.1%. Any distortion of the polarization measurement from this small contamination was negligible, since the asymmetry parameter for this decay mode,  $\alpha = +0.068$ ,<sup>24</sup> was only 7% that of the  $\Sigma^+ \rightarrow p\pi^0$  mode.

### 3.7 FINAL EVENT SAMPLE

The original sample of 237,500  $\Sigma^+$  candidates was reduced by the cuts described in the previous section to a final sample of 137,300 events. The various cuts and the number of events removed by each were as follows:

Vertex fiducial cut ( $z < 72$ cm; $z > 1300$ cm)	51,694 events
$\Sigma^+$ momentum cut ( $p < 140$ GeV/c; $p > 350$ GeV/c)	3,604 events
Geometric $\chi^2$ cut ( $\chi_G^2 > 27$ )	24,366 events
Kinematic $\chi^2$ cuts ( $\chi_K^2 > 9, 15, 20$ for 1, 3, 4-C fit)	20,317 events

The cuts were chosen to eliminate backgrounds while preserving as much of the signal as possible. The cleanliness of the resulting sample was tested by varying the cuts and checking the stability of the analysis results. The numbers of events in the final sample for the various



event types are listed in Table 3.4.

The decay vertex distribution after cuts is compared in Figure 3.8 to the MC vertex distribution, which was generated using the  $\Sigma^+$  lifetime. The spikes in the plot indicate the reconstruction program's proclivity for finding vertices at chamber positions. The agreement between the two distributions indicates the sample purity. The laboratory opening angle between the  $\Sigma^+$  and daughter proton is given in Figure 3.9. Plotted in Figure 3.10 are the momentum spectra of the  $\Sigma^+$  and its decay products p and  $\pi^0$ .

Since the source point in the collimator and the  $\Sigma^+$  mass were included in the fits as inputs rather than parameters, there were no mass or target position cuts. Instead, the quality of the sample depended upon cuts on the kinematic and geometric fit  $\chi^2$  distributions. The peak in the distribution for each plot in Figure 3.11 matches that expected for a fit with the appropriate number of degrees of freedom. The enhancement of the experimental distribution over the MC distribution at large  $\chi^2$  shows that the Monte Carlo program did not

TABLE 3.4 The number of events in each reconstruction category for the final sample. The event categories are described in Sections 3.2 and 3.3.

	One Gamma	Two Gamma	Split Gamma	Total
Non-Kink	--	35,300	21,500	56,800
Kink	39,900	27,900	12,700	80,500
Total	39,900	63,200	34,200	137,300

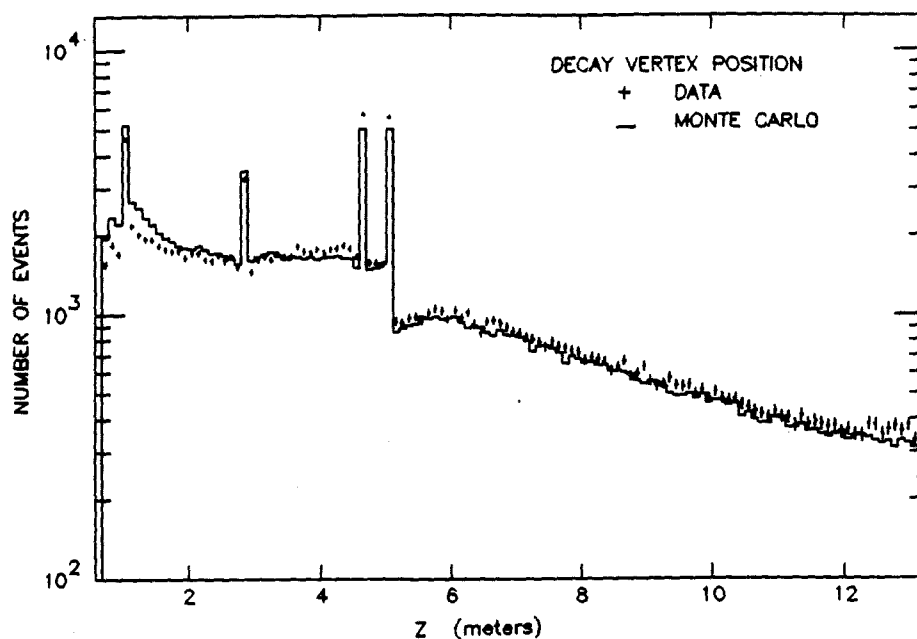


Figure 3.8 The  $\Sigma^+$  decay vertex distribution after all cuts, with  $z = 0$  at the exit face of the precession magnet. The Monte Carlo distribution is shown for comparison. The ends of the distributions were defined by fiducial cuts on the decay region.

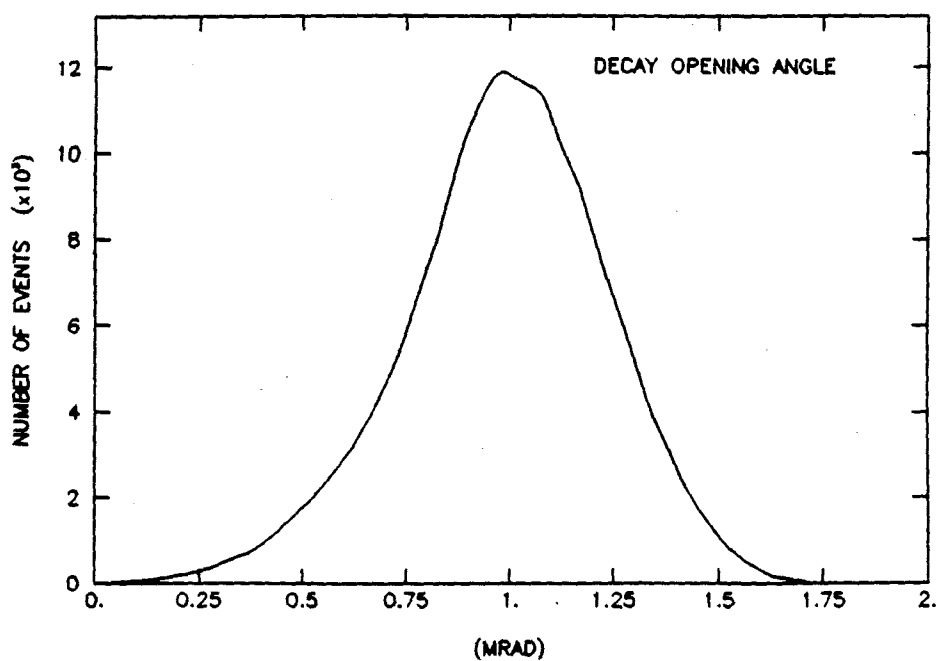


Figure 3.9 Laboratory opening angle between  $\Sigma^+$  and the daughter proton for the final sample of events in the data.

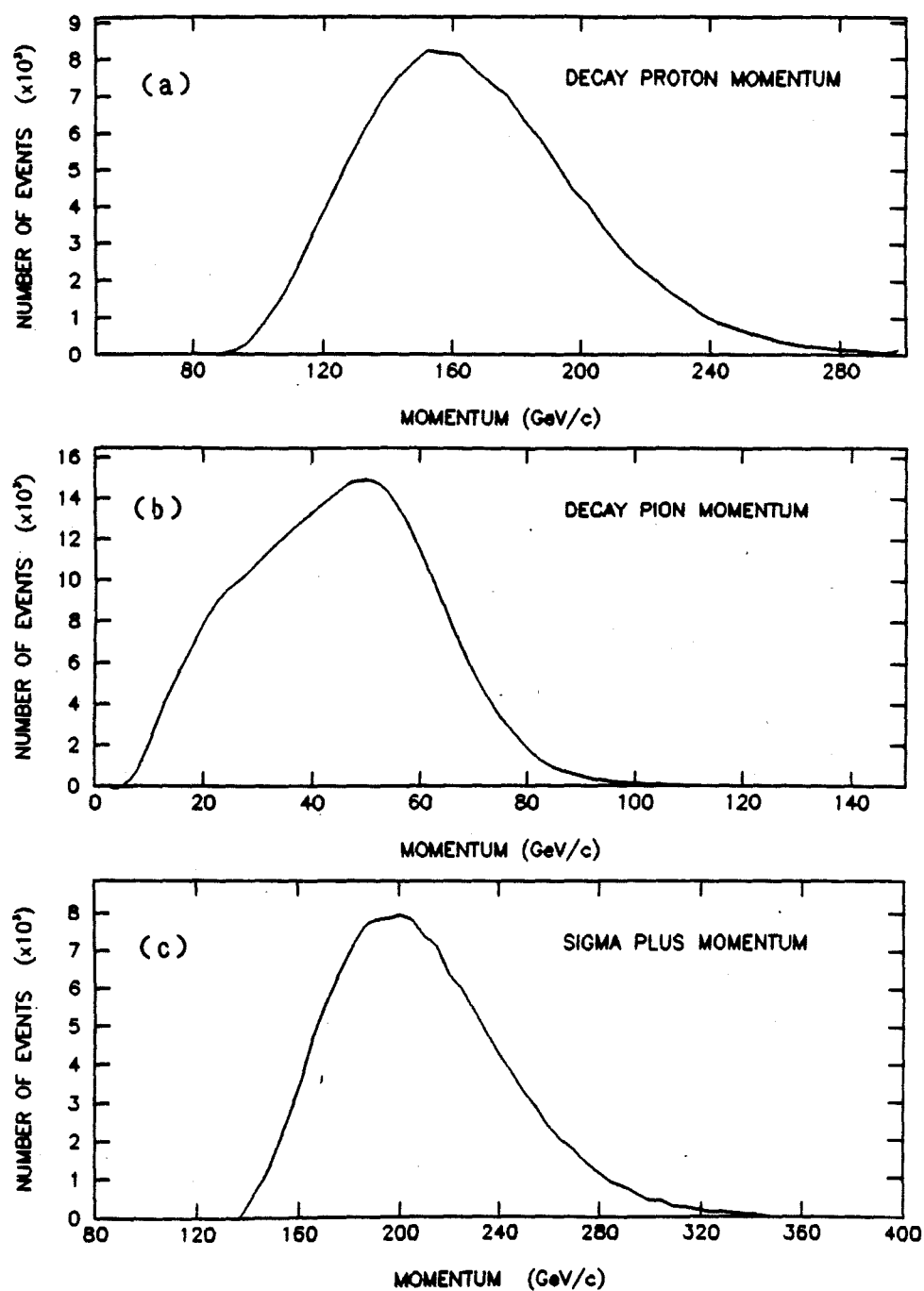


Figure 3.10 The momentum spectra after all cuts for (a)  $\Sigma^+$ , (b) daughter proton, and (c)  $\pi^0$ . The allowed ranges in the momenta were  $140 \text{ GeV}/c \leq p_{\Sigma^+} \leq 350 \text{ GeV}/c$  and  $p_p > 60 \text{ GeV}/c$ .

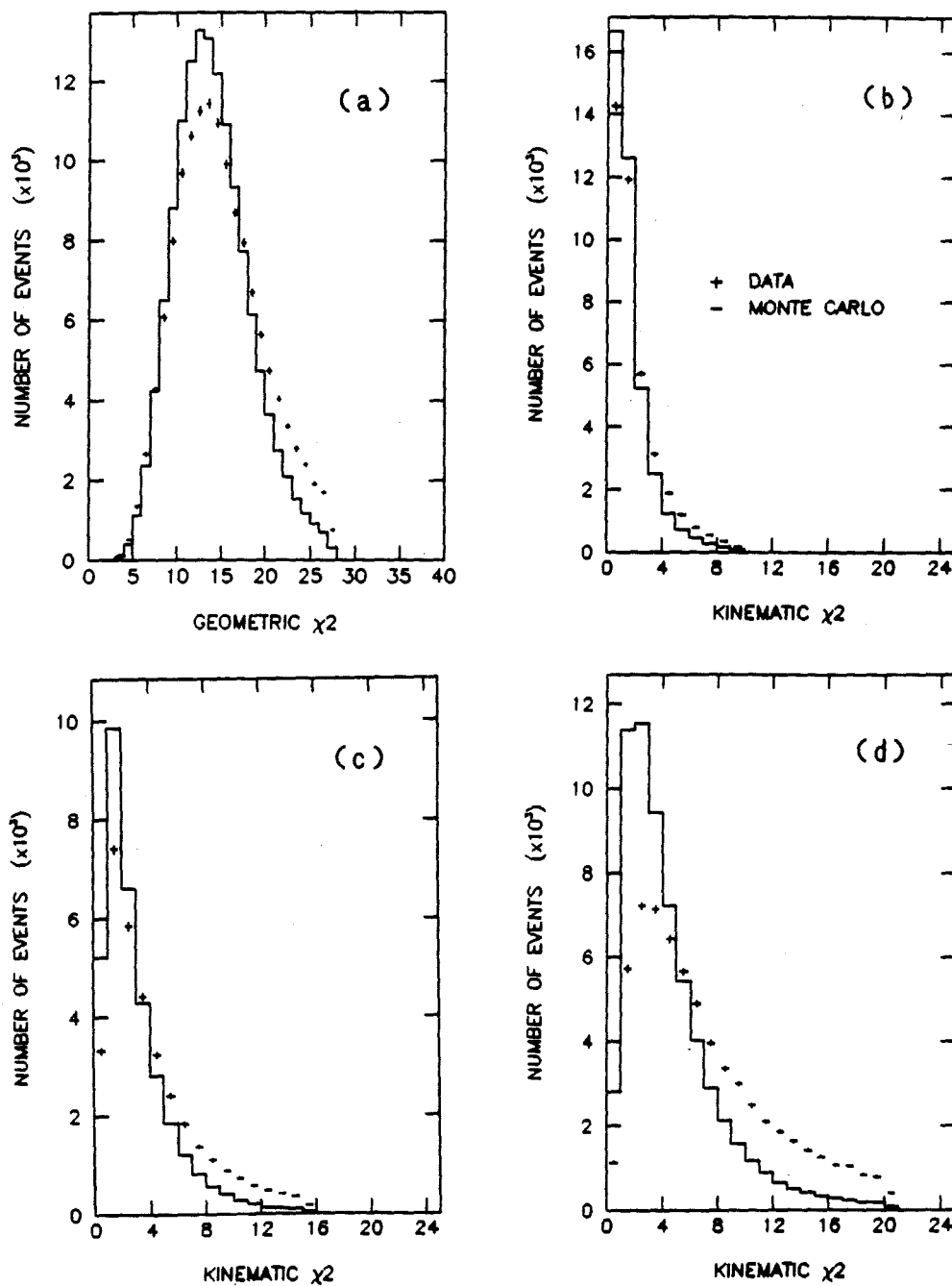


Figure 3.11 Chi-square distributions of the various reconstruction fits for the final data sample. (a) Geometric  $\chi^2$  distribution for charged track fit with an average number of degrees of freedom  $N = 12$ . Kinematic  $\chi^2$  distributions for the global fit hypothesis  $\Sigma^+ \rightarrow p\pi^0$ ,  $\pi^0 \rightarrow 2\gamma$  for (b) one detected gamma in the PbG array,  $N = 1$ ; (c) one gamma in PbG and one in the upstream detector,  $N = 3$ ; and (d) two gammas detected in the PbG array,  $N = 4$ .

include all the inefficiencies, measurement errors, and backgrounds. The match between MC and experimental data distributions, however, for the various physical apertures and parameters was very good ( $\chi^2/df \sim 2$ ), except for the  $\chi^2$  distribution tails and the  $\cos\theta$  distributions in  $x$  and  $z$ . The  $\cos\theta$  plots showed a small bias, which occurred because the MC generated Gaussian target distribution was slightly more symmetrical in  $x$  than the real distribution, and which did not affect the polarization analysis.

The purity of the final data sample, which had an estimated total background contamination of  $\sim 1\%$ , could be further demonstrated by reconstructing the  $\pi^0$  and  $\Sigma^+$  masses from measurements obtained before the application of the kinematic fits. For events with two gammas in the lead glass detector, the  $\gamma\gamma$  invariant mass plotted in Figure 3.12 was calculated using the gamma information from the glass and the vertex from the kinked track geometric fit or the average vertex from the global fit for the non-kink events. The FWHM of the distributions was  $45 \text{ MeV}/c^2$  for both the kinked track and the non-kinked track sample. A  $p\pi^0$  invariant mass could be obtained for the kink track sample from the measured values of  $\vec{p}_p$  and  $\vec{p}_\Sigma$  in the charged track geometric fit. The distribution in Figure 3.13 peaked around the  $\Sigma^+$  mass  $1.189 \text{ GeV}/c^2$  and had a FWHM of  $60 \text{ MeV}/c^2$ .

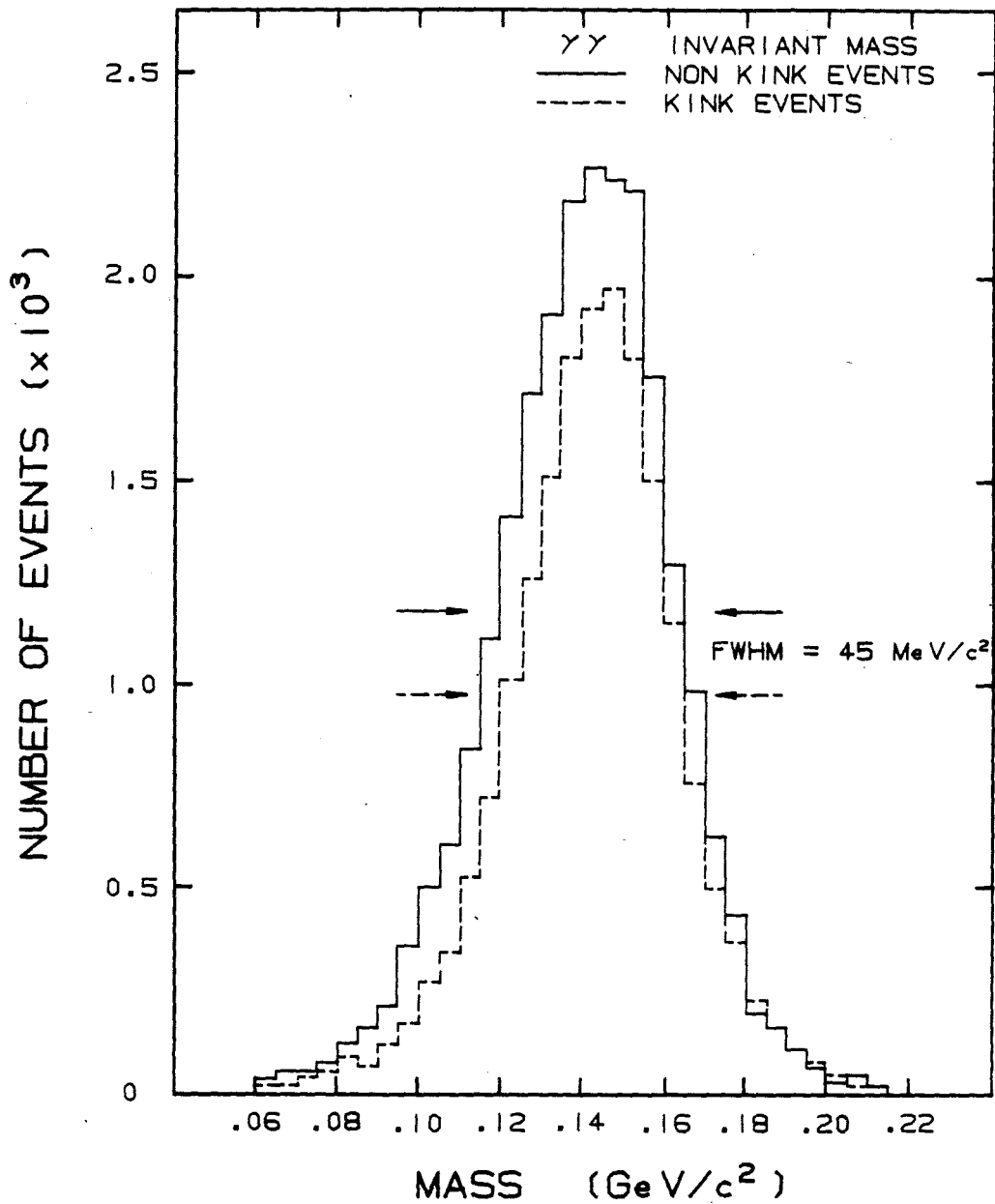


Figure 3.12 The  $\gamma\gamma$  invariant mass plot for events in the final sample with two gammas in the lead glass array. The measured gamma energies and positions and the vertex were used in the missing mass formula

$$M_{\pi^0}^2 = 2E_1E_2 (1 - \cos\theta_{12}).$$

The vertex for the kinked track sample came from the charged track fitting, while the non-kinked track vertex was assumed to be the mean value obtained by the kinematic fitting.

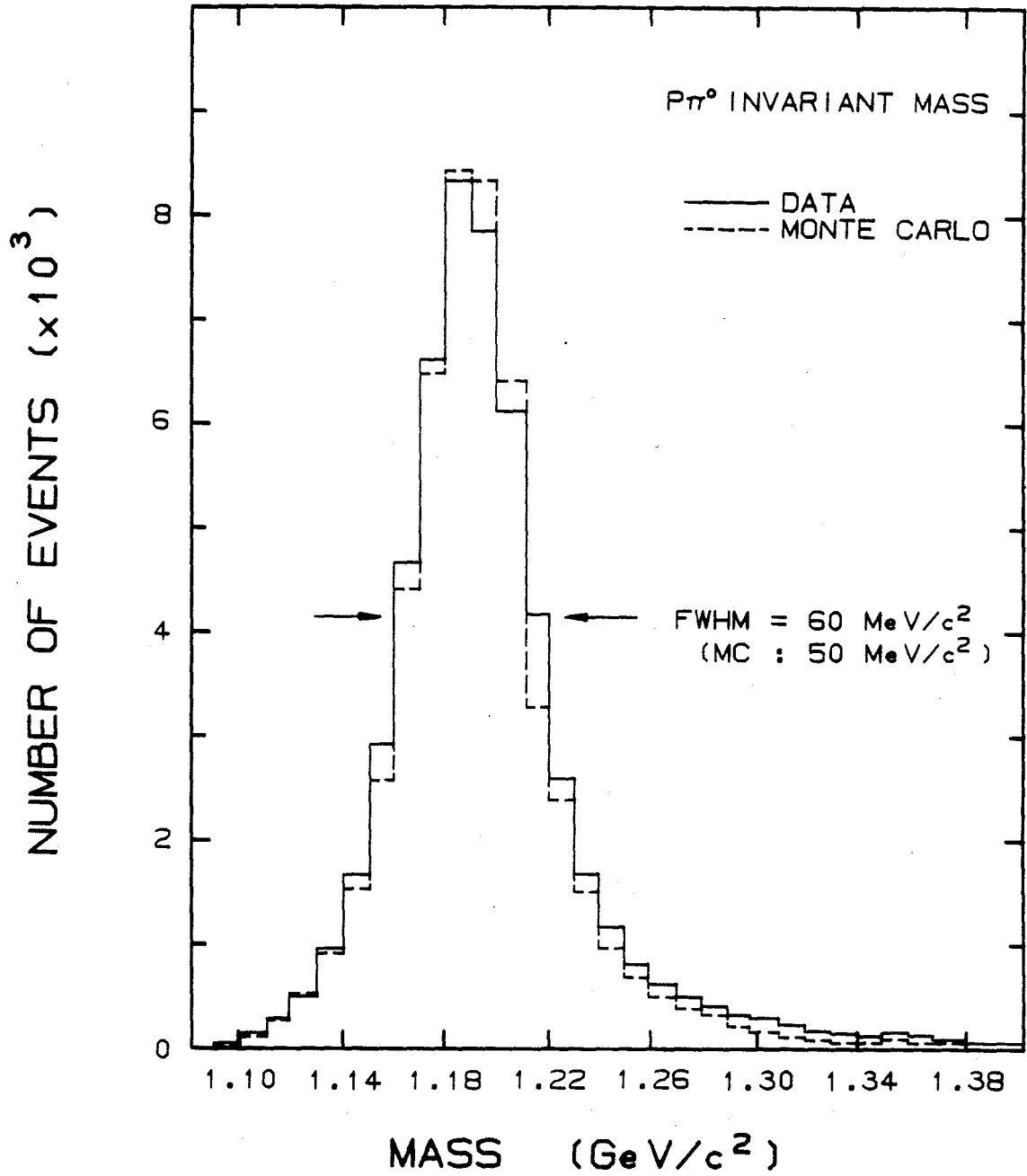


Figure 3.13 The  $p\pi^0$  invariant mass plot obtained from the measured values of  $\vec{p}_p$  and  $\vec{p}_\Sigma$  in the geometric fit and the relationship

$$M^2 = \left\{ (p_p^2 + m_p^2)^{1/2} + \left[ (\vec{p}_\Sigma + \vec{p}_p)^2 + m_\pi^2 \right]^{1/2} \right\}^2 - p_\Sigma^2.$$

## CHAPTER 4: POLARIZATION AND MAGNETIC MOMENT ANALYSIS

### 4.1 INTRODUCTION

Once the  $\Sigma^+ \rightarrow p\pi^0$  decay sample had been identified and kinematically analyzed, several known aspects of the production and decay were used to determine the  $\Sigma^+$  polarization and magnetic moment. The angular distribution of the daughter protons in the  $\Sigma^+$  rest frame had the polarization-dependent, asymmetric form typical of parity violating weak decays. Analysis of this asymmetry yielded the magnitude and direction of the polarization vector at the time of decay. Parity conservation requires that the original polarization vector at the target be perpendicular to the production plane, i.e., along  $+\hat{x}$  or  $-\hat{x}$ . The ambiguity in sign was resolved by using previous measurements of the magnetic moment to determine the original spin direction. The difference between the original and final directions determined the precession angle, which led directly to the precise measurement of the  $\Sigma^+$  magnetic moment.

### 4.2 POLARIZATION ANALYSIS

The asymmetry in the distribution of decay proton angles in the  $\Sigma^+$  rest frame has the form

$$\frac{dN}{d\Omega} = \frac{1}{4\pi} (1 + \alpha \vec{P} \cdot \hat{p}) , \quad (4.1)$$



where  $\vec{P}$  is the  $\Sigma^+$  polarization vector,  $\hat{p}$  is the direction of the daughter proton in the parent rest frame, and  $\alpha = -.979 \pm .016^{24}$  is the asymmetry parameter for the decay under study. This expression can be expanded in terms of the laboratory axes to

$$\frac{dN}{d\Omega} = \frac{1}{4\pi} [1 + \alpha(P_x \cos\theta_x + P_y \cos\theta_y + P_z \cos\theta_z)] , \quad (4.2)$$

where  $\hat{z}$  lies in the direction of the  $\Sigma^+$  momentum. If the experimental acceptance were perfect, the projection of the polarization vector on any axis could be obtained by integrating over the other two directions. The asymmetry distribution about the  $j$ -th axis is then given by

$$\frac{dN}{d(\cos\theta_j)} = \frac{1}{2} (1 + \alpha P_j \cos\theta_j), \quad j = x, y, z . \quad (4.3)$$

The three independent  $P_j$  determine the magnitude and direction of  $\vec{P}$ . In the case of imperfect acceptance, Equation 4.2 would be multiplied by an acceptance which is a function of  $\cos\theta_x$ ,  $\cos\theta_y$ , and  $\cos\theta_z$ . Equation 4.3 becomes

$$\frac{dN}{d(\cos\theta_j)} = \left(\frac{1}{2}\right) A(\cos\theta_j) [1 + \alpha P_j \cos\theta_j + K_j] , \quad (4.4)$$

where  $A(\cos\theta_j)$  is the acceptance after integration and the constant term  $K_j$  is added since the integration over the other two angles is no longer equal to zero. If the acceptance distributions are symmetrical in  $\cos\theta$ ,  $K$  vanishes.

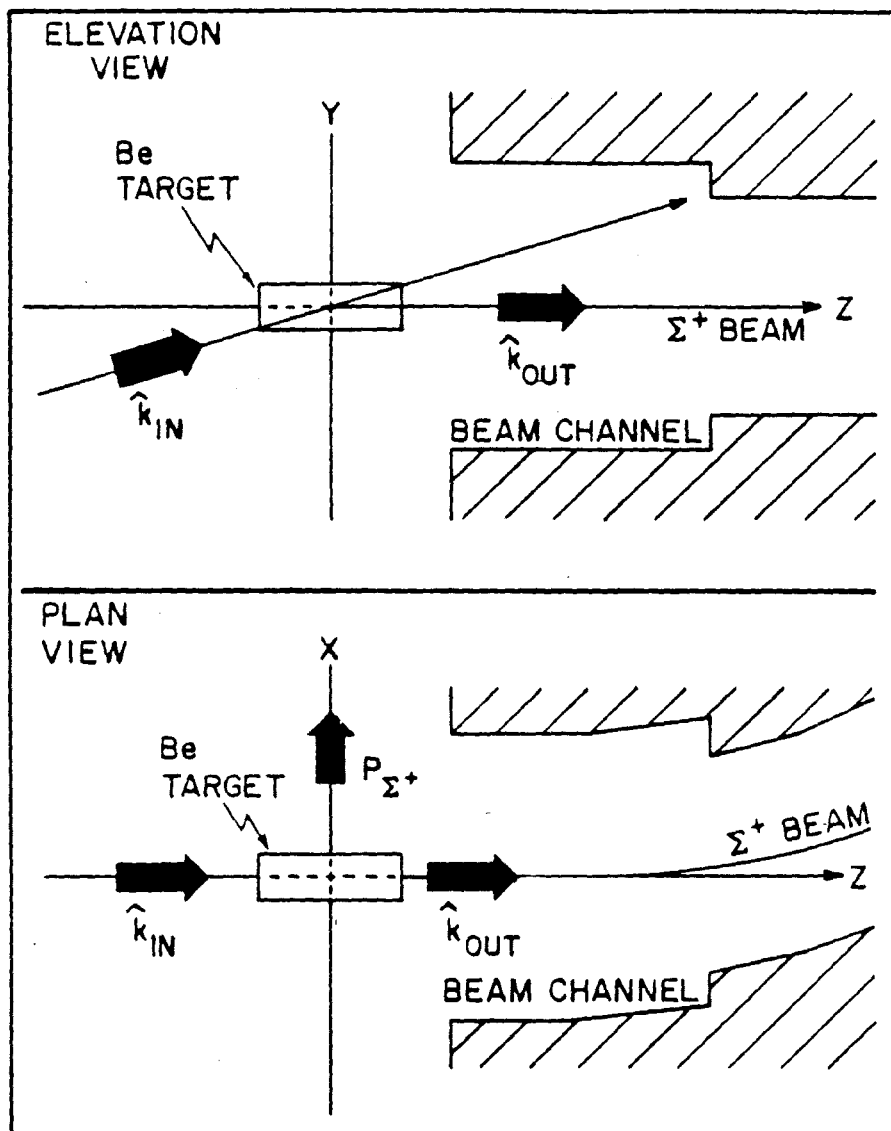


Figure 4.1 Initial direction of the polarization vector at production. The vector was required to be perpendicular to the plane defined by the incoming proton momentum  $\vec{k}_{in}$  and the outgoing  $\Sigma^+$  momentum  $\vec{k}_{out}$ . Its sign was unknown until determined by experiment.

In actual practice, the data were divided into 20  $\cos\theta$  bins of width  $\Delta = 0.1$  for each view, so the event distribution  $R$  in the  $i$ -th bin for the  $x$ -th view was expressed as

$$R^{\pm}(\cos\theta_1) = \left(\frac{\Delta}{2}\right) A_x^{\pm}(\cos\theta_1) [1 \pm \alpha P_x \cos\theta_1 \pm K_x] , \quad (4.5)$$

with similar equations for  $y$  and  $z$ . The  $\pm$  signs refer to  $\pm 5$  mrad production angle; changing the production angle reversed the sign of the polarization.  $A_x(\cos\theta_1)$ , the acceptance of the apparatus, was dependent on the  $\Sigma^+$  momentum, the  $\cos\theta$  bin, and the production angle, and was normalized so that the total acceptance over the range  $-1 < \cos\theta < 1$  was equal to 1. Contributions from acceptances could be minimized or eliminated by taking the ratio of the difference over the sum of the negative and positive production angle data;

$$\frac{R_x^+(\cos\theta_1) - R_x^-(\cos\theta_1)}{R_x^+(\cos\theta_1) + R_x^-(\cos\theta_1)} = \alpha P_x \cos\theta_1 + K_x , \quad (4.6)$$

where  $A^+ = A^-$  has been assumed.

Plots of the ratio in Equation 4.6 versus  $\cos\theta_1$  for each view in  $x$ ,  $y$ , and  $z$  are shown in Figure 4.2. The 20 data points per plot were fitted to a line whose slope was  $\alpha P_j$ , where  $j = x, y$ , or  $z$ . The intercept  $K$ , which had no effect on the analysis, was compatible with zero. Indicated on the plots are the fitted values for  $\alpha P_j$  with the errors and  $\chi^2$  of the line fits. Although the plots shown are representative and useful for illustrative purposes, they were not used

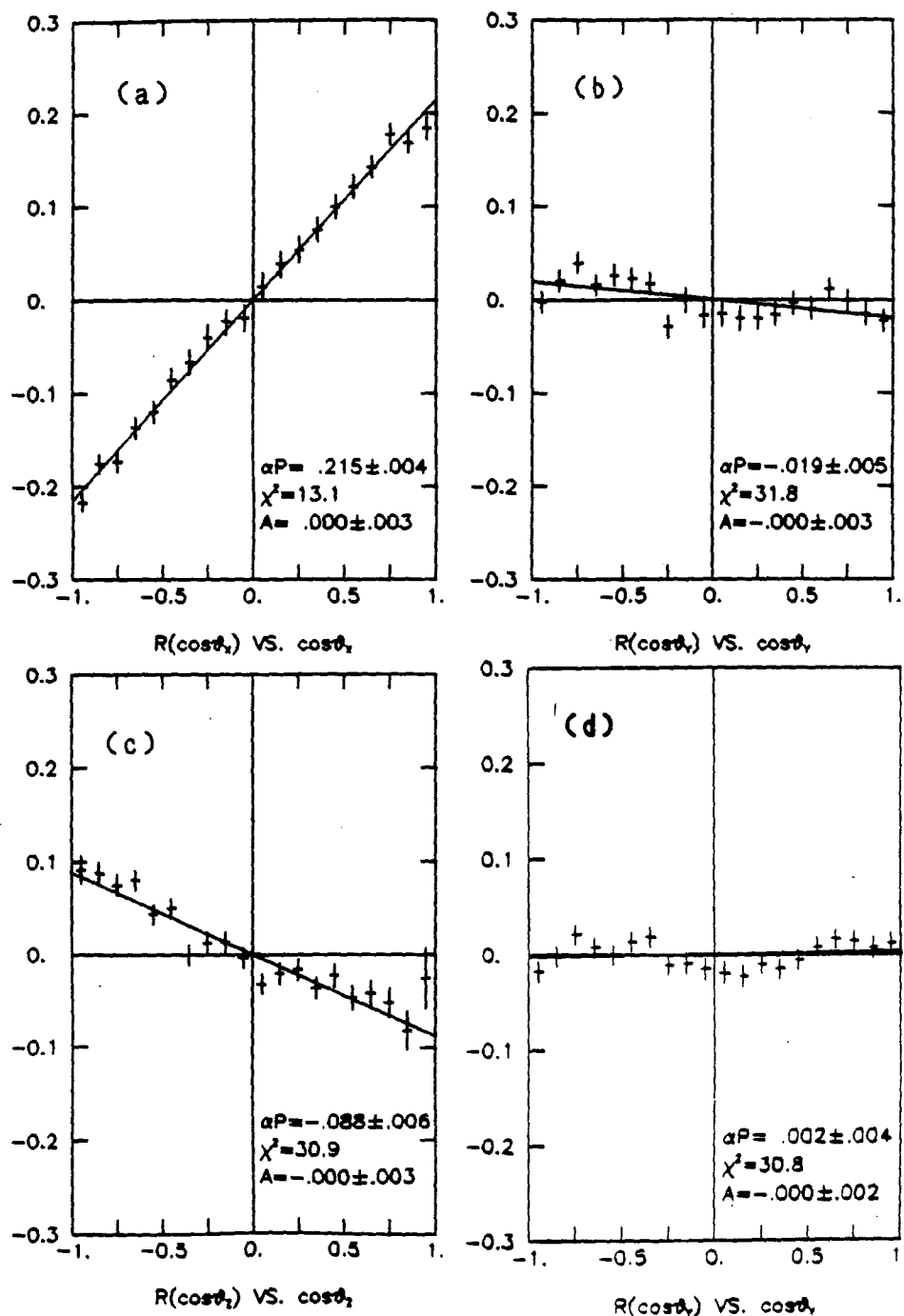


Figure 4.2 (a-c)  $R_i(\cos\theta)$  plotted versus  $\cos\theta$  for the total sample summed  $i$  over momentum, showing the slope  $\alpha P_i$ , the intercept  $A$ , and the  $\chi^2$  for the line fit for components  $i = x, y, z$ . (d) Repeat of plot (b) for the y component after a cut has been performed to eliminate a spurious y-signal from targeting effects.

in the determination of the results because of the wide momentum spread in the sample and the heavy dependence of the polarization and acceptance on momentum. Similar plots and fits were made for each of nine, 20 GeV/c-wide momentum bins, and the results are tabulated in Table 4.1, in Section 4.4.

### 4.3 ACCEPTANCE STUDIES

#### 4.3.1 DEPENDENCE ON PHYSICAL PARAMETERS

The dependence of the acceptance on the component  $x, y, z$ , on the  $\cos\theta$  bin, and the momentum is exhibited in the plots in Figure 4.3. The acceptance in the plots is defined to be the sum of the positive and negative production angle event distributions, each separately normalized to give a total acceptance of one over the entire  $\cos\theta$  range. The acceptance in  $x$  was depleted for  $\cos\theta_x = 0$  decays, indicating a detection inefficiency for small angle decays. The  $z$  plot shows this same inefficiency, with forward angle decays more heavily depleted than backward decays due to gamma detection inefficiencies. The  $y$  view also shows a depletion at  $\cos\theta = 0$  due to the limiting size of the proton counter PC. The dependence on momentum shows that the acceptance shifted from mostly backward events at low momentum to a more nearly flat distribution at higher momentum. Clipping at  $\cos\theta_x = 1$  by the high momentum edge of the proton counter increased with momentum as the bend angle in the spectrometer magnet decreased.

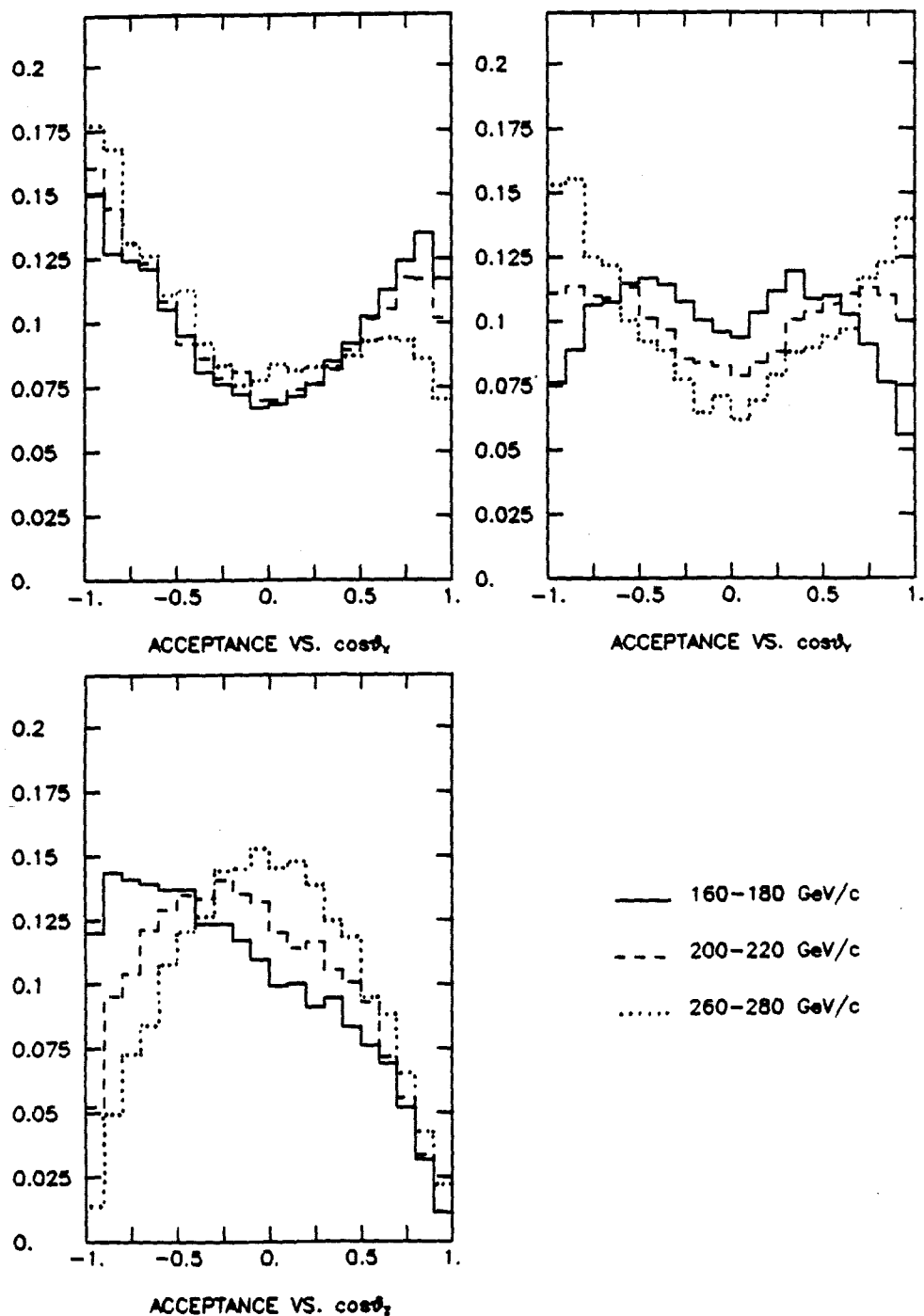


Figure 4.3 Acceptance plots for  $\cos\theta_i$ ,  $i = x, y, z$ , for 3 representative momentum bins. The summed acceptances were normalized to 2 over  $\cos\theta$ .

The majority of the effects that these acceptance dependences would have on the results were cancelled by the analysis technique, which separated the data into bins according to momentum, x, y, or z view, and  $\cos\theta$ . The fact that the average  $\chi^2$  for the line fits in Figure 4.2 was 19.4 for 18 degrees of freedom and the fact that the results were stable to various cuts on the sample indicates that possible effects were negligible.

#### 4.3.2 EFFECT OF TARGETING ANGLES

The method of analysis outlined in Section 4.2 was valid only if the positive and negative targeting angle acceptances  $A^+$ ,  $A^-$  were equal. A test of this equality could be made by studying the polarization signal in y. The direction of the spin vector at the production target was known to be

$$\hat{\pm x} = \frac{\hat{k}_{in} \times \hat{k}_{out}}{|\hat{k}_{in} \times \hat{k}_{out}|}, \quad (4.7)$$

with the sense, or sign, unknown. (See Figure 4.1.) The magnetic field was along  $-\hat{y}$  and the  $\Sigma^+$  momentum vector  $\hat{k}_{out}$  defined  $+\hat{z}$ , so the spin vector should have precessed only in the xz plane and there should have been no y component. The observed signal,  $\alpha P_y = 0.018 \pm 0.005$ , indicates that  $A_y^+ \neq A_y^-$ . The source of this signal is shown in Figure 4.4, which plots the distribution of production angles  $\theta_y$  for  $\pm 5$  mrad targeting angles. The difference in production angle spectra caused a separation of  $\Delta y \approx 3$  mm in daughter proton beam centroids at

the limiting aperture, proton counter PC, 45 m downstream of the target. The Monte Carlo reproduced this effect when run-to-run variations in targeting positions were included and the distribution of production angles about the incident beam directions  $\pm 5$  mrad,  $\phi_y = \theta_y \pm 5$  mrad, was constrained to fit the expected distribution

$$e^{-B\phi_y^2 P_\Sigma^2} \quad (4.8)$$

$P_\Sigma$  was the  $\Sigma^+$  momentum and B was chosen to be 1.55. Removing these targeting effects from the Monte Carlo simulation returned the y signal to zero, but changed the  $\alpha P_x$  and  $\alpha P_z$  signals in each momentum bin by less than 1 standard deviation.

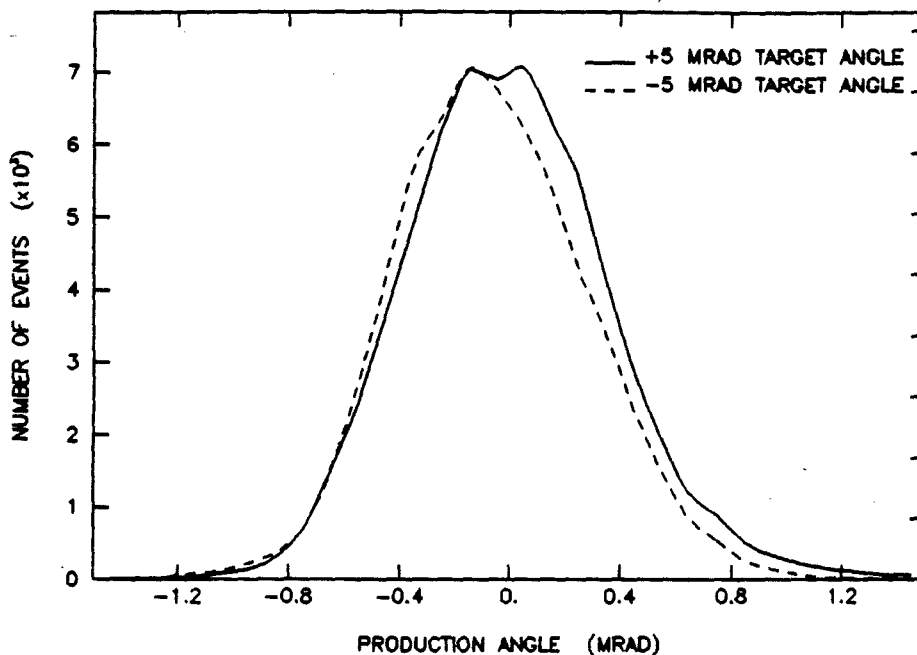


Figure 4.4 The measured  $\Sigma^+$  production angle  $\theta_y$ , produced by protons incident on the target at angles of  $\pm 5$  mrad, respectively.



The signal in the data sample was removed by placing a symmetric cut in  $y$  about the beam centroids in PC, which varied from run-to-run. The resulting plot for  $\alpha P_y$  is shown in Figure 4.2d. The  $y$  polarization was reduced to  $0.002 \pm .004$  and the  $x$  and  $z$  signals were again affected by less than 1 std. dev. Because of the lack of effect on  $x$  and  $z$  and the lack of statistics to obtain run-to-run beam centroids for each momentum bin, this cut was not used to obtain the results quoted in Table 4.1. Although the spurious  $y$ -signals are given, the true values were compatible with zero.

Conclusions drawn from these tests indicated that the acceptances for  $\pm 5$  mrad data taking were different because the daughter proton beams were aimed differently at the limiting aperture PC. The differences, however, were shown to have no effect on the  $x$  and  $z$  signals, and the spurious  $y$  polarization they produced could be reproduced and controlled in the Monte Carlo or removed by appropriate cuts on the data.

#### 4.3.3 EFFECT OF GAMMA DETECTION

The asymmetric placement of the hole in the lead glass array caused a difference in the yields for positive and negative targeting angles. Because of the large polarization asymmetry, the  $\pi^0$ 's from  $\Sigma^+$ 's produced by positive angle targeting were directed toward the hole and the  $-x$  direction, and those produced by negative angle targeting were directed away from the hole. MC studies of the different gamma-detection event types showed that the yields for positive

targeting were lower by  $\sim 2\%$  for the  $1\gamma$  sample and by  $\sim 10\%$  for the samples with two detected  $\gamma$ 's. The losses in the  $1\gamma$  sample were probably made up by events which shifted from the  $2\gamma$  sample. The difference in the yields for the total sample was  $\sim 5\%$ . This strong x-direction asymmetry caused a difference in the acceptance  $A_z^+$  and  $A_z^-$ , which had the effect of reducing  $P_z$  and, therefore,  $\mu_{\Sigma^+}$ . In addition to this x-asymmetry effect, the position of the  $\Sigma^+$  beam in x also shifted an average 3 mm at the lead glass between positive and negative targeting, further contributing to the acceptance difference. The change in the precession angle was opposite that of the asymmetry effect and served to increase the magnetic moment measurement. This change was energy dependent and primarily affected the  $1\gamma$  sample, with its higher gamma energies. See Figure 4.5.

The effect of the acceptance difference was studied in both the MC and experimental data. The magnetic moment for the experimental  $1\gamma$ -sample differed from the 2-detected- $\gamma$ 's samples by 4 std. dev., as shown in Figure 4.11. The MC reproduced this split in the results. Of primary importance, however, was the fact that the MC, using an input polarization and precession angle equal to the measured value for the total experimental sample, reproduced the experimental magnetic moment for the total sample within one standard deviation. When the experimental  $1\gamma$ - and  $2\gamma$ -samples were corrected by the shifts from the input value for the MC, they too agreed with the experimental magnetic moment for the total sample, with similar errors. This indicates that any systematic error in the measured result due to this differing gamma acceptance was of the order of one standard deviation.

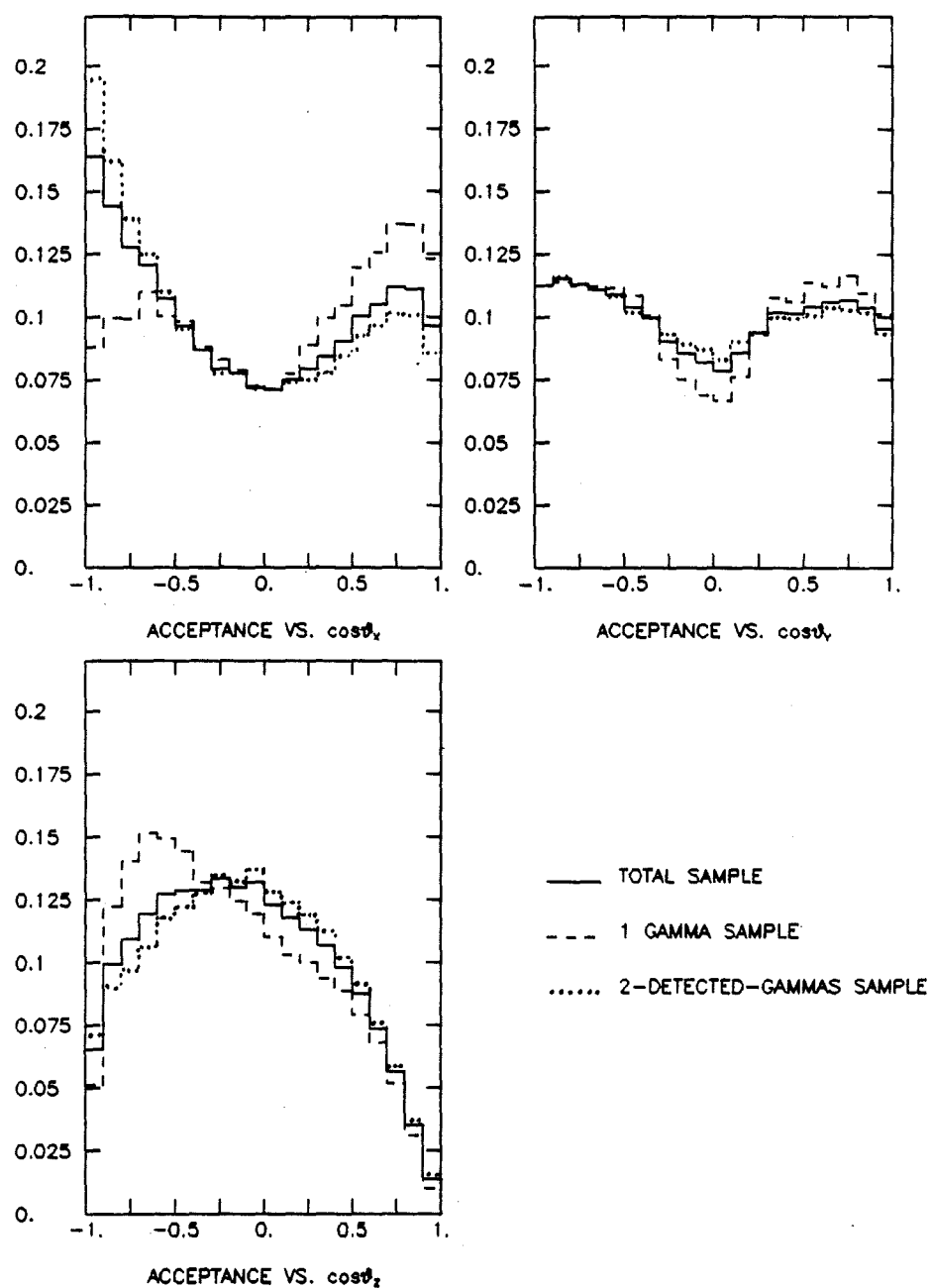


Figure 4.5 Acceptance plots for  $\cos\theta_i$ ,  $i = x, y, z$ , for the total sample and for the 1-gamma and 2-detected-gammas subsamples. The summed acceptance for each sample was normalized to 2 over  $\cos\theta$ .

#### 4.4 POLARIZATION RESULTS

The polarization vector  $\vec{P}$  was obtained from the individual components,

$$\begin{aligned}\vec{P} &= P_x \hat{x} + P_z \hat{z} \\ |\vec{P}| &= (P_x^2 + P_z^2)^{1/2},\end{aligned}\tag{4.9}$$

where  $P_y$  was not included because it was shown to be compatible with zero. The direction of this vector, however, must be corrected for the precession in the magnet M2 to obtain the direction of the spin at production. Combining Equations 1.13 for the amount of precession and Equation 1.14 for the magnetic moment the relationship between magnetic moment and precession angle gives

$$\mu_\Sigma = \frac{(\phi - \theta)_{\text{LAB}}}{(1/\beta)(18.307^\circ/\text{T-m}) \int B dl} + \frac{m_P}{m_\Sigma},\tag{4.10}$$

in nuclear magnetons. Using the previous world average  $\mu_{\Sigma^+} = 2.33 \pm 0.13 \text{ n.m.}$ ,<sup>24</sup> the field integral  $6.55 \pm .01 \text{ T-m}$ , and the known masses, the angle  $(\phi - \theta)_{\text{LAB}}$  between  $\vec{P}$  and the  $\Sigma^+$  momentum should have changed by  $+186^\circ \pm 16^\circ$ . Rotating the measured vector, which lies in the second quadrant with  $P_x$  negative and  $P_z$  positive, by  $-186^\circ$  brought the polarization vector to the  $+x$  axis, within error. See Figure 4.6.

The polarization  $P_0$  as a function of momentum is plotted over the range 140 GeV/c to 350 GeV/c in Figure 4.7, and listed in Table 4.1. For  $p_T = (140-350 \text{ GeV/c}) \times 5 \text{ mrad}$ , the range was  $0.7 < p_T < 1.75 \text{ GeV/c}$ ;

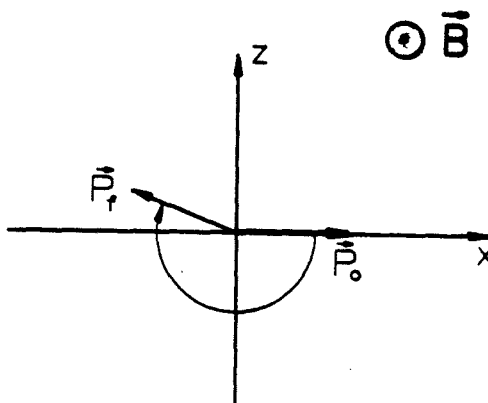


Figure 4.6 Precession of the polarization vector in magnet M2.

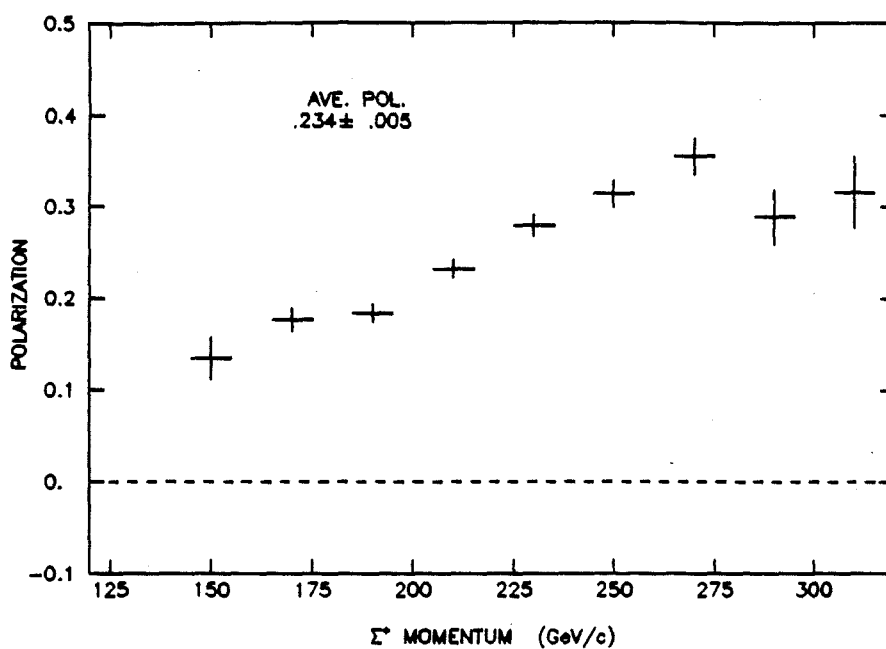


Figure 4.7 Polarization plotted as a function of momentum for the total data sample. Values are listed in Table 4.1.

and for Feynman  $x_F = p_T/(2 \text{ GeV}/c)$ , the range was  $0.35 < x_F < 0.88$ . The average polarization over the sample range was

$$P_{\text{ave}} = + 0.234 \pm 0.005 .$$

The sign of the polarization was positive, which is opposite that for inclusively produced  $\Lambda$ 's.\*

#### 4.5 PRECESSION ANGLE MEASUREMENT

Once the directions of the polarization vector at production and after precession have been established, the precession angle can be precisely measured by determining

$$(\phi - \theta)_{\text{LAB}} = \tan^{-1}(P_z/P_x) + n\pi , \quad (4.11)$$

where  $n$  for this experiment must be 1 to bring the final vector into the proper quadrant. The angle  $\alpha = P_x/P_z$  was determined by using a minimized chi-square fit with eight degrees of freedom. The data were divided into nine momentum bins to avoid biases due to momentum dependence, and the eighteen measured values of  $P_x$  and  $P_z$  listed in

---

\*Note: These results corroborate a preliminary report<sup>30</sup> on polarization previously published for these data, which used 10% of the data and a simplified analysis to obtain a result  $P = +0.22$  over the momentum range 140 to 280 GeV/c. Values of the average polarization components,  $\alpha P_x = 0.021 \pm 0.011$ ,  $\alpha P_y = -0.035 \pm 0.011$ , and  $\alpha P_z = -0.011 \pm 0.011$ , with an estimated systematic error of 0.035, were also reported. While the sign and magnitude of the polarization were not found to be particularly sensitive to cuts, acceptances, and analysis techniques, the individual components, particularly  $\alpha P_z$ , required the more advanced techniques outlined here for precise measurement.

Table 4.1 were used as inputs to the fit. The lengths of the nine polarization vectors and the precession angle were the outputs. The lengths of the vectors calculated directly from the input components are listed in Table 4.1, and were found to differ by less than 0.3 std. dev. from the fitted lengths.

The fit gave a value for the precession angle of

$$(\phi - \theta)_{\text{LAB}} = 201.54^\circ \pm 1.34^\circ ,$$

with a  $\chi^2$  per degree of freedom of 1.2. The quoted error was statistical.

#### 4.6 MAGNETIC MOMENT CALCULATION

The value of the precession angle was substituted into Equation 4.10 to yield a measurement of the  $\Sigma^+$  magnetic moment of

$$\mu_{\Sigma^+} = 2.469 \pm 0.011 \text{ nuclear magnetons,}$$

where the statistical error in the precession angle measurement has been combined in quadrature with an estimated 0.2% measurement error in the magnetic field integral. The values of the magnetic moment calculated for the individual momentum bins in Table 4.1 are plotted in Figure 4.9 as a function of momentum. A fit of these points to the value above gave a  $\chi^2$  of 13.5 for 8 degrees of freedom, indicating that any dependence on momentum is minimal.

TABLE 4.1 Results for the polarization, precession angle, and magnetic moment for nine momentum bins. The non-zero values for the y-component of polarization were due to targeting angle differences and can be shown to be compatible with the expected value of zero when these differences are taken into account. The asymmetry parameter  $\alpha_{\Sigma} = -.979 \pm .016$ .

$\Sigma$ momentum (GeV/c)	$\alpha P_x$	$\alpha P_y$	$\alpha P_z$	$ P $	$(\phi-\theta)_{LAB}^0$	$\mu_{\Sigma}$ (n.m.)
140-160	0.131 $\pm$ .021	0.042 $\pm$ .025	0.001 $\pm$ .022	0.133 $\pm$ .023	179.40 $\pm$ 9.68	2.28 $\pm$ .081
160-180	0.160 $\pm$ .011	0.011 $\pm$ .013	-0.064 $\pm$ .013	0.176 $\pm$ .012	201.78 $\pm$ 4.21	2.47 $\pm$ .035
180-200	0.171 $\pm$ .091	-0.013 $\pm$ .010	-0.052 $\pm$ .011	0.183 $\pm$ .010	196.88 $\pm$ 3.50	2.43 $\pm$ .029
200-220	0.216 $\pm$ .009	-0.014 $\pm$ .010	-0.069 $\pm$ .012	0.232 $\pm$ .010	197.64 $\pm$ 2.89	2.44 $\pm$ .024
220-240	0.253 $\pm$ .011	-0.032 $\pm$ .011	-0.103 $\pm$ .014	0.279 $\pm$ .012	202.19 $\pm$ 2.85	2.47 $\pm$ .023
240-260	0.279 $\pm$ .013	-0.039 $\pm$ .013	-0.129 $\pm$ .018	0.316 $\pm$ .015	204.75 $\pm$ 3.24	2.50 $\pm$ .027
260-280	0.309 $\pm$ .018	-0.052 $\pm$ .018	-0.150 $\pm$ .025	0.354 $\pm$ .020	206.91 $\pm$ 3.94	2.51 $\pm$ .033
280-300	0.237 $\pm$ .028	-0.043 $\pm$ .026	-0.153 $\pm$ .036	0.288 $\pm$ .030	212.78 $\pm$ 6.89	2.56 $\pm$ .058
300-350	0.273 $\pm$ .037	-0.071 $\pm$ .035	-0.143 $\pm$ .047	0.315 $\pm$ .039	207.55 $\pm$ 8.29	2.52 $\pm$ .069



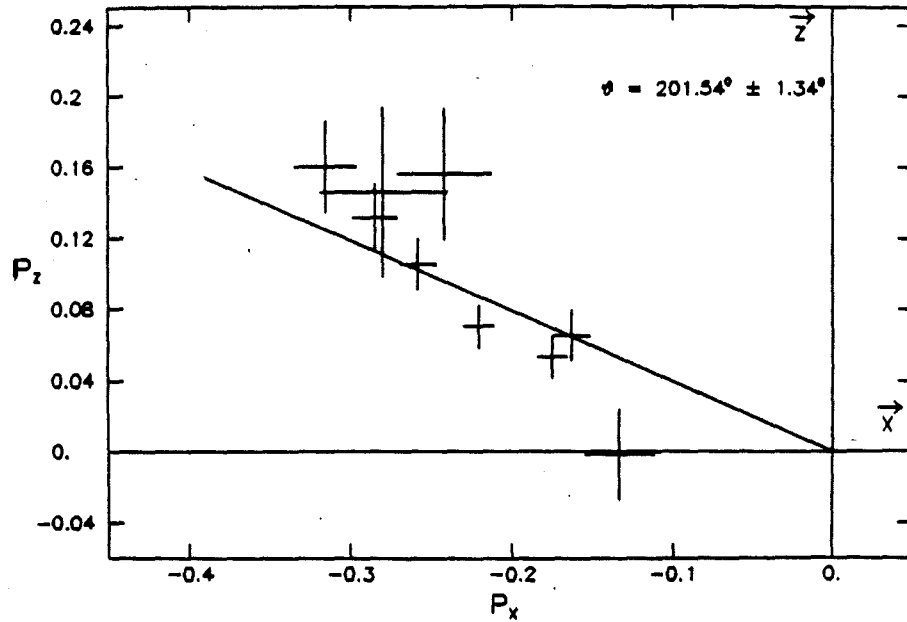


Figure 4.8 Plot of  $P_z$  versus  $P_x$  for nine momentum bins listed in Table 4.1.<sup>2</sup> The slope of the line fit was used to determine the precession of the polarization vector in magnet M2.

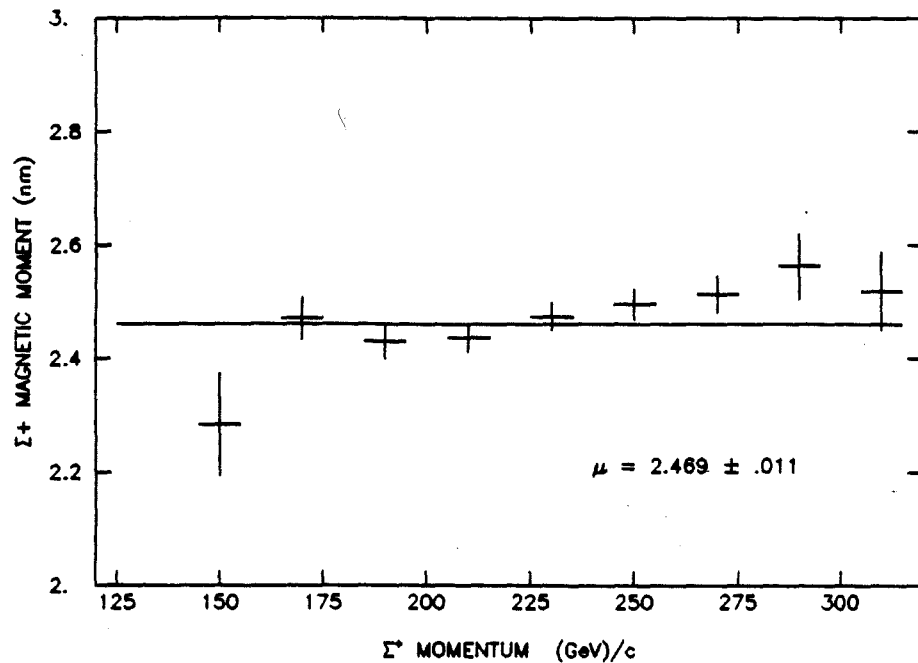


Figure 4.9 The magnetic moment plotted as a function of momentum, taken from Table 4.1. The value of the magnetic moment calculated from the fitted precession angle is also shown. The individual data points fit the calculated value with  $\chi^2 = 13$  for 8 degrees of freedom.

#### 4.7 SYSTEMATIC ERRORS

Several tests were made on the data and the analysis program to search for systematic errors. Because of the large polarization signal and the high statistical accuracy in this experiment, systematic errors could be significant compared to the statistical errors.

The reconstruction and analysis programs were first tested for their ability to determine the known polarization of a data sample. The  $\Sigma^+$  data were originally written to tape in alternating pairs: two tapes at +5 mrad production angle followed by two tapes at -5 mrad. Mixing the data by assigning first one event on each tape to one sample and the next on the tape to another created two equal samples, each with zero polarization from the mixing. Treating the two samples as if they came from opposite production angles and running the analysis program resulted in a polarization measurement equal to zero within two standard deviations, for all components. A similar sample of mixed, polarized MC events were also tested. See Table 4.2. The return of the known zero polarization indicates that the reconstruction and analysis programs did not produce spurious polarization signals.

The data were then checked for stability against varying cuts and parameters. The largest effect on the measurements occurred when the decay fiducial volume cut was applied to the initial  $\Sigma^+$  candidate sample. The average polarization after cutting increased by 2 std. dev. and the magnetic moment by  $\sim 1.5$  std. dev. This increase in the signal was expected upon the removal of events which had not experienced the full precession field. The application of the

TABLE 4.2 Polarization analysis for samples with known zero polarization, created by mixing equal numbers of events from positively and negatively polarized samples in both the experimental and Monte Carlo data.

	Experimental	Monte Carlo
$\alpha P_x$	$0.0085 \pm 0.0043$	$0.0006 \pm 0.0058$
$\alpha P_y$	$0.0001 \pm 0.0045$	$0.0067 \pm 0.0060$
$\alpha P_z$	$-0.0049 \pm 0.0054$	$0.0019 \pm 0.0069$
$ \vec{P} $	$0.0101 \pm 0.0048$	$0.0020 \pm 0.0062$

remaining cuts made an additional change in the magnetic moment of less than 0.2 std. dev. Changing the target and collimator positions by  $\pm 2$  mm, the production angle distribution parameter B by  $\pm 5\%$ , and the analyzing magnet field by  $\pm 1\%$  in the Monte Carlo generation changed the measurement of the polarization and the magnet moments by much less than one standard deviation in each case. Stability of the results against cuts was an important test of the purity of the sample and of the effect that the less than perfect acceptance had on the measurements. The measurements in general were not found to be very sensitive to the placement of cuts. Plots of the magnetic moment versus momentum, decay vertex position, and kinematic and geometric  $\chi^2$  are shown in Figures 4.9 and 4.10. The variations in the magnetic moment were largely due to the different event types. The first bin in the vertex plot had no 1y events and showed the lower value associated with the non-1y sample. The first bin in the kinematic  $\chi^2$  plot was dominated by the 1y events, which had a 1-C fit.

The data were also binned and analyzed according to event type. The effects of varying acceptances would be most apparent here, since the definition of event type often defines the geometry of the decay. The magnetic moments for the various track and gamma detection types are plotted in Figure 4.11. The largest difference occurred for the 1 $\gamma$  and 2-detected- $\gamma$ 's samples and was due to the gamma detection differences discussed in Section 4.3.3. The analysis of the Monte Carlo event sample showed the same split in magnetic moment values. The estimated systematic error from these acceptance effects was of the order 1 std. dev.

A last check was made by analyzing the kink subset by two separate methods. Events with a visible kink in the charged track could be fit to the simplified hypothesis  $\Sigma^+ \rightarrow p\pi^0$ , on the track information alone, or could be fit to the global hypothesis  $\Sigma^+ \rightarrow p\pi^0$ ,  $\pi^0 \rightarrow 2\gamma$  with the addition of the gamma information. The polarizations and magnetic moments for the two analysis methods are plotted in Figure 4.12. The difference in the two suggests that the addition of the gamma information changes the result by  $\sim 1$  std. dev., suggesting a possible systematic error of 0.011 on the magnetic moment.

The study of possible backgrounds contamination in Section 3.6 indicated that any contributions from unwanted sources were negligible. The largest systematic effects appear to come from the acceptance sensitivities and the use of the gamma information. A total estimated error of 0.016 was added to the magnetic moment determination to take these effects into account.

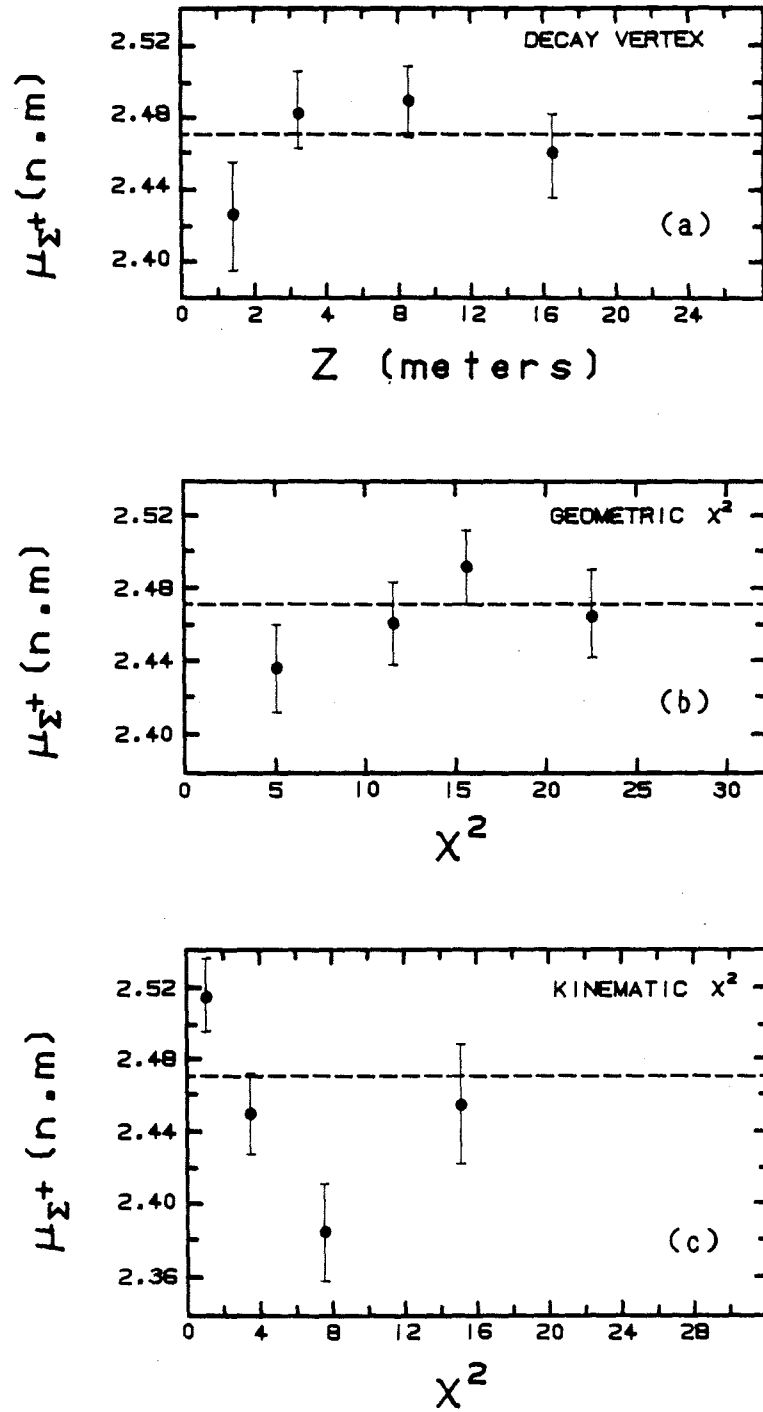


Figure 4.10 The  $\Sigma^+$  magnetic moment plotted against the various cut parameters, (a) the decay vertex, (b) the geometric  $\chi^2$ , and (c) the kinematic  $\chi^2$  for the global fit.

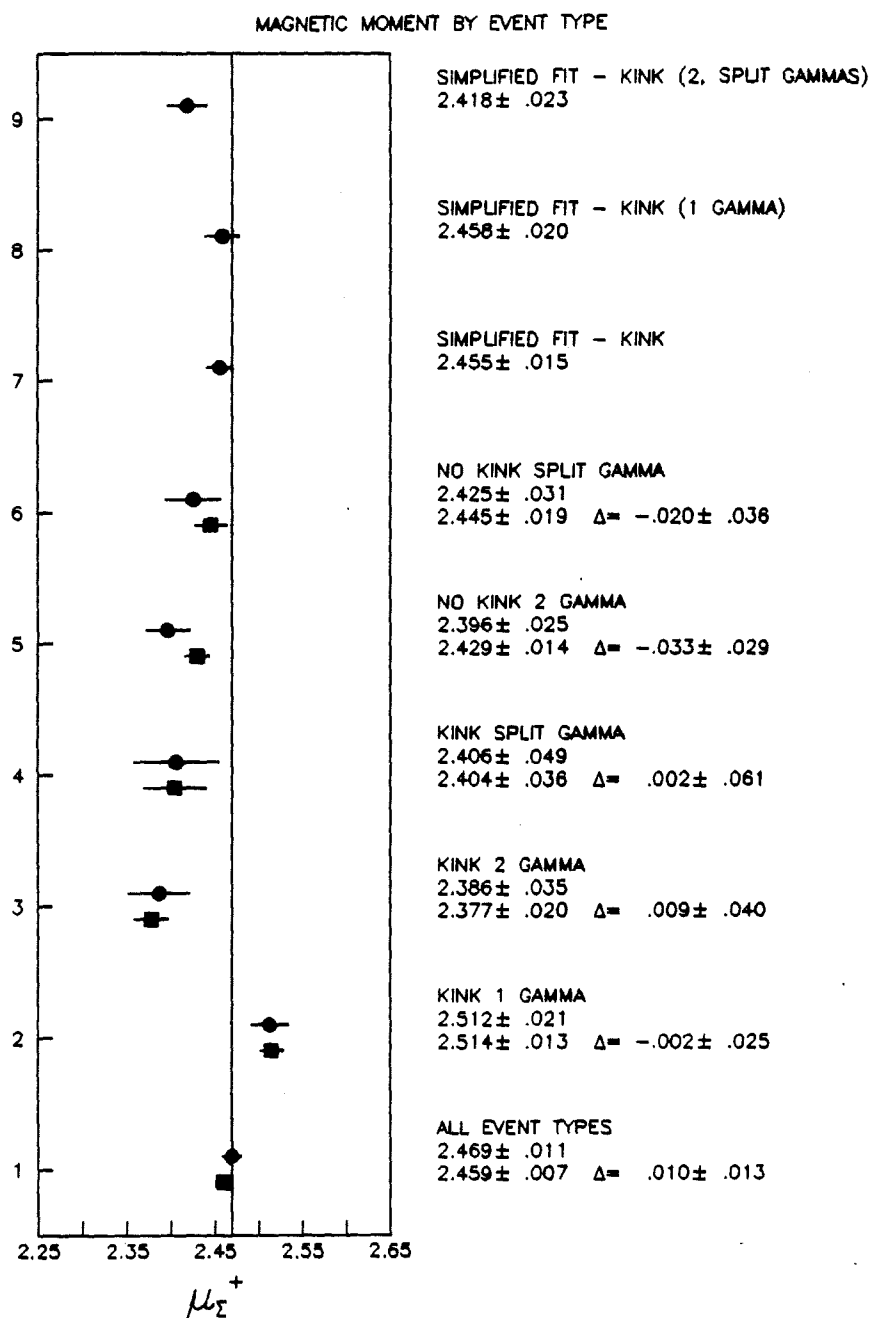


Figure 4.11 The  $\Sigma^+$  magnetic moments for various detection and fit type classifications. The experimental results are represented by the dots and the Monte Carlo results by the squares. The difference between MC and data is also shown.

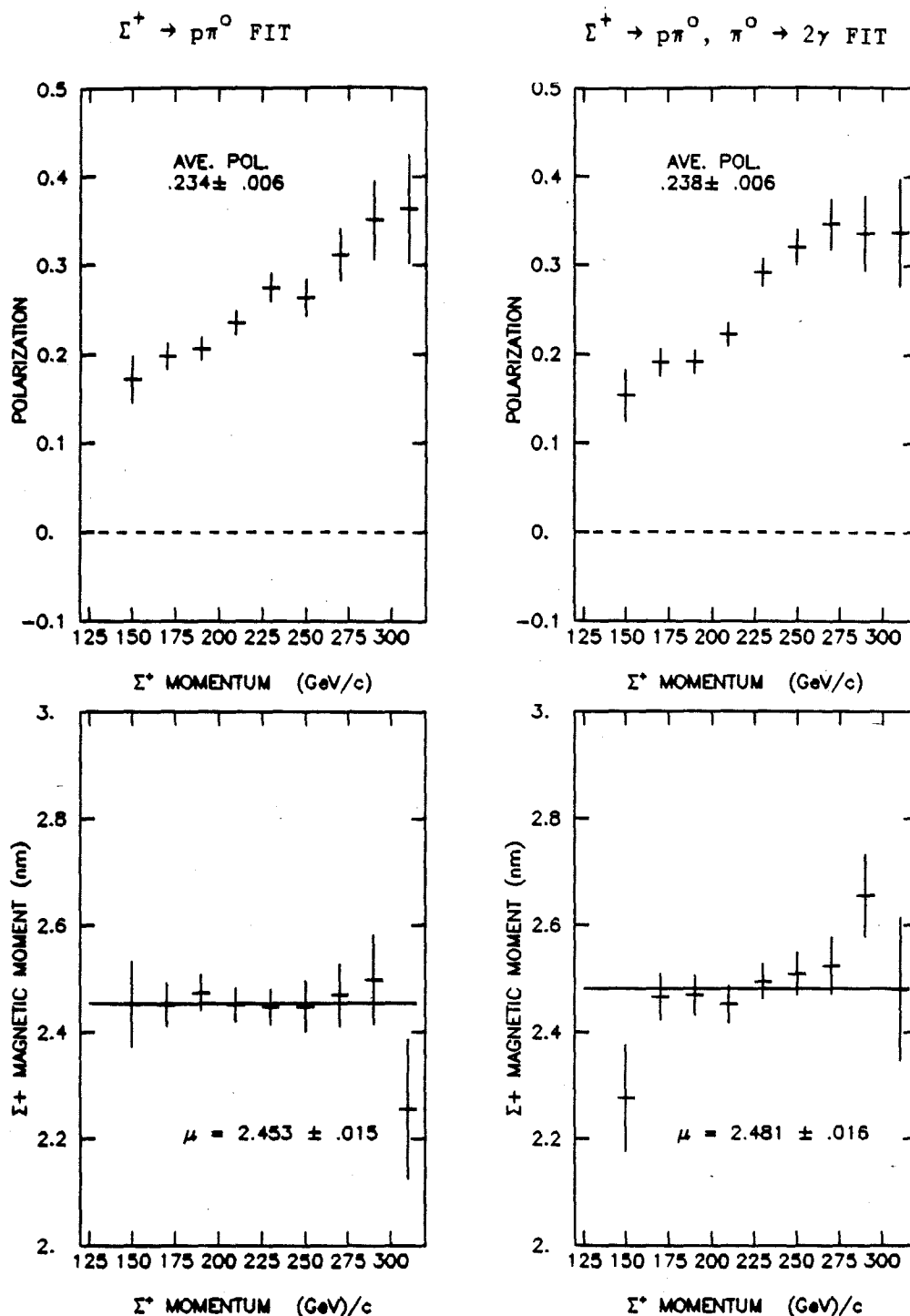


Figure 4.12 The polarization and magnetic moments for the kink track data for two different analysis methods:  $\Sigma^+ \rightarrow p\pi^0$  fit on the basis of the charged track information alone, and  $\Sigma^+ \rightarrow p\pi^0, \pi^0 \rightarrow 2\gamma$  fit with the additional gamma information.

## CHAPTER 5: RESULTS AND IMPLICATIONS

## 5.1 RESULTS SUMMARY

The final results for the polarization of a sample of 137,300  $\Sigma^+$  produced by 400 GeV protons on beryllium was

$$P_{\Sigma}^+ = + (0.234 \pm 0.005) , \quad (5.1)$$

where the range of  $\Sigma^+$  momentum was  $140 \text{ GeV}/c \leq p_{\Sigma} \leq 350 \text{ GeV}/c$ , of transverse momentum was  $0.7 < p_T < 1.75 \text{ GeV}/c$ , and of Feynman  $x$  was  $0.35 < x_F < 0.88$ . The polarization was along the direction  $\hat{k}_{in} \times \hat{k}_{out}$ , which is the same direction as for  $\Sigma^-$  inclusive production<sup>31</sup> but opposite that of  $\Lambda$ ,<sup>32</sup>  $\Xi^0$ ,<sup>33</sup> and  $\Xi^-$ .<sup>26</sup>

The  $\Sigma^+$  magnetic moment determined in this experiment was

$$\mu_{\Sigma^+} = (2.469 \pm 0.011 \pm 0.016) \mu_N , \quad (5.2)$$

where the first uncertainty is statistical and the second is an estimate of the systematic errors. Since the time of data taking for this experiment, another group has also published a  $\Sigma^+$  magnetic measurement,  $\mu_{\Sigma^+} = 2.38 \pm 0.02$ .<sup>34</sup> The values of these two latest experiments have approximately the same precision, but are each  $\sim 3$  std. dev. away from the new world average,  $\mu_{\Sigma^+} = 2.426 \pm 0.044$ .

The sign of the polarization at production was not constrained by this experiment, but was determined by using a previous magnetic moment measurement<sup>18</sup> to estimate the amount the polarization precessed in the magnet M2. The precession angle could also have been determined by



taking data at two or more magnetic field integrals for M2, and fitting a line to the data. Such a procedure would eliminate any ambiguities in the initial polarization direction and the numbers of half revolutions  $n\pi$  in the magnet. Data for this experiment were taken at only one field setting, but, by combining with data from Ref. 34, a plot of precession angle versus magnetic field integral can be made. The two lowest order possibilities for positive or negative initial polarization are plotted in Figure 5.1. A line fit is compatible only with the assumption that the initial polarization is along  $+\hat{x}$ . A plot of the  $\Sigma^+$  magnetic moment measurements to date and the new weighted world average is shown in Figure 5.2.

## 5.2 POLARIZATION THEORIES

Current parton models, in spite of their success in describing many features of particle production, are unable to predict the large polarizations seen in proton induced hyperon production. Figure 5.3 shows a plot of the measured hyperon polarizations, which follow the approximate relationship:

$$P_{\Lambda} = P_{E^0} = P_{E^-} = -P_{\Sigma^+} = -P_{\Sigma^-} . \quad (5.3)$$

Extensive studies of  $\Lambda$  and  $E^0$  production show that the polarization depends on transverse momentum  $p_{\perp}$  and Feynman  $x$ .<sup>32</sup> A function of the form

$$P(x, p_{\perp}) = -(ax + bx^3) [1 - \exp(-\alpha p_{\perp}^2)] \quad (5.4)$$

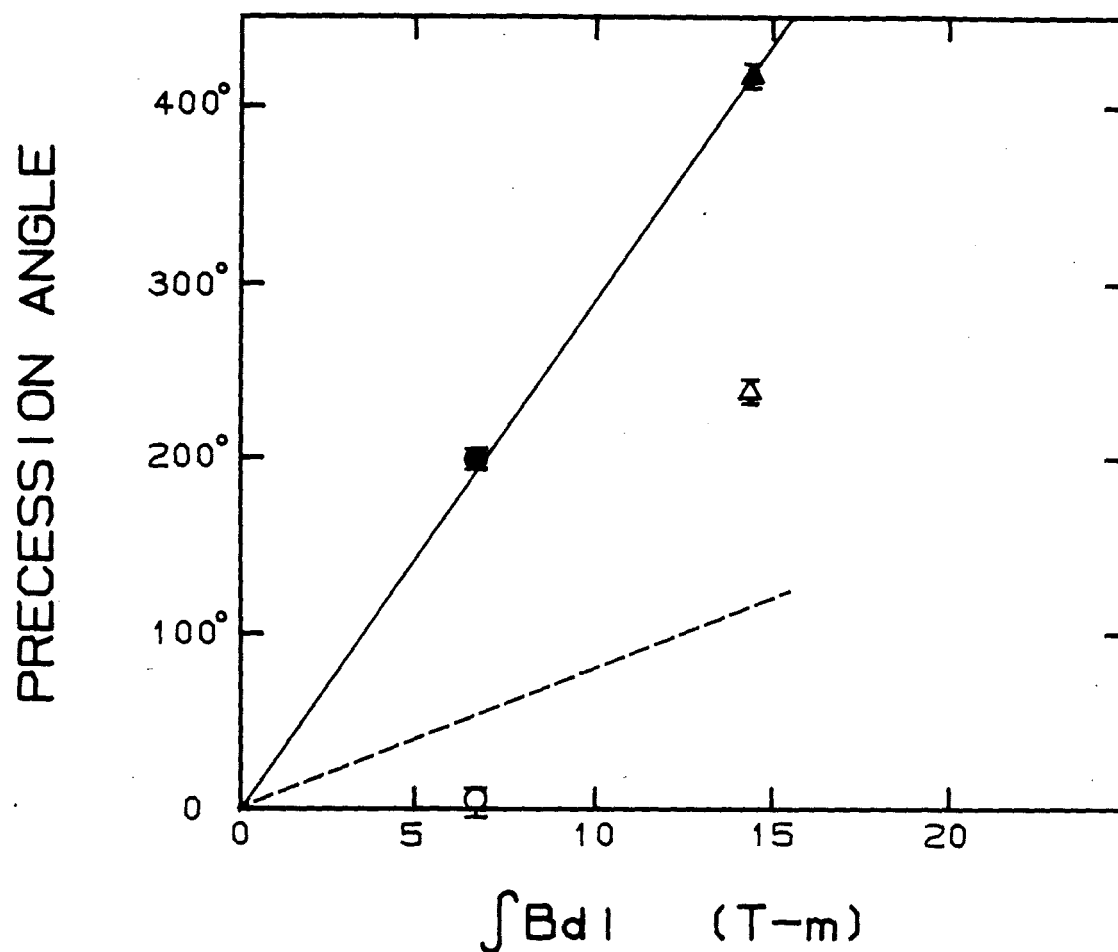


Figure 5.1 Plot of precession angle versus magnetic field integral for this experiment (dots) and for Ref. 34 (triangles). Shaded points represent the lowest order precession angles for positive initial polarization, while open points represent negative initial polarization. A fit with 1-degree of freedom gives a  $\chi^2$  of 3 for the shaded points and a  $\chi^2$  of 590 for the open points, indicating that the initial polarization must be positive.

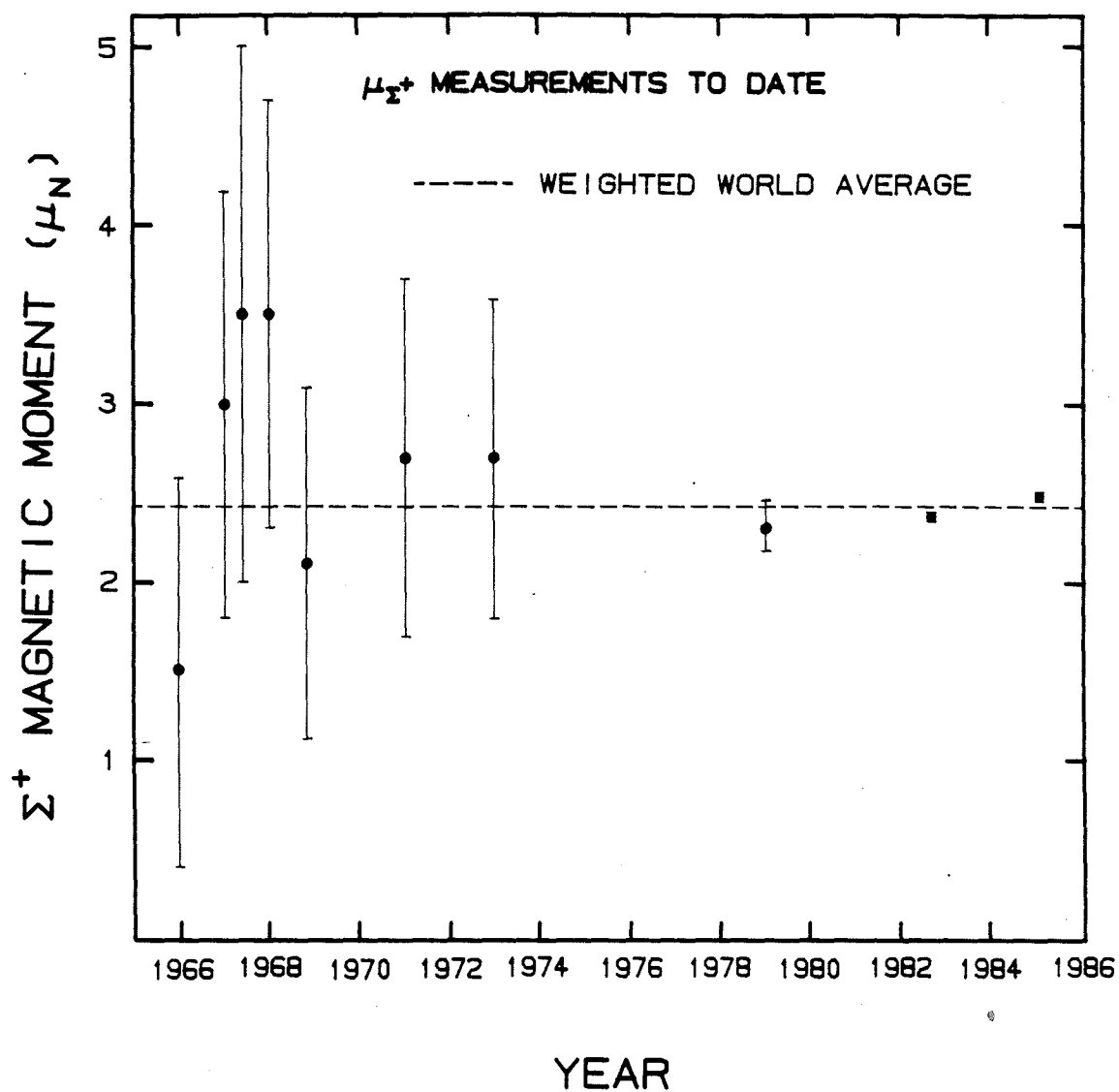


Figure 5.2  $\Sigma^+$  magnetic moment measurements as a function of time. The dotted line indicates the weighted world average, including data from this experiment. References are listed in Table 5.1.

TABLE 5.1 Summary of  $\mu_{\Sigma^+}$  measurements to date. Results are taken from Ref. 53 except where noted.

Reaction	No. of Events	$\mu_{\Sigma^+} (\mu_N)$
$\pi^+ p \rightarrow K^+ \Sigma^+$	235	$1.5 \pm 1.1$
$\gamma p \rightarrow K^0 \Sigma^+$	51	$3.0 \pm 1.2$
$K^- p \rightarrow \pi^- \Sigma^+$	52	$3.5 \pm 1.5$
$\pi^+ p \rightarrow K^+ \Sigma^+$	69	$3.5 \pm 1.2$
$K^- p \rightarrow \pi^- \Sigma^+$	39,000	$2.1 \pm 1.0$
$\pi^+ p \rightarrow K^+ \Sigma^+$	955	$2.7 \pm 1.0$
$K^- p \rightarrow \pi^- \Sigma^+$	2,651	$2.7 \pm 0.9^{(54)}$
$K^- p \rightarrow \pi \Sigma^+$	24,513	$2.30 \pm 0.14^{(18)}$
$pN \rightarrow X + \Sigma^+$	44,457	$2.38 \pm 0.02^{(34)}$
$pN \rightarrow X + \Sigma^+$ (this exp.)	137,500	$2.469 \pm 0.019$
weighted average		$2.426 \pm 0.044$

fits the data reasonably well and exhibits the approximately linear dependence on  $x$  below  $p_{\perp} \approx 0.8$  GeV/c and the saturation above  $p_{\perp} \approx 1.5$  GeV/c. Hyperons produced by proton fragmentation are polarized, but antihyperons and protons are not.<sup>12-14</sup> These data indicate that the polarization is strongly dependent upon the assumed production mechanism.

The production models outlined here are all based on quark recombination theories, in which spectator quarks from the proton are combined with quarks produced in the interaction. Thus, in  $p \rightarrow \Lambda(uds)$ ,

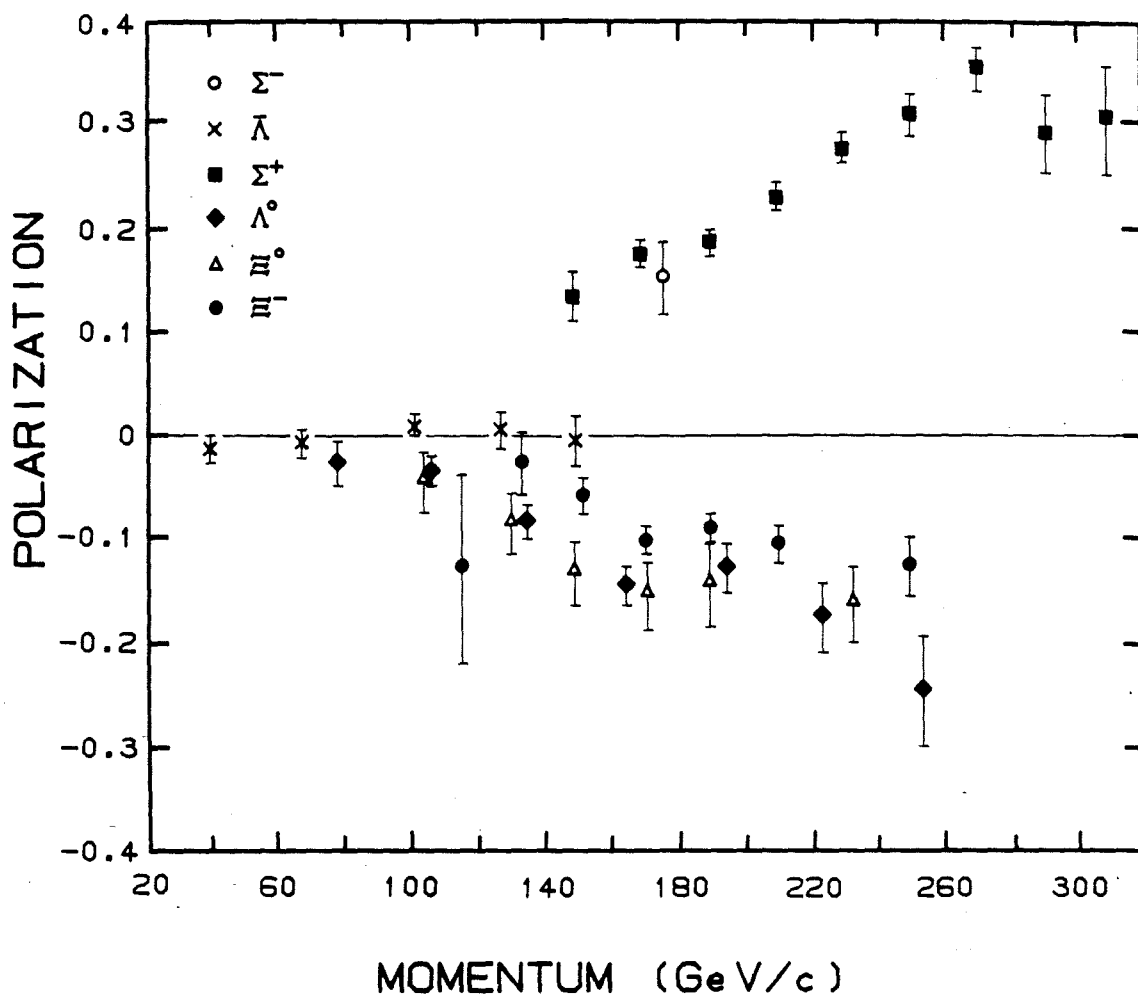


Figure 5.3 Collected inclusive polarization data for hyperons produced by 400 GeV protons incident on a Be target at fixed angle  $\theta_p = 5$  mrad, except for  $\Sigma^-$  and  $\bar{\Lambda}$ , where  $\theta_p = 7.5$  mrad.

$p \rightarrow \Sigma^0(uds)$ , and  $p \rightarrow \Sigma^+(uus)$  production, a collision-produced  $s$  quark is added to the spectator diquark fragment  $ud$  or  $uu$  from the proton ( $uud$ ). Production of  $\Sigma^-(dds)$ ,  $\Xi^-(dss)$ , and  $\Xi^0(uss)$ , on the other hand, combines a spectator  $u$  or  $d$  quark with a produced  $ds$  or  $ss$  diquark. Proton induced  $\bar{\Lambda}(\bar{u}\bar{d}\bar{s})$  has no spectator quarks, and  $p(uud)$  requires no produced quarks.

The simplest explanation of the above notes that polarization occurs only when an  $s$  quark is picked up in the interaction. If the  $s$  quark is assumed to be the carrier, in some unspecified manner, of the polarization, then the simple  $SU(6)$  baryon wavefunctions listed in Table 1.1 can be used to calculate the polarizations. The  $ud$  diquark in the  $\Lambda$  is in a spin 0 state, so the spin and polarization of the  $\Lambda$  is just that of the  $s$ -quark. The polarizations of the  $\Xi^0$  and  $\Xi^-$  must depend on two produced  $s$ -quarks and should be similar to the  $\Lambda$  polarization, as born out by the data. The  $\Sigma^0$  and  $\Sigma^+$ , however, each have a diquark in a spin 1 state which must combine with spin opposite that of the  $s$ -quark in order to produce a spin 1/2 particle. Using the quark wavefunctions for the baryons, this simple picture predicts

$$P_{\Sigma^0} = P_{\Sigma^+} = -\frac{1}{3} P_{\Lambda} . \quad (5.5)$$

The polarization results for this experiment show that the  $\Sigma^+$  polarization is indeed opposite that of the  $\Lambda$  but also the same size. As Szwed<sup>35</sup> and Andersson<sup>16</sup> have pointed out, making direct comparisons of the magnitudes is questionable because the relationships in

Equation (5.3) are calculated for direct production modes only. The measured inclusive  $\Lambda$  polarization may be diluted an unknown amount by daughter  $\Lambda$ 's from  $\Sigma^0$ ,  $\Sigma^*$ , and other decays whose production processes differ from the direct mode. The assumption of the produced s-quark as the carrier breaks down when the  $\bar{\Lambda}$  ( $\bar{u}\bar{d}\bar{s}$ ) is examined. The reaction  $p + N \rightarrow \bar{\Lambda}$ , which has a produced  $\bar{s}$  quark, is unpolarized,<sup>12</sup> but  $K^+ + p \rightarrow \bar{\Lambda}$  has a spectator  $\bar{s}$  quark and is strongly polarized.<sup>36</sup> This polarization must come from the spectator  $\bar{s}$ , since the  $\bar{u}\bar{d}$  diquark has spin 0.

Miettinen and DeGrand,<sup>15,37</sup> therefore, suggest that the polarization is carried by both the quark and diquark. If the asymmetry is parameterized by  $\epsilon$  for the lone quark and by  $\delta$  for the diquarks, the wavefunctions give

$$P_{\Lambda} = -\epsilon \quad (5.6)$$

$$P_{\Sigma^+} = \frac{1}{3} \epsilon + \frac{2}{3} \delta ,$$

which match the measured  $\Sigma^+$  result if  $\epsilon = \delta$ . Miettinen and DeGrand have also calculated the polarizations for a large number of beams and final state particles, which compare favorably with known results.

Proposed dynamical models of polarization depend upon which carriers of the polarization have been assumed by the authors. Szwed<sup>35</sup> suggests that the slow sea s-quark is polarized as it scatters off quark-gluonic fields before recombination. Examining polarization at a certain value of  $P_T$  biases the selection of s-quark states with large

transverse momentum  $k_T$  in the direction of  $P_T$ . The scattering process correlates  $k_T$  with the spin alignment. Andersson and his collaborators attribute the polarization to a similar biasing effect but assume that the spin correlation occurs when  $s\bar{s}$  pairs are created along a color field string stretched between the collision center and the separating valence quarks.<sup>16,38</sup> The quark-antiquark pair is produced with equal and opposite momenta transverse to the string, as shown in Figure 5.4. The spins must also be opposite to conserve angular momentum. Both these models assume, therefore, that the polarization is a sort of selection bias effect, where specifying  $P_T$  automatically enhances the selection of certain  $k_T$ -spin states.

Miettinen and DeGrand's model<sup>15,37</sup> assumes that the polarization is a kinematic effect caused by the torques on  $k_T$  experienced by fast valence quarks as they slow down and by slow sea quarks as they speed

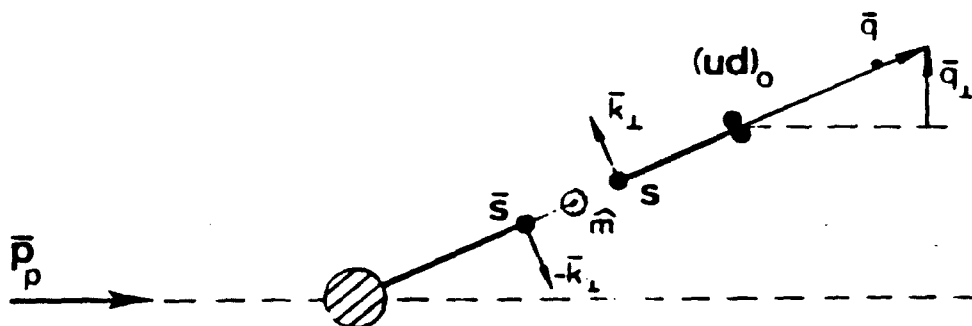


Figure 5.4 An  $s\bar{s}$  pair is created along a color force field string stretched between the collision center and separating valence quarks  $ud$ . The  $s\bar{s}$  transverse momenta give rise to an orbital angular momentum in the direction  $\hat{m} = (\mathbf{q} \times \mathbf{k}_\perp) / |\mathbf{q} \times \mathbf{k}_\perp|$ , which leads to polarized  $s\bar{s}$  quarks. Taken from Reference 16.



up in the recombination process. The known polarizations fit the hypothesis that slow quarks combine spin down and fast quarks combine spin up with respect to the production plane. Unfortunately the authors have not yet been able to validate the existence of such a spin state preference.

All the dynamical models suffer from the difficulties of making calculations in the low  $P_T$  regions where QCD and perturbation methods fail. Fortunately, the proposed models make many predictions which can be tested in inclusive and exclusive production. Further experimental results should help identify which particles carry the polarizations and which dynamical models are the most profitable to pursue.

### 5.3 MAGNETIC MOMENT MODELS

The earliest calculations of the baryon magnetic moments were based on SU(3) and ignored the mass splittings which broke the unitary symmetry. Various relationships between the baryon magnetic moments were predicted by this two parameter model, in particular,  $\mu_{\Sigma^+} = \mu_p$  and  $\mu_{\Lambda} = \mu_n/2$ .<sup>39</sup> The additional relationship  $\mu_p/\mu_n = -3/2$  was predicted<sup>1</sup> by using SU(6) and is indeed the observed ratio. When the measured value<sup>4</sup> of  $\mu_{\Lambda}$  was found to be incompatible with these predictions, the mass splittings could no longer be ignored. Using the color SU(6) wave functions first proposed by O. W. Greenberg,<sup>40</sup> the current set of simple SU(6) magnetic moment predictions were obtained.<sup>41</sup> This three parameter model successfully predicted  $\mu_{\Lambda}$ , but the next precision magnetic moment measurement, that of the  $\Xi^0$ ,<sup>42</sup> was 13 std. dev. away

from the predicted value of  $\mu_{\Sigma^0} = -1.44 \mu_n$ . As more measurements were made, including the results for the charged hyperons from this experiment, other large deviations became apparent. The measured  $\Sigma^+$  moment is approximately 10 std. dev. from the predicted value. Obviously something is missing from the model.

The simple models relied on the static properties of quarks and ignored any suspected dynamics or interactions between them. The ground state wave functions, for example, assumed no configuration mixing with other orbital or spin angular momentum states. The definition of quark mass is in itself a problem. Depending upon the model and the particle properties under study, quarks have been assigned masses from zero to infinity, as pointed out by Lipkin.<sup>43</sup> Although constituent quark masses seem appropriate for studies involving hadron mass splittings and moments, the effective masses and moments may vary from hadron to hadron, showing a dependence upon environment. Given the serious nature of some of these effects, one wonders why the simple quark model works as well as it does. Cohen and Lipkin<sup>44</sup> suggest that the good agreement is due to the absorption of many of these effects into the effective quark masses or moments, which are in reality just free parameters fit to the data.

Several authors have attempted to refine the naive model by calculating these previously ignored effects directly, but the results are highly dependent upon the model and the assumptions used. As Lichtenberg<sup>45</sup> points out, not only is it difficult to isolate the individual effects, but it is sometimes impossible to know which

effects to include. In certain cases, configuration mixing and SU(3) symmetry breaking effects can simulate environmental effects. There appear to be too many unknowns and no definitive model. The results of a representative number of these calculations are given in Table 5.2. None are able to predict consistently the measured values, most of which are known to within 1%. In general, the success of the predictions appears to scale with the number of parameters in the

TABLE 5.2 Theoretical predictions for the hyperon magnetic moments in nuclear magnetons, based on refinements of the naive quark model.

	Experiment <sup>a</sup>	b	c	d	e	f
p	2.793	2.64	input	input	2.85	input
n	-1.913	-1.76	input	input	-1.85	input
$\Lambda$	$-0.613 \pm 0.004$	-0.62	input	-0.61	-0.61	input
$\Sigma^+$	$2.469 \pm 0.019$	2.53	2.14	2.39	2.54	2.40
$\Sigma^0 \rightarrow \Lambda$	$-1.61 \pm 0.07$		0.65	1.45	-1.51	1.52
$\Sigma^-$	$-1.10 \pm 0.05$	-0.96	-0.83	-0.95	-1.00	-0.82
$\Xi^0$	$-1.253 \pm 0.014$	-1.36	-1.13	-1.27	-1.20	-1.25
$\Xi^-$	$-0.69 \pm 0.04$	-0.53	-0.46	-0.48	-0.43	-0.68

a) See Table 1.3.

b) Reference 46

c) Reference 47

d) Reference 48

e) Reference 49

f) Reference 50

model, a relationship which undermines one's belief in the validity of the calculations.

In view of the great difficulty in determining and calculating these effects, some authors<sup>42,51,52</sup> have proposed using sum rules rather than the absolute magnetic moments. Appropriate relationships between the baryon magnetic moments or masses can be used to isolate the individual quark contributions. It is argued that the dynamical terms will cancel out in differences and ratios. Linear sums within multiplets can also be formed and tested against the data for symmetry breaking effects. The purpose of the sum rule approach is to indicate which effects are the most significant. The results from these manipulations, however, are not entirely unambiguous, as Franklin's calculation of the strange quark moment demonstrates.<sup>52</sup> He obtains three values for  $\mu_s$ :  $\mu_s$  (in  $\Lambda$ ) =  $-0.61 \mu_n$ ,  $\mu_s$  (in  $\Xi^0$ ) =  $-0.68 \mu_n$ , and  $\mu_s$  (in  $\Sigma^+$ ) =  $+0.49 \mu_n$ , a result difficult to interpret!

Although there now exist eight data points for the hyperon magnetic moments with which to test the theories, the picture of the underlying physics of hadrons is still highly confused. The physics is apparently far too complex for a description of the hyperon magnetic moments alone to yield the correct picture. The physics community may have to adopt the attitude of Isgur and Karl,<sup>49</sup> who encountered a similar situation when they attempted to add refinements to the naive calculations of the magnetic moments of tritium and  $^3\text{He}$ . Calculations based on the simple additive approach using known nuclear magnetic moments had predicted the measured values only to within  $0.2 \mu_n$ , the

same accuracy as for the naive quark model predictions of the hyperon magnetic moments. Isgur and Karl state that "the accuracy of naive calculations may be as good as one can realistically expect."

*The wizard opened one of the cabinets and produced a large roll of parchment, which he handed to the scarecrow. "Here," he continued, "is yours." ...*

*The scarecrow stared at the parchment for a few seconds and then suddenly said, "The theory of relativity, as proposed by Professor Albert Einstein, teaches us that infinite space is not infinite at all. It merely curves back upon itself and--"*

The Wizard of Oz,  
adapted by Horace J. Elias  
from the original story by  
L. Frank Baum

## REFERENCES

1. M.A.B. Beg, B.W. Lee, and A. Pais, Phys. Rev. Lett. 13, 514 (1964); or G. Morpurgo, Physics 2, 95 (1965).
2. A. DeRujula, Howard Georgi, and S.L. Glashow, Phys. Rev. D12, 147 (1975).
3. G. Bunce, et al., Phys. Rev. Lett. 36, 1113 (1976):
4. L. Schachinger, et al., Phys. Rev. Lett. 41, 1348 (1978).
5. For a review, see C. Bourrely, E. Leader, and J. Soffer, Phys. Rep. 59, 95 (1980).
6. P. Skubic, et al., Phys. Rev. D18, 3115 (1978).
7. R. Grobel, Ph.D. Thesis, University of Wisconsin (1980) (unpublished).
8. K. Heller, et al., Phys. Lett. B68, 480 (1977).
9. B. Lundberg, Ph.D. Thesis, University of Wisconsin (1983) (unpublished).
10. K. Raychaudhuri, et al., Phys. Lett. B90, 319 (1980); Erratum: Phys. Lett. B93, 525 (1980).
11. R. Handler, et al., Phys. Rev. D25, 639 (1982); K. Heller, et al., Phys. Rev. 51, 2025 (1983).
12. K. Heller, et al., Phys. Rev. Lett. 41, 607 (1978); Erratum: Phys. Rev. Lett. 45, 1043 (1980).
13. R.O. Polvado, et al., Phys. Rev. Lett. 42, 1325 (1979).
14. P. Yamin, et al., Phys. Rev. D23, 31 (1981).
15. T.A. DeGrand and H.I. Miettinen, Phys. Rev. D24, 2419 (1981). This paper contains an error in the sign of  $P_{\Sigma^-}$ , which was corrected by T.A. DeGrand in private communication.
16. B. Andersson, et al., Phys. Lett. B85, 417 (1979).
17. For a review of hyperon experiments and theories, see L.G. Pondrom, Phys. Rep. 122, Nos. 2 and 3 (1985).
18. R. Settles, et al., Phys. Rev. D20, 2154 (1979).

19. See, for example, R. Hagedorn, "Relativistic Kinematics," pp. 124-126, W.A. Benjamin, Inc. (1963).
20. See, for example, R.D. Sard, "Relativistic Mechanics," pp. 281-298, W.A. Benjamin, Inc. (1970); or J.D. Jackson, "Classical Electrodynamics," pp. 541-546, 2nd edition, John Wiley and Sons, Inc. (1975).
21. L.H. Thomas, Phil. Mag. 3, 1 (1927).
22. V. Bargmann, L. Michel, and V.L. Telegdi, Phys. Rev. Lett. 2, 435 (1959); see also reference 19, pp. 126-137.
23. W. Thirring, Acta Phys. Aust., Supple. II, 205 (1965); and J.J.J. Kokkedee, "The Quark Model," pp. 23-26, W.A. Benjamin, Inc. (1969).
24. Particle Data Group, Phys. Lett. B111, (1982).
25. P. Petersen, Ph.D. Thesis, Rutgers University (1985) (unpublished).
26. R. Rameika, Ph.D. Thesis, Rutgers University (1981) (unpublished); Phys. Rev. Lett. 52, 581 (1984).
27. L. Schachinger, Ph.D. Thesis, Rutgers University (1978) (unpublished).
28. P. Martin, Ph.D. Thesis, University of Wisconsin (1978), (unpublished); P. Skubic, Ph.D. Thesis, University of Michigan (1977) (unpublished).
29. R. Thun, et al., Nuc. Inst. Meth. 138, 437 (1976).
30. C. Wilkinson, et al., Phys. Rev. Lett. 46, 805 (1981).
31. L. Deck, et al., Phys. Rev. D28, 1 (1983).
32. B. Lundberg, et al., "High Energy Spin Physics-1982", Brookhaven National Laboratory, AIP Conference Proceedings 95, p. 83, edited by G. Bunce (1983); B. Lundberg, Ph.D. Thesis, University of Wisconsin (1984) (unpublished).
33. K. Heller, et al., Phys. Rev. Lett. 51, 2025 (1983).
34. C. Ankenbrandt, et al., Phys. Rev. Lett. 51, 863 (1983).
35. J. Szwed, Phys. Lett. B105, 403 (1981).



36. I.V. Ajinenko, et al., Phys. Lett. B121, 183 (1983).
37. T.A. DeGrand, et al., Phys. Rev. D32, 2445 (1985).
38. G. Gustafson, "High Energy Spin Physics-1982", Brookhaven National Laboratory, AIP Conference Proceedings 95, p. 355, edited by G. Bunce (1983).
39. S. Coleman and S.L. Glashow, Phys. Rev. Lett. 8, 423 (1961).
40. O.W. Greenberg, Phys. Rev. Lett. 13, 598 (1964).
41. S.B. Gerasimov, Zh. Eksp. Teor. Fiz. 50, 1559 (1966).
42. P.T. Cox, et al., Phys. Rev. Lett. 46, 877 (1981).
43. H. Lipkin, Phys. Rev. Lett. 41, 1629 (1978).
44. I. Cohen and H. Lipkin, Phys. Lett. B93, 57 (1980).
45. D.B. Lichtenberg, Zeit. fur Phys. C7, 143 (1981).
46. T. Barnes, Nuc. Phys. B96, 353 (1975).
47. Y. Tomozawa, Phys. Rev. D19, (1979).
48. R.B. Teese and R. Settles, Phys. Lett. B87, 111 (1979).
49. N. Isgur and G. Karl, Phys. Rev. D21, 3175 (1980).
50. R.B. Teese, Phys. Rev. D24, 1413 (1981).
51. H. Lipkin, Phys. Lett. B89, 358 (1980).
52. J. Franklin, Phys. Rev. Lett. 45, 1607 (1980).
53. P.W. Alley, et al., Phys. Rev. D3, 75 (1971).
54. M. Saha, et al., Phys. Rev. D7, 3295 (1973).

